MINISTÉRIO DA CIÊNCIA, TECNOLOGIA E INOVAÇÕES
INSTITUTO NACIONAL DE PESQUISAS ESPACIAIS

sid.inpe.br/mtc-m12e/2025/04.07.19.12-TDI

DETERMINATION OF THE HUBBLE CONSTANT FROM MULTI-MESSENGER ASTRONOMY INVOLVING GRAVITATIONAL WAVES

Mayara Hilgert Pacheco

Master's Dissertation of the Graduate Course in Astrophysics, guided by Drs. Odylio Denys de Aguiar, and Josiel Mendonça Soares de Souza, approved in March 31, 2025.

URL of the original document:
<http://urlib.net/8JMKD2USNRW34T/4D9P9J2>

INPE
São José dos Campos
2025

PUBLISHED BY:

Instituto Nacional de Pesquisas Espaciais - INPE
Coordenação de Ensino, Pesquisa e Extensão (COEPE)
Divisão de Biblioteca (DIBIB)
CEP 12.227-010
São José dos Campos - SP - Brasil
Tel.:(012) 3208-6923/7348
E-mail: pubtc@inpe.br

MINISTÉRIO DA CIÊNCIA, TECNOLOGIA E INOVAÇÕES
INSTITUTO NACIONAL DE PESQUISAS ESPACIAIS

sid.inpe.br/mtc-m12e/2025/04.07.19.12-TDI

DETERMINATION OF THE HUBBLE CONSTANT FROM MULTI-MESSENGER ASTRONOMY INVOLVING GRAVITATIONAL WAVES

Mayara Hilgert Pacheco

Master's Dissertation of the Graduate Course in Astrophysics, guided by Drs. Odylio Denys de Aguiar, and Josiel Mendonça Soares de Souza, approved in March 31, 2025.

URL of the original document:
<http://urlib.net/8JMKD2USNRW34T/4D9P9J2>

INPE
São José dos Campos
2025

Cataloging in Publication Data

Pacheco, Mayara Hilgert.

P115d Determination of the hubble constant from multi-messenger astronomy involving gravitational waves / Mayara Hilgert Pacheco. – São José dos Campos : INPE, 2025.

xviii + 103 p. ; (sid.inpe.br/mtc-m12e/2025/04.07.19.12-TDI)

Dissertation (Master in Astrophysics) – Instituto Nacional de Pesquisas Espaciais, São José dos Campos, 2025.

Guiding : Drs. Odylio Denys de Aguiar, and Josiel Mendonça Soares de Souza.

1. Standard sirens. 2. Hubble tension. 3. Gravitational waves. 4. Cosmology. 5. Multi-messenger astrophysics. I.Title.

CDU 52:551.511.31

MINISTÉRIO DA CIÊNCIA, TECNOLOGIA E INOVAÇÃO

INSTITUTO NACIONAL DE PESQUISAS ESPACIAIS

Serviço de Pós-Graduação - SEPGR

Aluno(a): Mayara Hilgert Pacheco

Título: "Determination of the Hubble Constant from Multi-messenger Astronomy Involving Gravitational Waves."

Aprovado(a) pela Banca Examinadora em cumprimento ao requisito exigido para obtenção do Título Mestre (a) em Astrofísica.

(assinado eletronicamente)
Dr. José Carlos Neves de Araújo - Presidente - Membro Interno (DIAST/INPE & PGAST/INPE)
(**X**) Aprovado ( ) Reprovado

(assinado eletronicamente)
Dr. Carlos Alexandre Wuensche de Souza - Membro Interno (DIAST/INPE & PGAST/INPE)
(**X**) Aprovado ( ) Reprovado

(assinado eletronicamente)
Dr. Odylio Denys de Aguiar - Orientador - Membro Interno (DIAST/INPE & PGAST/INPE)
(**X**) Aprovado ( ) Reprovado

(assinado eletronicamente)
Dr. Josiel Mendonça Soares de Souza - Orientador - Membro Externo (UFRJ)
(**X**) Aprovado ( ) Reprovado

(assinado eletronicamente)
Dr. Riccardo Sturani - Membro Externo (UNESP - IFT)
(**X**) Aprovado ( ) Reprovado

Este trabalho foi aprovado por:

( ) maioria simples
(**X**) unanimidade

São José dos Campos, 31 de março de 2025

Documento assinado eletronicamente por **Riccardo Sturani (E)**, **Usuário Externo**, em 03/04/2025, às 11:04 (horário oficial de Brasília), com fundamento no § 3º do art. 4º do Decreto nº 10.543, de 13 de novembro de 2020.

Documento assinado eletronicamente por **Carlos Alexandre Wuensche de Souza**, **Pesquisador**, em 03/04/2025, às 12:07 (horário oficial de Brasília), com fundamento no § 3º do art. 4º do Decreto nº 10.543, de 13 de novembro de 2020.

Documento assinado eletronicamente por **José Carlos Neves de Araújo**, **Pesquisador**, em 03/04/2025, às 15:07 (horário oficial de Brasília), com fundamento no § 3º do art. 4º do Decreto nº 10.543, de 13 de novembro de 2020.

Documento assinado eletronicamente por **Josiel Mendonça Soares de Souza**, **Usuário Externo**, em 04/04/2025, às 12:19 (horário oficial de Brasília), com fundamento no § 3º do art. 4º do Decreto nº 10.543, de 13 de novembro de 2020.

Documento assinado eletronicamente por **Odylio Denys de Aguiar**, **Pesquisador**, em 04/04/2025, às 21:44 (horário oficial de Brasília), com fundamento no § 3º do art. 4º do Decreto nº 10.543, de 13 de novembro de 2020.

A autenticidade deste documento pode ser conferida no site https://sei.mcti.gov.br/verifica.html, informando o código verificador **12715402** e o código CRC **D6B7B6AA**.

Referência: Processo nº 01340.002242/2025-14 SEI nº 12715402

A meus pais ***Jaqueline*** *e* ***Valdeci****.*

ACKNOWLEDGEMENTS

Palavras são insuficientes para expressar minha profunda gratidão aos meus orientadores, Odylio e Josiel, por terem aceitado me guiar nessa jornada e por o terem feito com tanta paciência, dedicação e leveza. Inúmeras vezes, mesmo sem perceber, vocês me acalmaram, ajudaram a compreender que os obstáculos são inerentes à vida acadêmica e que, quando as coisas não saem como planejado, não é o fim do mundo. Sinto-me verdadeiramente privilegiada por tê-los tido como mentores e por todo o apoio que me deram ao longo desse caminho.

Agradeço também a todos os professores da divisão que, direta ou indiretamente, contribuíram para o meu crescimento intelectual e pessoal. Cada aula, conversa e orientação foi fundamental para a construção do conhecimento que hoje carrego comigo. Agradeço a o Instituto Nacional de Pesquisas Espaciais e a CNPq, sem os quais essa pesquisa e meus estudos não seriam possiveis.

Meu agradecimento estende-se aos amigos que fiz durante essa trajetória, em especial ao Djalma, Luan, Verônica e Jonas. Vocês foram pilares essenciais nesse processo! Foram vocês que ouviram minhas reclamações, presenciaram meus momentos de desespero e crises de ansiedade, mas também foram vocês que sempre me encorajaram, dizendo que tudo daria certo. Acompanharam-me nos momentos de descontração, fizeram-me rir e, acima de tudo, lembraram-me que a vida presta.

Não poderia deixar de expressar minha gratidão aos meus pais, que desde a infância me incentivaram a estudar e sempre apoiaram meus sonhos e escolhas, mesmo quando divergiam das expectativas que poderiam ter. Seu apoio incondicional foi a base que me permitiu chegar até aqui.

Por fim, dedico este trabalho a todos que acreditaram em mim, mesmo nos momentos em que eu mesma duvidei de minhas capacidades. Vocês foram fundamentais para que este momento se tornasse realidade, e sou eternamente grata por cada palavra de incentivo, cada gesto de apoio e por acreditarem em mim quando eu mais precisei.

ABSTRACT

In 1916, Albert Einstein postulated the existence of gravitational waves (GW) as a natural outcome of his Theory of General Relativity. These waves were predicted to be transverse distortions of space-time that travel at the speed of light. A century later, in 2015, the Advanced Laser Interferometer Gravitational-wave Observatory (LIGO) confirmed the existence of gravitational waves during its first run (O1). This groundbreaking discovery revolutionized astronomy by facilitating multi-messenger observations. On the other hand, Alexandre Friedmann and Georges Lemaître independently proposed the theoretical foundations for cosmic expansion. Edwin Hubble later quantified the rate of cosmic expansion through his namesake law, which relates recession velocity to distance. The Hubble constant (H_0) is a critical cosmology parameter representing the cosmic expansion rate. Its precise value has been the subject of extensive study, with various measurements yielding conflicting results. This discrepancy, known as the Hubble Tension, poses a significant challenge in cosmology. To address this issue, scientists are exploring the use of gravitational waves as "standard sirens" (in analogy to "standard candles" in electromagnetic astrophysics). Gravitational wave analysis offers a direct way to estimate cosmological distances, without relying on traditional distance indicators. With the advancements in ground-based interferometers like LIGO, Virgo, and KAGRA and future projects like the Einstein Telescope (ET) and Cosmic Explorer (CE), the standard siren technique hold promise for resolving the Hubble Tension. This dissertation delves into the standard siren technique, employing GWDALI software to estimate gravitational wave parameters from compact object mergers. We also investigate the strength of next-generation detectors on constraining cosmological parameters via $D_L - z$ relationships of 'bright' standard sirens. For this task, we explore the efficiency and efficacy of DALI methods in approximating cosmological posteriors.

Keywords: Standard Sirens. Hubble Tension. Gravitational Waves. Cosmology. Multi-Messenger Astrophysics.

DETERMINAÇÃO DA CONSTANTE DE HUBBLE ATRAVÉS DE ASTROFÍSICA MULTI-MENSAGEIRA UTILIZANDO ONDAS GRAVITACIONAIS

RESUMO

Em 1916, Albert Einstein previu a existência de ondas gravitacionais como uma consequência natural de sua Teoria da Relatividade Geral. Essas ondas foram descritas como distorções transversais do espaço-tempo que se propagam à velocidade da luz. Um século depois, em 2015, a existência das ondas gravitacionais foi confirmada pela colaboração do Advanced Laser Interferometer Gravitational-Wave Observatory (Advanced LIGO), durante sua primeira campanha de observações (O1). Essa descoberta revolucionou a astronomia ao inaugurar a era da astronomia multimensageira com ondas gravitacionais.

Na década seguinte a formulação da RG, a descoberta da expansão do universo foi realizada de forma independente por Alexander Friedmann e Georges Lemaître. Posteriormente, Edwin Hubble quantificou essa expansão por meio da formulação de sua lei, que relaciona a velocidade de recessão das galáxias com sua distância. A constante de Hubble (H_0) é um dos parâmetros fundamentais da cosmologia, representando a taxa de expansão do universo. No entanto, sua determinação tem sido alvo de extensos estudos, cujas medições independentes apresentam resultados discrepantes. Essa divergência, conhecida como Tensão de Hubble, constitui um dos principais desafios atuais da cosmologia observacional.

Diante desse cenário, uma abordagem promissora envolve o uso de ondas gravitacionais como "sirenes padrão", em analogia às "velas padrão"da astrofísica eletromagnética. A análise de sinais de ondas gravitacionais permite estimar diretamente distâncias luminosas, sem recorrer aos tradicionais indicadores de distância. Com os avanços dos interferômetros terrestres, como LIGO, Virgo e KAGRA, e com os projetos futuros do Einstein Telescope (ET) e do Cosmic Explorer (CE), a técnica das sirenes padrão se mostra promissora para contribuir na resolução da Tensão de Hubble.

Esta dissertação investiga em profundidade a técnica das sirenes padrão, utilizando o software GWDALI para estimar parâmetros associados a fontes de ondas gravitacionais. Também é avaliado o potencial dos detectores de próxima geração na imposição de restrições sobre parâmetros cosmológicos, por meio da relação D_L–z obtida com sirenes padrão. Para essa finalidade, são exploradas a eficiência e a precisão dos métodos DALI na aproximação de distribuições posteriores cosmológicas.

Palavras-chave: Sirenes Padrão. Tensão de Hubble. Ondas Gravitacionais. Cosmologia. Astrofísica Multi-Mensageira.

LIST OF FIGURES

Page

LIST OF TABLES

Page

CONTENTS

1 INTRODUCTION

In the year 1916, Albert Einstein, after formulating the final set of field equations of the Theory of General Relativity, postulated the existence of gravitational waves (GW). He observed that the weak field equations, when linearized, give rise to wave solutions, which manifested as transverse waves of spatial deformation propagating at the speed of light, known as gravitational waves (MAGGIORE, 2008). This prediction was confirmed a century later, on September 14, 2015. During the first run (O1) of Advanced Laser Interferometer Gravitational-wave Observatories (LIGO), located in Livingston, Louisiana and Hanford, Washington, USA, a signal was detected, which upon analysis, was identified as the outcome of the collision of two black holes in a binary system, having masses of 29 and $36M_{\odot}$ (ABBOTT et al., 2016).

As of now, the LIGO collaboration has identified more than 90 confirmed gravitational-wave detections up until the end of the third observing run (O3) in 2020. Since the O4 analysis, which began in May 2023, is still ongoing, a few dozen significant candidate events have been detected by the LIGO detectors, though this number is subject to change as the analysis progresses. These candidates are currently under analysis, and some are expected to be confirmed as gravitational-wave detections. By the end of the O4 run in October 2025, the total number of detections is expected to exceed 100.

Among these detections, one of the most notable was made by three interferometers - two LIGO along with a Michelson detector located outside of Pisa, Italy, the Virgo. This signal, known as GW170817 and identified on August 17, 2017, marked the first signal ever detected from the merging of two neutron stars. Emitting both gravitational and electromagnetic waves, in the form of a short gamma-ray burst (GRB170817A), x-rays, ultraviolet, visible light, infrared, and radio, originated from a distance of 40 megaparsecs (Mpc) (ABBOTT et al., 2017b; ABBOTT et al., 2017d). Figure 1.1 depicts the signals detected from this event. The location of the gravitational wave source derived by LIGO-Virgo was in line with the GRB, resulting in the identification of a transient source called AT2017gfo (ABBOTT et al., 2017b; STRATTA; PANNARALE, 2022), befitting with a kilonova. The coalescence signals were detected in an wide eletromagnetic window by several observatories, marking the beginning of a new era in multi-messenger astronomy.

When the General Relativity (GR) theory was published, astronomers thought the universe was static (RYDEN, 2003). In fact, Einstein even modified his equations

to align with this belief. However, Alexandre Friedmann's articles in 1922 and 1924 proposed dynamic, expanding solutions to Einstein's equations, while George Lemaître made an independent discovery in 1927 that challenged this static universe paradigm. It was not until 1929 that Edwin Hubble used astronomical observations and Cepheids Variables as distance markers to establish a direct linear relationship between recession velocity and galaxy distance, known as Hubble-Lemaître's Law ($v_r = H_0 d$), confirming the universe's expansion and measuring it through H_0, the Hubble constant. This discovery led to the search for the universe's primordial origin, a singular moment in which space and time emerged simultaneously.

In modern Cosmology, besides expressing the universe's expansion rate, the square of H_0 relates the total energy density of the universe to its geometry, as well as making it possible to calculate the age of the universe, the size of the observable universe, and its radius of curvature, for that H_0 is one of the most important parameters in Cosmology. Due to the relevance of the H_0 numerous methods have been developed and refined over decades, employing a diverse array of astronomical phenomena such as Cepheid Variables, red-giant stars, supernovae (SNe), gravitational lenses, galaxies, and the Cosmic Microwave Background (CMB). Among these, the SH0ES Cepheid-SN distance ladder yields the most precise cosmological constraints independent of specific cosmological models, with a value of $73.2 \pm 1.7 kms^{-1}Mpc^{-1}$ (RIESS et al., 2022). Conversely, the most stringent constraints are derived from the Planck CMB data, offering a value of $67.4 \pm 0.5 kms^{-1}Mpc^{-1}$ (Planck Collaboration 2018), under the assumption of a standard ΛCDM cosmological model. This discrepancy between measurements is called Hubble Tension, currently, it is estimated to be at $4 - 5\sigma$ level. Figure 1.2 shows different measurements of H_0.

Several endeavors have been made to reconcile the two results through new physics, or improved astrophysical, experimental, and statistical modeling (FREEDMAN, 2021; FREEDMAN; MADORE, 2010). One of these attempts is the use of gravitational waves as a standard siren, analog to standard candles. The GW analysis provides a direct way to estimate the luminosity distance at cosmological scales, without the need for any intermediate astronomical distance measurements (FEENEY et al., 2019; FISHBACH et al., 2019; HOLZ; HUGHES, 2005; Schutz, 1986). To determine the distance, the signal must be observed by a worldwide network of three detectors, preferably four (Schutz, 1986). Nowadays, there are two detectors with 4 km arm-length, the LIGOs, two detectors with 3 km arm-length, the Virgo, and KAGRA (Japan), and one with a 600 m arm-length, the GEO600. Third-generation ground-based interferometers in the project, the Einstein Telescope (ET) and Cos-

mic Explorer (CE), will have 10 km and 40 km arm-lengths, respectively, and significantly enhanced sensitivity to detect farther sources. Besides those, there is LISA, the first space-based observatory dedicated to studying gravitational waves of low frequency (LISA CONSORTIUM,). GW170817 provided proof of the principle that the standard siren technique could measure the Hubble constant.

In this thesis, we explore the use of standard sirens through DALI (Derivative Approximation for LIkelihoods) to estimate gravitational wave (GW) parameters (GW-DALI) and cosmological parameters from compact object coalescences. This analysis employs Gaussian and Beyond-Gaussian likelihood approximations, focusing specifically on $D_L - z$ measurements of bright sirens—standard sirens with electromagnetic counterparts—within a dynamic cosmological model framework. The thesis is structured as follows: It begins with the fundamental concepts of General Relativity and Cosmology, providing the necessary background for understanding the problem. This is followed by a detailed description of Gravitational Wave theory and the data analysis methods used to address the main objectives of this work. Finally, the last chapter presents our results and conclusions.

Figure 1.1 - Hubble Constant Measurements.

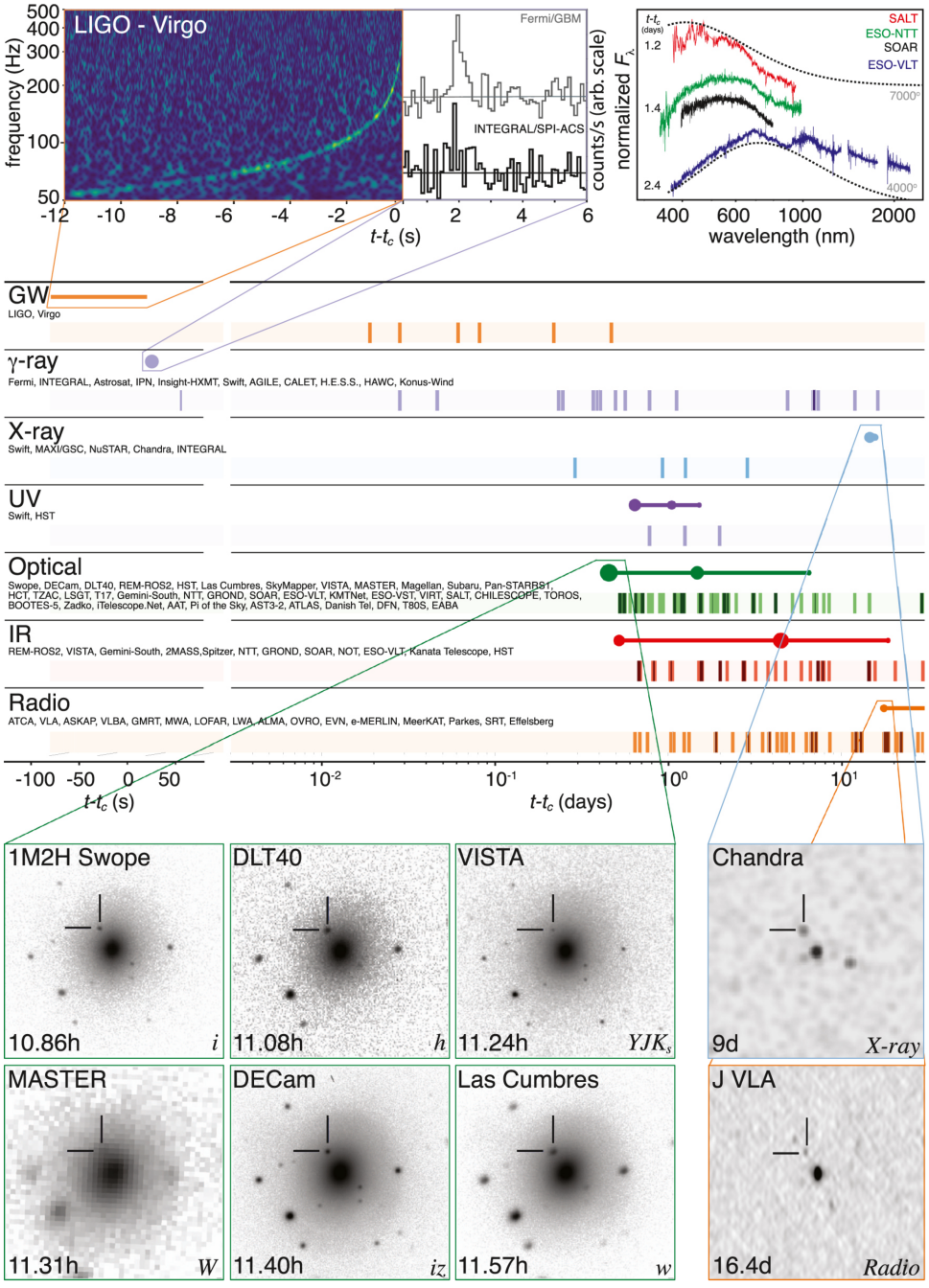

Upper left panel: The gravitational wave signal from GW170817 depicted in the time-frequency domain, alongside the associated short gamma-ray burst (GRB) independently detected by Fermi and INTEGRAL. The temporal scale is centered on the coalescence epoch ($t - t_c = 0$), illustrating a clear 1.7-second lag of the GRB trigger following the merger. Upper right panel: The nearly thermal optical spectrum of the kilonova (AT2017gfo) captured at various epochs. Central panel: A timeline detailing the discovery of the electromagnetic counterparts (GRB 170817A and AT2017gfo) throughout the follow-up campaign. Lower left panel: Visual representations of AT2017gfo and its host galaxy NGC 4993. Lower right panel: Visual representations of the X-ray and radio afterglow of GRB 170817A.

SOURCE: Stratta and Pannarale (2022).

Figure 1.2 - GW170817, GRB170817a and AT2017gfo signals.

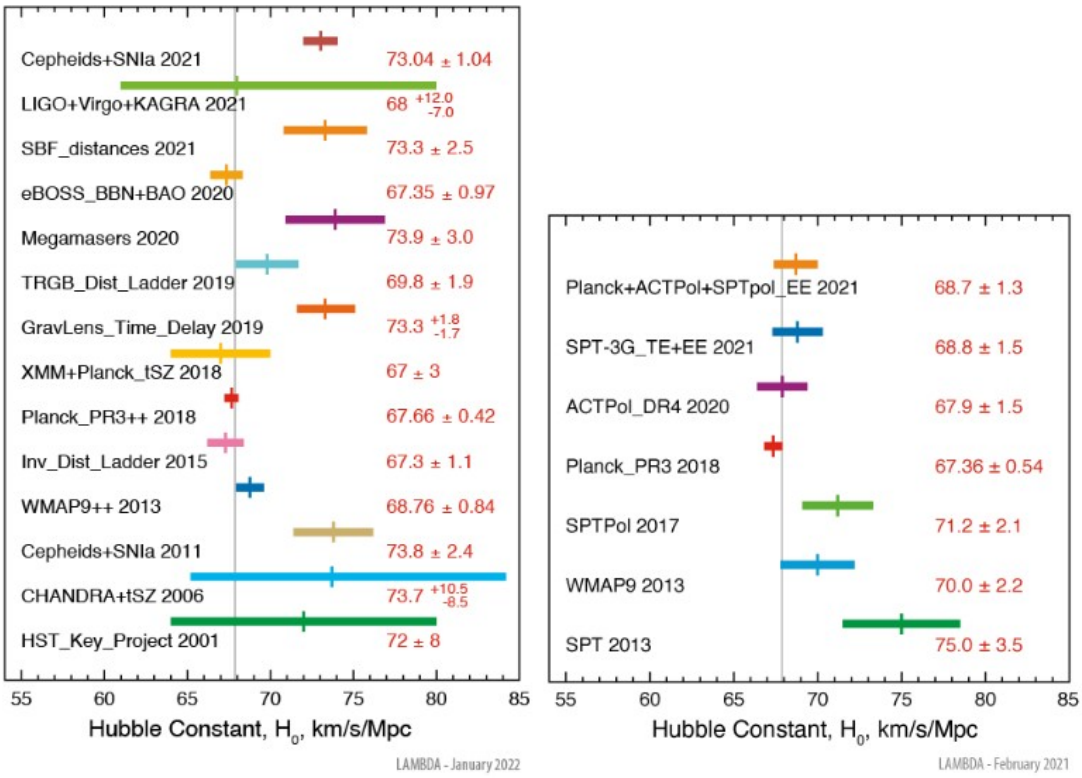

Left: the figure includes results from distance ladder determinations (labeled HST Key Project, $Cepheids + SNIa$ (2011 and 2021), TRGB Dist Ladder), indirect CMB measurements ($WMAP9++, Planck_PR3++$, both of which combine CMB with other data), BAO in combination with baryon abundance (BAO+D/H), the thermal SZ effect (CHANDRA+tSZ, XMM+Planck tsZ), strong gravitational lensing (Gravlens Time Delay) and gravitational waves (LIGO+Virgo+KAGRA). Right: This figure illustrates recent H_0 determinations using only CMB data, uncombined with lower redshift measurements.

SOURCE: NASA / LAMBDA ARCHIVE TEAM (2024).

2 FUNDAMENTAL PRINCIPLES OF GENERAL RELATIVITY AND COSMOLOGY

This section provides an introduction to the fundamental concepts of modern cosmology. It is divided into two main parts: the principles of General Relativity, focusing on elements such as the understanding and interpretation of the field equation, and the main ideas in Cosmology. The latter includes discussions on the Cosmological Principle, the Friedmann equations derived from the Friedmann-Lemaître Robertson-Walker metric, the Hubble-Lemaître law, and various definitions of cosmological distances. Additionally, this section discusses the ΛCDM model and its extensions, specifically the w_0w_aCDM model.

2.1 Principles of General Relativity

At the dawn of the 20th century, Albert Einstein formulated General Relativity (GR) in 1915 (EINSTEIN, 1915). This framework redefined gravitational interactions, which were previously described solely by Newtonian mechanics. While Newtonian gravity successfully explained planetary motion, it failed under extreme conditions, particularly in accounting for the finite propagation speed of gravitational interactions (CARROLL, 2019). Before going deeper into these equations, it is important to understand the foundational concepts and mathematical tools essential to this theory of gravity.

2.1.1 Mathematical foundations of General Relativity

The mathematical formulation of General Relativity relies on differential geometry, tensor calculus, and the theory of manifolds. A fundamental concept in GR is the four-dimensional differentiable manifold $\mathcal{M}$, representing spacetime (CARROLL, 2019; D'INVERNO, 1992). A manifold allows for local coordinate charts x^μ, where $\mu = 0, 1, 2, 3$ labels spacetime coordinates. The principle of general covariance asserts that the laws of physics should take the same form in all coordinate systems.

The metric tensor $g_{\mu\nu}$ defines the infinitesimal spacetime interval:

$$ds^2 = g_{\mu\nu}dx^\mu dx^\nu, \tag{2.1}$$

where $g_{\mu\nu}$ encodes the geometry of spacetime (CARROLL, 2019). For example, in the absence of gravitational fields, spacetime is described by Minkowski space, a flat four-dimensional spacetime used in Special Relativity. The Minkowski metric is

given by:

$$ds^2 = -c^2dt^2 + dx^2 + dy^2 + dz^2. \tag{2.2}$$

This metric describes the geometry of spacetime where inertial observers experience no gravitational effects, and the interval ds^2 remains invariant under Lorentz transformations.

- Tensor Calculus

Tensors generalize vectors and scalars to higher-dimensional spaces and are fundamental in GR since physical laws must be independent of coordinate choices. A rank-(m, n) tensor transforms as (D'INVERNO, 1992)

$$T'^{\alpha_1\ldots\alpha_m}_{\beta_1\ldots\beta_n} = \frac{\partial x^{\alpha_1}}{\partial x'^{\mu_1}} \cdots \frac{\partial x^{\alpha_m}}{\partial x'^{\mu_m}} \frac{\partial x'^{\nu_1}}{\partial x^{\beta_1}} \cdots \frac{\partial x'^{\nu_n}}{\partial x^{\beta_n}} T^{\mu_1\ldots\mu_m}_{\nu_1\ldots\nu_n}. \tag{2.3}$$

Common tensors in GR include the metric tensor $g_{\mu\nu}$, the stress-energy tensor $T_{\mu\nu}$, and the Riemann curvature tensor $R^{\rho}_{\sigma\mu\nu}$.

- Covariant Differentiation and Connections

In curved spacetime, differentiation must respect the manifold's structure. The covariant derivative ∇_μ generalizes the partial derivative and is defined using the Christoffel symbols (CARROLL, 2019):

$$\nabla_\mu T^\nu = \partial_\mu T^\nu + \Gamma^\nu_{\mu\lambda} T^\lambda. \tag{2.4}$$

The Christoffel symbols $\Gamma^\lambda_{\mu\nu}$, which describe how the coordinate basis changes from point to point, are derived from the metric tensor:

$$\Gamma^\lambda_{\mu\nu} = \frac{1}{2} g^{\lambda\sigma} \left(\partial_\mu g_{\sigma\nu} + \partial_\nu g_{\sigma\mu} - \partial_\sigma g_{\mu\nu}\right). \tag{2.5}$$

The Levi-Civita connection, a torsion-free connection, ensures that the metric is preserved under parallel transport (MISNER K. S. THORNE, 1973).

2.2 Einstein field equations

The curvature of spacetime is described by the Riemann curvature tensor (D'INVERNO, 1992):

$$R^\rho{}_{\sigma\mu\nu} = \partial_\mu \Gamma^\rho_{\nu\sigma} - \partial_\nu \Gamma^\rho_{\mu\sigma} + \Gamma^\rho_{\mu\lambda}\Gamma^\lambda_{\nu\sigma} - \Gamma^\rho_{\nu\lambda}\Gamma^\lambda_{\mu\sigma} \tag{2.6}$$

This tensor encodes the intrinsic curvature of spacetime and describes how vectors change when transported in parallel along a curved manifold.

The Ricci tensor $R_{\mu\nu}$ is obtained by contracting the first and third indices of the Riemann tensor:

$$R_{\mu\nu} = R^{\lambda}_{\mu\lambda\nu}. \tag{2.7}$$

Further contraction with the metric tensor yields the Ricci scalar R:

$$R = g^{\mu\nu} R_{\mu\nu}. \tag{2.8}$$

This scalar represents a measure of curvature at a given point in spacetime.

Relating these curvature quantities to the stress-energy tensor gives the Einstein field equations:

$$R_{\mu\nu} - \frac{1}{2} g_{\mu\nu} R + \Lambda g_{\mu\nu} = \frac{8\pi G}{c^4} T_{\mu\nu}, \tag{2.9}$$

where G is the gravitational constant, c is the speed of light, and Λ is the cosmological constant (EINSTEIN, 1915; D'INVERNO, 1992).

The right-hand side of the Einstein equations is related to the matter and energy, and it is composed of the energy-momentum tensor $T_{\mu\nu}$. The energy-momentum tensor quantitatively provides the densities and flows of energy and momentum generated by the sources present in space that will determine the geometry of spacetime (ROOS, 2003). The energy-momentum tensor $T_{\mu\nu}$ can be understood as the flow of the quadri-momentum p_{μ} through a constant surface x_{ν}

The Einstein equations predict some physical phenomena:

- Gravitational Time Dilation: Stronger gravitational fields slow down the passage of time (ASHBY, 2003).
- Gravitational Waves: Metric perturbations propagate as ripples in spacetime (ABBOTT et al., 2016).
- Black Holes and Event Horizons: Certain solutions predict regions of inescapable gravitational pull (CHANDRASEKHAR, 1983).
- Cosmological Expansion: The field equations underpin modern cosmological models (PEEBLES, 1993).

In the weak-field approximation (The weak-field approximation refers to the regime

in which the gravitational field is sufficiently weak such that the spacetime metric deviates only slightly from the flat Minkowski metric), GR should reduce to Newtonian gravity.

2.3 Cosmology

2.3.1 Cosmological principle

In the 1930s, Edward A. Milne (1896-1950) introduced a fundamental concept in modern cosmology, called the Cosmological Principle (RYDEN, 2003; BARTUSIAK, 2006). The Cosmological Principle states that, on large scales ($>$ 100 Mpc), the Universe is homogeneous and isotropic. This principle was implicitly considered in Einstein's early cosmological work (1917) and later formalized in the 1930s in the context of General Relativity (RYDEN, 2003). According to this principle, the Universe appears statistically the same to all observers who follow the Hubble flow, implying that the distribution of matter and energy is uniform at sufficiently large scales.

Homogeneity means that there is no privileged location in the Universe. Matter is evenly distributed, meaning that any observer would perceive the same number of galaxies, clusters, and superclusters regardless of their position. Isotropy, on the other hand, implies that there is no preferred direction in the Universe; it appears the same in all directions. To illustrate this concept, imagine a room with infinite walls and a light bulb in the center. If different directions of the room have the same luminosity, but there is a direction with greater luminosity where the lamp is located, then there is a lack of isotropy. Therefore, homogeneity and isotropy are not identical concepts. Figure 2.1 shows the different patterns that can arise: (a) only homogeneous, (b) only isotropic, and (c) both homogeneous and isotropic.

2.3.2 FLRW metric and Friedmann's equations

In 1922, based on the Cosmological Principle, Alexander Friedmann, a self-taught student of General Relativity, derived the first expansionist solutions to Einstein's equations (BARTUSIAK, 2006). Friedmann's model describes a dynamic, spatially homogeneous, isotropic Universe that began from a divergent matter density scenario (RYDEN, 2003). In 1927, Georges E. Lemaître independently obtained equations equivalent to Friedmann's. Unlike his colleague, Lemaitre used the physics and astronomy of the time to describe the Universe, attracting the interest of the scientific community.

Figure 2.1 - Cosmological Principle.

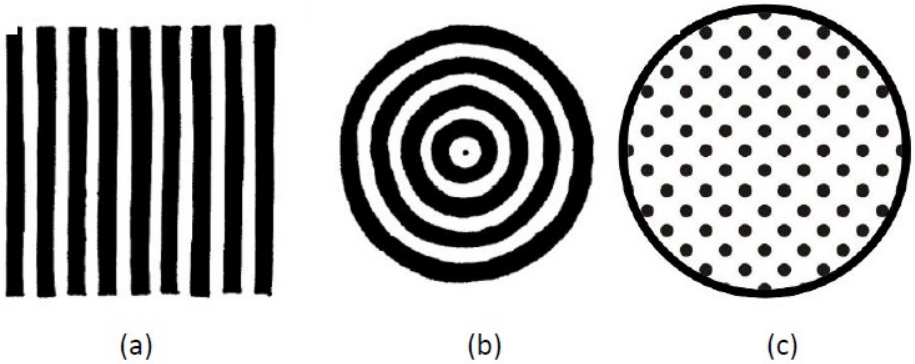

Illustrations representing what would be a: (a) homogeneous but not isotropic pattern. (b) isotropic but not homogeneous pattern for an observer at the center. (c) isotropic and homogeneous pattern.

SOURCE: Ryden (2003).

Cosmological distances are dynamic, requiring the use of comoving coordinates, which expand with the universe. They can be visualized as a grid in which galaxies remain fixed while the universe expands, as illustrated in Figure 2.2. The changes in scale due to the universe's expansion or contraction can be quantified using the scale factor $a(t)$, defined as a time-dependent function that parametrizes the expansion of the universe through the distance between galaxies:

$$a(t) \propto \text{intergalactic distance.} \tag{2.10}$$

For convenience, $a(t)$ is normalized such that $a(t_0) = 1$ today. This normalization is only valid in a spatially flat Universe; in models with non-zero spatial curvature, rescaling $a(t_0)$ would alter the physical meaning of the curvature term K, which appears in the metric as $K/a(t)^2$ Distances at different epochs relate via:

$$a(t) = \frac{R(t)}{R_0}, \tag{2.11}$$

where $R(t)$ is the proper distance at time t, and R_0 is the present-day comoving distance. The metric describing a homogeneous, isotropic universe is the Friedmann-Lemaître-Robertson-Walker (FLRW) metric:

$$ds^2 = -c^2dt^2 + a^2(t)\left[\frac{dr^2}{1-Kr^2} + r^2(d\theta^2 + \sin^2\theta d\phi^2)\right], \tag{2.12}$$

Figure 2.2 - Scale Factor.

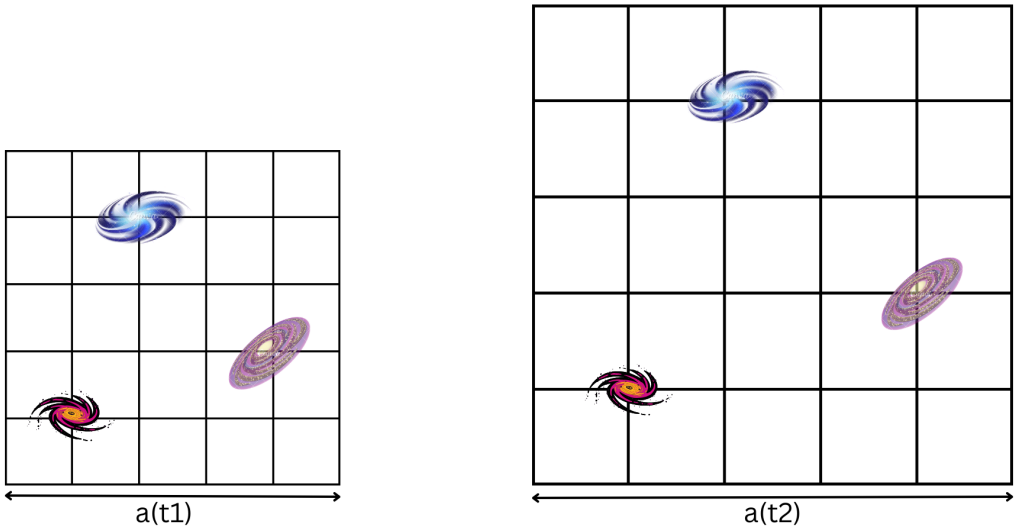

Illustration showing the evolution of the scale factor over time. The black grids represent the comoving coordinates, and note that galaxies appear "stuck" to the grid.

SOURCE: Author.

where K is called the curvature parameter, $K = +1, 0, -1$ represents closed, flat, or open spatial geometry, respectively.

By inserting the FLRW metric into of Einstein's equations, and assuming that the energy-matter in the Universe behaves like a perfect fluid [1] it is possible to derive a dynamical equation known as Friedmann's equation:

$$H^2 = \frac{8\pi G}{3}\rho(t) - \frac{K}{a^2(t)} \tag{2.13}$$

where $H = \dot{a}/a$ is the Hubble parameter. The density term is the sum of all energetic components of the Universe ($\rho(t) = \sum_i \rho_i(t)$. For a given value of the Hubble

[1] A perfect fluid in cosmology is described by the energy-momentum tensor of the form $T^{\mu\nu} = (\rho + p)u^\mu u^\nu + pg^{\mu\nu}$, where ρ represents the energy density, p is the isotropic pressure, u^μ is the four-velocity of the fluid, and $g^{\mu\nu}$ is the spacetime metric tensor. This formulation assumes the absence of viscosity and heat conduction and is widely used to model cosmic components such as radiation, matter, and dark energy in relativistic cosmology (WEINBERG, 1972).

parameter, there is a critical density $\rho_c(t)$, defined by

$$\rho_c(t) = \frac{3H(t)^2}{8\pi G}. \tag{2.14}$$

Defining the density parameter $\Omega_i = \rho_i(t)/\rho_c(t)$, the second Friedmann equation describing energy conservation is:

$$\dot{\rho} = -3H(\rho + P). \tag{2.15}$$

2.3.3 Hubble-Lemaître law

In the past, when the Universe was considered to be stationary, it was predicted that galaxies could move randomly. However, Edwin Hubble[2], assisted by Milton Humason, observed, using Cepheid Variables[3], that most galaxies showed a redshift (some blue). A redshift (or blueshift) is a change in the spectrum of electromagnetic waves toward longer (or shorter) wavelengths, indicating a movement toward the red (or blue) side of the spectrum, respectively.

Hubble and Humason (1929) confirmed a linear relation between redshift and distance, now known as the Hubble-Lemaître Law (RYDEN, 2003):

$$v = H_0 D. \tag{2.16}$$

The observed redshift in an expanding universe results from three effects:

- Doppler shift (peculiar velocity)
- Gravitational redshift (gravitational potential differences)
- Cosmological redshift (metric expansion)

[2]Vesto Slipher was the first to calculate the speed with which Andromeda approaches the Earth, as well as the speed of 2004 galaxies, although in 1910 galaxies were called spiral nebulae, interpreted as solar systems in formation (BARTUSIAK, 2006). In 1927, George Lemaître used a list containing 42 galaxies for which the wavelength shift had been calculated by Slipher and concluded that the high velocities found (well above the velocity of the stars in the Milky Way) could be the result of the expansion of the Universe

[3]Cepheid variables are high-luminosity supergiant stars [$L_\odot$ = 400000 (solar luminosity)] and periodically variant luminosities (RYDEN, 2003)

The redshift is defined mathematically by the equation (RYDEN, 2003):

$$z = \frac{\lambda_o - \lambda_e}{\lambda_e} \tag{2.17}$$

where λ_o e λ_e represent the wavelengths of the light observed and emitted, respectively. The value of the redshift can also be related to distance by Hubble-Lemaître Law, expressed as:

$$z = \frac{v}{c} = \frac{H_0 D}{c} \tag{2.18}$$

Observational data confirm the relationship between redshift and luminosity distance[4]. Figure 2.3 illustrates the relationship between the luminosity distance (d_L) and the redshift (z), using data from Union2.1, one of the largest catalogs of supernova Ia. This relationship is essential for understanding the expansion of the Universe and validating cosmological models.

[4]Luminosity distance is a measure of distance used to describe the relationship between the intrinsic luminosity (or power emitted) of an astronomical object and its observed flux (brightness), better discussed on the next section.

Figure 2.3 - Relationship between luminosity distance (d_L) and redshift (z).

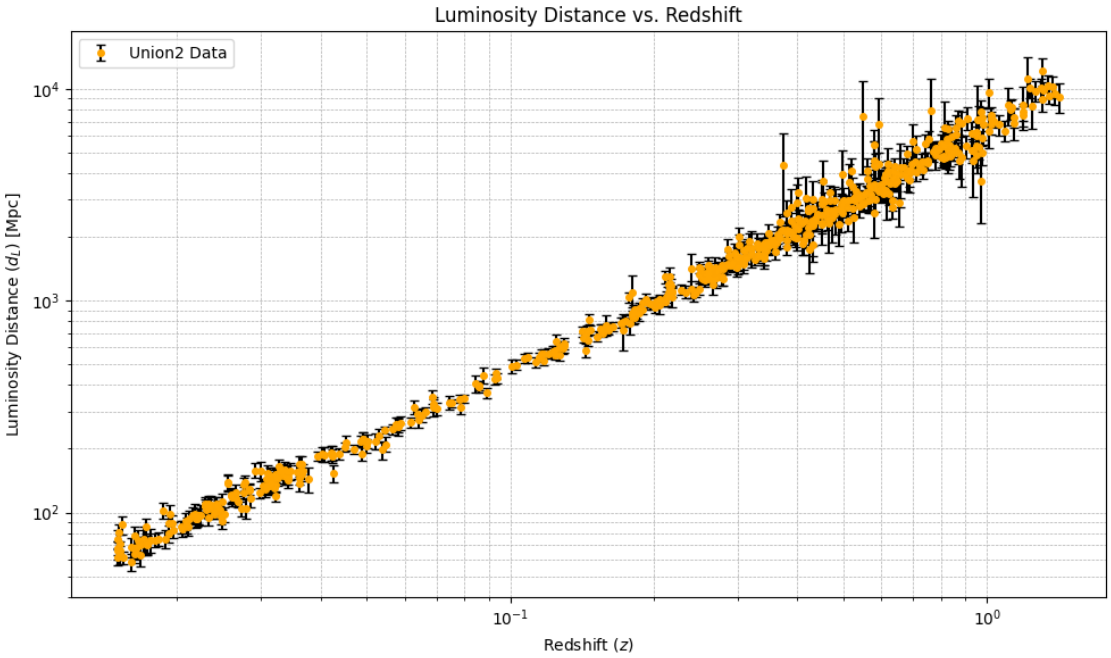

Relationship between luminosity distance (d_L) and redshift (z) for supernovae from the Union2.1 catalog (SUZUKI et al., 2012). The error bars are shown in pink, while the observed values are represented in orange.

SOURCE: Author.

In this context, the Hubble constant can be calculated by dividing the speed by the distance, and its unit is $km.s^{-1}Mpc^{-1}$. If the galaxies are currently moving apart, this implies that they were very close together in the past. Therefore, the time elapsed since they were very close can be defined as:

$$t_0 = \frac{1}{H_0} \tag{2.19}$$

Hubble's time (t_0) represents the current age of the Universe, calculated as approximately (13.74 ± 0.40) billion years (RYDEN, 2003). This value is in line with the age of the oldest astronomical objects ever observed. In addition, since "objects" with large redshift values indicate a period when the Universe had a small scale factor, while small redshift values suggest more recent eras, it is possible to establish a relationship between the redshift (z) and the scale factor. Let's take an electromagnetic signal emitted by an object of coordinates (r, θ, ϕ), at the instant t_e the first peak

is emitted, at the instant $t_e + \delta t_e$ a second peak is emitted. Both are observed by the observer with coordinates (0,0,0) at the instant t_0 and $t_0 + \delta t_0$, respectively. The light signal travels along a null geodesic ($ds^2 = 0$), where θ and ϕ are constants. Through the definition of the scalar factor we have that:

$$1 + z = \frac{\lambda_o}{\lambda_e} = \frac{a(t_o)}{a(t_e)} \tag{2.20}$$

This implies that the wavelength of the signal are stretching due the cosmic expansion, by a factor equal to the ratio between the scale factor at the time of emission and observation (ROOS, 2003).

Accurate determination of astronomical distances is fundamental to understanding the scale, structure, and evolution of the universe. Over time, astronomers have developed a series of interconnected methods known as the cosmic distance ladder, each building on the precision of the previous to reach greater distances. These methodologies, coupled with alternative approaches like the inverse distance ladder, have become central to modern cosmology.

To better understand, the cosmic distance ladder is a hierarchical method used to determine astronomical distances, addressing the challenge that no single method can measure distances across all cosmic scales. Each "rung" of the ladder relies on calibrations from the preceding one (RIESS et al., 2022). For instance, the SH0ES team calibrated the luminosities of Classical Cepheids using parallaxes, maser distances to NGC 4258, and detached eclipsing binaries in the Large Magellanic Cloud (RIESS et al., 1998). These Cepheid measurements then served to calibrate Type Ia supernovae, which act as "standard candles" for measuring even greater distances. Standard candles, such as Cepheids and supernovae, have well-defined luminosity properties that allow their distances to be determined by comparing intrinsic and observed brightness.

Challenges in using standard candles include accurate calibration of their absolute brightness and ensuring precise categorization to avoid misclassifications. Type Ia supernovae, critical for distances beyond 10^8 light-years, are particularly valuable due to their uniform luminosity and consistent light curve patterns, enabling precise distance measurements by analyzing peak brightness and light curve evolution.

An alternative approach, the inverse distance ladder, begins with the Cosmic Microwave Background (CMB) (CAMARENA; MARRA, 2020). Here, the sound horizon (a standard ruler) is imprinted as acoustic peaks in the CMB's angular power

spectrum. By measuring the angular diameter distance to the CMB surface and applying cosmological models, researchers can estimate key parameters like matter density and the Hubble parameter.

However, these methodologies have highlighted a growing discrepancy, the Hubble tension. Using the cosmic distance ladder, measurements of the Hubble constant (H_0) yield a value systematically higher than the value derived from the inverse distance ladder using CMB data. A recent hypothesis, termed the "local bubble effect," suggests that this tension might be partly due to our location within an underdense region of the universe (HUTERER; WU, 2024). Complementarily, recent results from the DESI survey, when interpreted through a fundamental physics lens, provide independent motivation for questioning the ΛCDM model. In particular, Brandenberger argues that a constant dark energy density — as assumed in ΛCDM — may be theoretically inconsistent, based on the Trans-Planckian Censorship Conjecture and swampland criteria, and that current observations favor a time-dependent dark energy component (BRANDENBERGER, 2025). Such efforts highlight the complementary nature of these distance measurement techniques and the challenges of unifying them under a consistent framework.

2.3.4 Distance in cosmology

In cosmology, there are several types of distances used to describe the vast scales of the universe and the relationships between celestial bodies. Here are some of the different types of distances commonly used.

2.3.4.1 Comoving distance

The concept of comoving quantities is related to the quantities that remain unchanged with the expansion of the Universe (RYDEN, 2003; HOGG, 2000). Since it is the space itself that is expanding, we can define a type of distance called the comoving distance, which remains constant. The comoving distance δD_C is a measure of the separation between two objects in the Universe that remains constant over time if both objects move with the Hubble flow (RYDEN, 2003). In other words, it represents the distance that would be observed between them at the time of observation (the proper distance), adjusted for the ratio of the scale factor of the Universe at that time to its current value. Mathematically, it equals the proper distance multiplied by $(1 + z)$, where z is the redshift There are two types of comoving distance: the Line-of-Sight and the Transverse. These distances are derived directly from the spacetime interval using the FLRW metric.

To calculate the total line-of-sight comoving distance D_C from us to a distant object, one needs to integrate the infinitesimal contributions δD_C between nearby events along the radial ray from $z = 0$ to the object's redshift. The line-of-sight comoving distance, or simply comoving distance D_C, is defined as such.

$$D_C = \int_0^z c\frac{dz}{H(z)} \tag{2.21}$$

The transverse comoving distance, denoted as D_M, represents the spatial separation between two points in the universe along a path perpendicular to the line of sight, accounting for the universe's expansion (HOGG, 2000). Unlike the line-of-sight comoving distance, which is measured along the direction of observation, the transverse comoving distance is measured perpendicular to this line. It provides a crucial measure for understanding the universe's geometry and is often used in cosmological calculations and models to describe the spatial distribution of celestial objects. The transverse comoving distance is defined as

$$D_M = \frac{1}{\sqrt{K}} sin\left[\sqrt{K}\int_0^z c\frac{dz}{H(z)}\right] = \frac{D_H}{\sqrt{\Omega_{k,0}}} sinh\left[\frac{\sqrt{\Omega_{K,0}}}{D_H}\int_0^z c\frac{dz}{H(z)}\right] \tag{2.22}$$

Where $D_H = \frac{1}{H_0}$ is the Hubble Distance, K is the curvature parameter, and $\Omega_{K,0}$ is the density parameter associated with the spatial curvature.

2.3.4.2 Angular diameter distance

The angular diameter distance, denoted as D_A, represents the relationship between the physical transverse size of an object and its angular size (measured in radians). This distance measure is essential for converting angular separations observed in telescope images into proper separations at the source. Notably, D_A is characterized by a unique feature: it does not increase indefinitely as a redshift (z) approaches infinity. Instead, it reaches a maximum turnover point at around $z \sim 1$, beyond which more distant objects appear larger in angular size. The angular diameter distance is intricately connected to the transverse comoving distance, with the relationship given by

$$D_A = \frac{D_M}{1+z} \tag{2.23}$$

2.3.4.3 Luminosity distance

The luminosity distance d_L is defined by the relationship between the bolometric flux S (integrated over all frequencies) and the bolometric luminosity L:

$$d_L = \sqrt{\frac{L}{4\pi S}} \tag{2.24}$$

We can also relate this to the transverse comoving distance and angular diameter distance by

$$d_L = (1+z)D_M = (1+z)^2 D_A \tag{2.25}$$

2.3.5 The Universe

2.3.5.1 Dark matter

Dark matter was first inferred by Zwicky (1933) from galaxy cluster dynamics (ZWICKY, 1933). Rubin and Ford (1970s) further confirmed its presence through galaxy rotation curves (RUBIN; FORD, 1970). It is one of the greatest mysteries in modern astrophysics. Despite not emitting, absorbing, or reflecting light, it exerts significant gravitational influence in the universe. According to astrophysical observations, about 27% of the total composition of the universe is attributed to dark matter (RYDEN, 2003).

Today, dark matter is studied not only through galactic dynamics but also via phenomena such as gravitational lensing (BARTELMANN; SCHNEIDER, 2001). Dark matter can be classified into two main categories based on the thermal velocity of the particles and their influence on the universe's structure (RYDEN, 2003). Cold Dark Matter (CDM) consists of massive particles that move slowly and are essential for the formation of structures like galaxies and galactic clusters. Hot Dark Matter (HDM), composed of very light and fast particles such as neutrinos, is insufficient to explain the formation of larger structures.

Several theoretical models have been proposed to explain the nature of dark matter. Among them are Weakly Interacting Massive Particles (WIMPs), hypothetical subatomic particles interacting only through gravitational and weak forces (BERTONE et al., 2005). Another proposal is the Axion, an extremely light particle that can form large-scale quantum condensates (MARSH, 2016).

2.3.5.2 The ΛCDM model

The ΛCDM (Lambda-Cold Dark Matter) model is the prevailing paradigm in modern cosmology, offering a coherent description of the Universe's evolution. It integrates the cosmological constant Λ, originally introduced by Einstein in the framework of general relativity (EINSTEIN, 1917), with cold dark matter (CDM), forming the foundation for explaining large-scale observations, such as the cosmic microwave background (CMB) (PENZIAS; WILSON, 1965; AGHANIM et al., 2020), galaxy distribution (TEGMARK et al., 2004), and the Universe's accelerated expansion (PERLMUTTER et al., 1999; RIESS et al., 1998).

The model is governed by the Friedmann equation, which describes the expansion dynamics of a homogeneous and isotropic Universe:

$$H^2(a) = H_0^2 \left[\Omega_r a^{-4} + \Omega_m a^{-3} + \Omega_k a^{-2} + \Omega_\Lambda\right], \tag{2.26}$$

where $H(a)$ is the Hubble parameter as a function of the scale factor a, H_0 is the present-day value of the Hubble parameter;Ω_r, Ω_m, Ω_k, and Ω_Λ are the density parameters for radiation, matter, spatial curvature, and dark energy, respectively.

The cosmological constant Λ is linked to dark energy, which drives the Universe's accelerated expansion, as confirmed by Type Ia supernova observations (PERLMUTTER et al., 1999; RIESS et al., 1998). Dark energy constitutes approximately 68% of the Universe's total energy budget, while cold dark matter and baryonic matter contribute about 27% and 5%, respectively (AGHANIM et al., 2020).

2.3.5.3 The w_0w_aCDM model

The w_0w_aCDM model extends ΛCDM by allowing for a time-dependent dark energy equation of state. Unlike the ΛCDM model, which assumes a constant equation of state parameter $w = -1$, the w_0w_aCDM model parametrizes the evolution of w as:

$$w(a) = w_0 + w_a(1 - a), \tag{2.27}$$

where w_0 is the present-day value of the dark energy equation of state; w_a describes the rate of change of w with time; and a is the scale factor, normalized such that $a = 1$ today.

This formulation allows for deviations from the cosmological constant model, where $w_0 = -1$ and $w_a = 0$. A commonly used case of this parameterization is the

Chevallier-Polarski-Linder (CPL) model (CHEVALLIER et al., 2001; LINDER, 2003), which is designed to capture possible time evolution in the dark energy component with a minimal set of parameters. The CPL parametrization is sometimes alternatively written as:

$$w(a) = w_0 + w_a \left(\frac{a-1}{a} \right). \tag{2.28}$$

This expression is mathematically equivalent to the standard form through the identity $\frac{a-1}{a} = -\frac{1-a}{a}$, which emerges when the original CPL model, typically written as $w(z) = w_0 + w_a \frac{z}{1+z}$, is re-expressed in terms of the scale factor via the relation $z = \frac{1}{a} - 1$. Both forms describe the same physical model and converge to w_0 as $a \to 1$, with the parameter w_a encoding the first-order deviation from a constant equation of state.

The Hubble parameter in the $w_0 w_a$CDM model is expressed as:

$$H^2(a) = H_0^2 \left[\Omega_m a^{-3} + \Omega_r a^{-4} + \Omega_k a^{-2} + \Omega_{\mathrm{DE}}(a) \right], \tag{2.29}$$

but with a time-dependent dark energy density parameter:

$$\Omega_{\mathrm{DE}}(a) = \Omega_{\mathrm{DE},0} \exp \left[3 \int_a^1 \frac{1 + w(a')}{a'} \, da' \right]. \tag{2.30}$$

This formulation captures the potential time evolution of dark energy, distinguishing the $w_0 w_a$CDM model from the standard ΛCDM paradigm (LINDER, 2003).

The $w_0 w_a$CDM model can contribute to resolving cosmological discrepancies, such as the tension in Hubble constant measurements between early and late-Universe probes. By incorporating a dynamic dark energy component, this model allows for possible variations in cosmic acceleration, potentially reconciling differences in expansion rate estimates (RIESS et al., 2019; WONG et al., 2020). Despite its conceptual advantages, the $w_0 w_a$CDM model presents challenges in constraining w_a due to observational limitations. Current data remain largely consistent with the standard ΛCDM framework, making it difficult to detect deviations. However, next-generation surveys, such as the Vera C. Rubin Observatory's Legacy Survey of Space and Time (LSST) and the Euclid mission, are expected to enhance constraints on w_0 and w_a, improving our understanding of dark energy (LEGACY COLLABORATION, 2021; EUCLID CONSORTIUM, 2020).

3 GRAVITATIONAL WAVES

Gravitational Waves are distortions in the fabric of spacetime, much like the distortion that forms on the surface of a pond when you throw in a stone. However, instead of water, these waves travel through spacetime itself. It arises from the motion of mass-energy forms, much like how electromagnetic waves emerge from moving electric charges. This chapter covers the theoretical foundations, polarization states, and role of gravitational waves in cosmology.

3.1 Linearized field equations

Einstein's field equations are non-linear, meaning that you cannot simply add up solutions as you might with ordinary linear equations. Moreover, computing the Riemann tensor in strongly curved spacetime requires dealing with intricate second-order partial differential equations (MILLER; YUNES, 2021). To simplify the analysis in weak-field approximations, we introduce the small perturbation $h_{\mu\nu}$. Thus, the metric is written as

$$g_{\mu\nu} = \eta_{\mu\nu} + h_{\mu\nu}, \tag{3.1}$$

with the condition $|h_{\mu\nu}| \ll 1$. This assumption allows us to treat $h_{\mu\nu}$ as a small perturbation superimposed on an otherwise smooth spacetime background, valid in the weak-field limit (MAGGIORE, 2008). Since $h_{\mu\nu}$ is small, we ignore any terms that are quadratic or higher in $h_{\mu\nu}$, which simplifies Einstein's equations.

The Christoffel symbols (first order $h_{\mu\nu}$) are:

$$\Gamma^{\rho}_{\mu\nu} = \frac{1}{2}\eta^{\rho\lambda}\Big(\partial_\mu h_{\lambda\nu} + \partial_\nu h_{\lambda\mu} - \partial_\lambda h_{\mu\nu}\Big). \tag{3.2}$$

Note that we have already omitted any second-order contributions in $h_{\mu\nu}$. The Riemann curvature tensor simplifies to:

$$R_{\mu\nu\rho\sigma} = \frac{1}{2}\left(\partial_\nu\partial_\rho h_{\mu\sigma} + \partial_\mu\partial_\sigma h_{\nu\rho} - \partial_\mu\partial_\rho h_{\nu\sigma} - \partial_\nu\partial_\sigma h_{\mu\rho}\right), \tag{3.3}$$

with all indices lowered using the flat Minkowski metric (MAGGIORE, 2008). The Ricci tensor $R_{\mu\nu}$ is obtained by contracting the Riemann tensor:

$$R_{\mu\nu} = R^{\rho}_{\mu\rho\nu} = \frac{1}{2}\left(\partial_\sigma\partial_\mu h^{\sigma}_{\nu} + \partial_\sigma\partial_\nu h^{\sigma}_{\mu} - \partial_\mu\partial_\nu h - \Box h_{\mu\nu}\right), \tag{3.4}$$

where the trace $h = \eta^{\mu\nu}h_{\mu\nu}$, and the D'Alembertian operator is $\Box = \eta^{\mu\nu}\partial_\mu\partial_\nu$

To simplify the field equations further, we define:

$$\bar{h}_{\mu\nu} = h_{\mu\nu} - \frac{1}{2}\eta_{\mu\nu}h. \tag{3.5}$$

This redefinition allows us to recast the Einstein equations into a more manageable form:

$$\Box\bar{h}_{\mu\nu} + \eta_{\mu\nu}\partial^\rho\partial^\sigma\bar{h}_{\rho\sigma} - \partial^\rho\partial_\nu\bar{h}_{\mu\rho} - \partial^\rho\partial_\mu\bar{h}_{\nu\rho} = -\frac{16\pi G}{c^4}T_{\mu\nu}. \tag{3.6}$$

General Relativity permits a great deal of gauge freedom, so we can impose additional conditions on the metric perturbation without altering the underlying physics. A particularly effective choice is the harmonic gauge, also known as the Lorenz gauge. The gauge condition is:

$$\partial^\nu\bar{h}_{\mu\nu} = 0. \tag{3.7}$$

When this condition is applied, several terms in the previous equation vanish, reducing it to the gravitational waves equation:

$$\Box\bar{h}_{\mu\nu} = -\frac{16\pi G}{c^4}T_{\mu\nu}. \tag{3.8}$$

In vacuum ($T_{\mu\nu}$), this further simplifies:

$$\Box\bar{h}_{\mu\nu} = 0. \tag{3.9}$$

A crucial property of the Lorenz gauge condition 3.7 is that, even after imposing it, we can still perform an additional gauge transformation (only in vacuum). For a detailed discussion, see (SOUZA, 2023). By exploiting this residual gauge freedom, the number of independent components of $\bar{h}_{\mu\nu}$ is further reduced from six to two. These two remaining degrees of freedom correspond to the physical radiative polarization states of gravitational waves, which will be discussed in the following section.

3.2 Plane gravitational waves

For the detection and analysis of gravitational waves, we focus on radiative solutions of Equation (3.9). Since the d'Alembertian operator ($\Box$) describes wave propagation at the speed of light, the general solution satisfies the superposition principle and can be expressed as a sum of plane waves:

$$\bar{h}_{\mu\nu} = \Re\left(A_{\mu\nu}e^{ik_\rho x^\rho}\right), \tag{3.10}$$

Where $A_{\mu\nu}$ is a complex amplitude tensor, and k^μ is the wave vector, which consists of the gravitational wave angular frequency ω and the spatial wave components k^i.

Substituting the solution (3.10) into the wave Equation (3.9), we obtain the dispersion relation:

$$k^\rho k_\rho = \eta_{\rho\sigma} k^\rho k^\sigma = 0. \tag{3.11}$$

This shows that the wave vector is null (lightlike), confirming that gravitational waves propagate at the speed of light ($v = c$).

Additional constraints arise from the Lorenz gauge condition 3.7. Applying it to the plane wave solution (3.10), we obtain:

$$k^\rho A_{\mu\rho} = 0. \tag{3.12}$$

This condition implies that the amplitude tensor $A_{\mu\nu}$ is orthogonal to the wave vector, further reducing the number of independent components. By imposing further gauge conditions on the metric perturbation, we arrive at the harmonic gauge. In this gauge, the independent components satisfy:

$$\bar{h}_{0\mu} = 0, \quad \bar{h}^i_i = 0, \quad \partial^i \bar{h}_{ij} = 0. \tag{3.13}$$

Where the indexes i and j indicate the spatial coordinates. These constraints simplify the gravitational wave structure, leading to the Transverse-Traceless (TT) gauge. The perturbation metric on this specific gauge is denoted by h^{TT}_{ij}. Assuming a plane monochromatic gravitational wave propagating, the solution is

$$h^{TT}_{ij}(x) = e_{ij}(\mathbf{k}) e^{ikx} \tag{3.14}$$

Here $e_{ij}(\mathbf{k})$ is called the polarization tensor. For a single plane wave with a given wave-vector $\mathbf{k}$, $\hat{n} = \mathbf{k}/|\mathbf{k}|$. Considering that $\hat{n}$ is along the z-axis, and that h_{ij} is symmetric and traceless, we have

$$h^{TT}_{ij} = \begin{bmatrix} h_+ & h_\times & 0 \\ h_\times & -h_+ & 0 \\ 0 & 0 & 0 \end{bmatrix}_{ij} \cos(\omega(t - z/c)) \tag{3.15}$$

3.3 Multipole expansion

To analyze the gravitational wave field produced by a localized source, one can employ a multipole expansion that decomposes the field into contributions from various moments of the mass distribution. In this approach, the solution to the wave equation can be expressed using a Green's function method. Computing the Green's function, one can show that the solution of the GW equation can be given by (MAGGIORE, 2008):

$$h_{\mu\nu}(t, \mathbf{x}) = 4G \int d^3x' \frac{T_{\mu\nu}(t - |\mathbf{x} - \mathbf{x}'|/c, \mathbf{x}')}{|\mathbf{x} - \mathbf{x}'|}. \tag{3.16}$$

where $T_{\mu\nu}$ is the energy-momentum tensor of the source. Since we are interested in the far-field region where $|\mathbf{x}| >> |\mathbf{x}'|$, the denominator in Equation (3.16) can be expanded in a Taylor series, and then it can obtained by applying the projector tensor $\Lambda_{i,j,kl} = P_{ik}P_{jl} - \frac{1}{2}P_{ij}P_{kl}$, where $P_{ij} = \delta_{ij} - n_i n_j$ is the vectorial projector tensor in a given direction $\mathbf{n} = \mathbf{x}/|\mathbf{x}|$.

Substituting Equation 3.16 we obtain:

$$h_{ij}^{TT} = \frac{4G}{r}\Lambda_{i,j,kl} \int d^3x' T^{kl}(\mathbf{x}', t_r + \mathbf{x}'.\mathbf{n}) \tag{3.17}$$

Where $t_r = t - r$ is the retarded time. Expanding Equation 3.17 around the retarded time and defining the quadrupole moment M^{ij} as

$$M^{ij} = \int T^{00} x^i x^j d^3x, \tag{3.18}$$

the Quadrupole Formula at leading order is

$$h_{ij}^{TT}(t, \mathbf{x})|\text{quadrupole} = \frac{2G}{r}\Lambda i, j, kl\ddot{M}^{kl}(t_r). \tag{3.19}$$

The expression above represents the leading-order contribution to the gravitational waveform in a multipolar expansion. Here, *leading order* refers to the dominant term in an expansion in powers of the small parameter $\epsilon \sim v/c$, where v is the typical velocity of the source and c is the speed of light. This expansion is valid in the weak-field, slow-motion regime of General Relativity and is analogous to the post-Newtonian expansion. In this context, the quadrupole term is the first non-vanishing contribution to gravitational radiation.

The lowest-order term in the multipole expansion is the monopole term, which rep-

resents the total mass M of the system. However, in General Relativity, mass-energy conservation prevents monopole radiation because this term remains constant. The next term, the dipole moment, describes the center of mass of the system. Since the total momentum of an isolated system is conserved, dipole radiation is also suppressed. The quadrupole term is, therefore, the dominant source of gravitational radiation. Higher-order multipoles, such as the octupole and higher moments, introduce additional corrections to the gravitational wave signal, but their contributions are typically much weaker than those of the quadrupole term.

3.4 Gravitational Waves Polarization

To determine the gravitational wave polarizations, we analyze the quadrupole radiation from a binary system and decompose the resulting metric perturbation into its transverse-traceless (TT) components. This approach allows us to compute the waveforms observed by a distant detector.

We begin by defining the system's fundamental quantities:

$$\bar{r}_0 = (x_0, y_0, z_0) \equiv \bar{x}_1 - \bar{x}_2 \quad \text{(relative distance)}, \tag{3.20}$$

$$\bar{R}_{CM} = (x_{CM}, y_{CM}, z_{CM}) \equiv \frac{m_1\bar{x}_1 + m_2\bar{x}_2}{m_1 + m_2} \quad \text{(center of mass)}, \tag{3.21}$$

$$M = m_1 + m_2 \quad \text{(total mass)}, \tag{3.22}$$

$$\mu = \frac{m_1 m_2}{m_1 + m_2} \quad \text{(reduced mass)}. \tag{3.23}$$

The energy density T^{00} in the center-of-mass frame is given by:

$$T^{00} = \mu, \delta(x - x_0)\delta(y - y_0)\delta(z - z_0). \tag{3.24}$$

Since the center-of-mass motion does not contribute to gravitational wave emission, it is excluded from the expression. Following (MAGGIORE, 2008), under the circular orbit approximation, the relative position of each is given by

$$x_0 = R\cos\left[\Phi_s(t) + \varphi_0\right], \tag{3.25}$$

$$y_0 = R\sin\left[\Phi_s(t) + \varphi_0\right], \tag{3.26}$$

where R is the orbital radius, $\Phi_s(t)$ is the orbital phase evolving as

From these expressions, we compute the quadrupole moment components and their

second time derivatives. Since the motion is confined to the §†-plane, the mass quadrupole component along the z-axis vanishes ($\ddot{M}^{33} = 0$). The leading components of the second derivative of the quadrupole moment are:

$$\ddot{M}^{11} = -\ddot{M}^{22} \approx 2\mu R^2 \dot{\Phi}_s^2 \cos(2\Phi_s), \tag{3.27}$$

$$\ddot{M}^{12} \approx 2\mu R^2 \dot{\Phi}_s^2 \sin(2\Phi_s). \tag{3.28}$$

where $\Phi_s = \Phi_s(t) + \varphi_0$. These expressions allow us to write the transverse-traceless (TT) components of the quadrupole moment as

$$\ddot{M}^{TT} = 2\mu (R\dot{\Phi}_s)^2 \begin{bmatrix} \cos(2\Phi_s) & \sin(2\Phi_s) & 0 \\ \sin(2\Phi_s) & -\cos(2\Phi_s) & 0 \\ 0 & 0 & 0 \end{bmatrix}. \tag{3.29}$$

Using this quadrupole tensor, the gravitational wave strain h_{ij}^{TT} at a distance r is given by

$$\mathbf{h}^{TT} = \frac{4}{r}\,\eta\,(GM)^{5/3}(\pi f_{gw})^{2/3} \begin{bmatrix} \cos(2\Phi_s) & \sin(2\Phi_s) & 0 \\ \sin(2\Phi_s) & -\cos(2\Phi_s) & 0 \\ 0 & 0 & 0 \end{bmatrix}, \tag{3.30}$$

where the gravitational wave frequency is $f_{gw} = 2f_i$. Since the quadrupole moment oscillates at twice the orbital frequency, the observed gravitational wave frequency is twice the binary's orbital frequency.

The symmetric mass ratio is defined as:

$$\eta = \frac{m_1 m_2}{(m_1 + m_2)^2} = \frac{\mu}{M}. \tag{3.31}$$

To account for the inclination of the binary's orbital plane relative to the observer, we rotate the coordinate system by an angle l around the x-axis using the rotation matrix:

$$\mathcal{R} = \begin{bmatrix} 1 & 0 & 0 \\ 0 & \cos l & -\sin l \\ 0 & \sin l & \cos l \end{bmatrix}. \tag{3.32}$$

By applying this transformation to the quadrupole moment tensor, we obtain the new components:

$$\ddot{M}^{ij}_{\text{rotated}} = \mathcal{R}^i_k(t)\,\ddot{M}^{kl}\,\mathcal{R}^j_l(t). \tag{3.33}$$

For the inclined binary, the TT components of the gravitational wave polarizations become

$$\ddot{M}_{+}^{TT} = \frac{1}{2}\left(\ddot{M}^{11} - \ddot{M}^{22}\right) = \mu(\pi R f_{gw})^2 \left(\frac{1+\cos^2 t}{2}\right)\cos(2\Phi_s), \tag{3.34}$$

$$\ddot{M}_{\times}^{TT} = \ddot{M}^{12} = \mu(\pi R f_{gw})^2 \cos t \sin(2\Phi_s). \tag{3.35}$$

Finally, defining the chirp mass as

$$M_c \equiv \mu^{3/5} M^{2/5} = \eta^{3/5} M, \tag{3.36}$$

and noting that the gravitational wave phase is $\Phi_{gw} = 2\Phi_s$, we obtain the final expressions for the gravitational wave polarizations.

$$h_{+}(t) = \frac{4}{r}\Big(G\,M_c\Big)^{5/3}\Big(\pi\, f_{\rm gw}\Big)^{2/3}\left(\frac{1+\cos^2 i}{2}\right)\cos\Big(\Phi_{\rm gw}(t,r)\Big), \tag{3.37}$$

$$h_{\times}(t) = -\frac{4}{r}\Big(G\,M_c\Big)^{5/3}\Big(\pi\, f_{\rm gw}\Big)^{2/3}\cos i\,\sin\Big(\Phi_{\rm gw}(t,r)\Big). \tag{3.38}$$

Figure 3.1 illustrates the characteristic strain patterns of h_+ and $h_\times$, showing their effects on space-time as they propagate.

Figure 3.1 - Gravitational Waves polarizations.

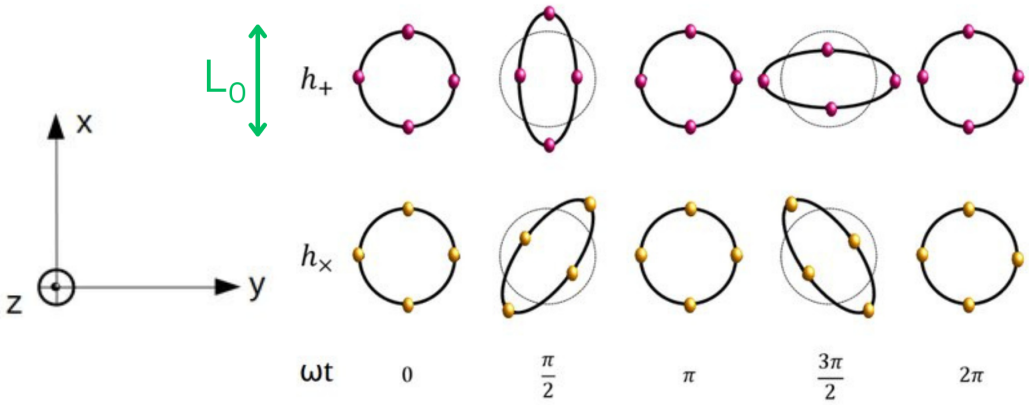

Polarizations of gravitational waves, showcasing their distinctive patterns of stretching and squeezing as they propagate through space.

SOURCE: Belahcene (2019).

3.5 Gravitational waves from binary system

Compact binary systems consist of two massive, dense astrophysical objects—either black holes or neutron stars—gravitationally bound in a relativistic orbit, emitting gravitational waves as they evolve. There are three primary subclasses of compact binary systems (ABBOTT et al., 2019): binary neutron star (BNS), binary black hole (BBH), and neutron star-black hole binary (NSBH).

Unique gravitational wave patterns are generated by each binary pair, influenced by factors such as mass, orbital orientation relative to Earth, and distance. However, the wave generation mechanism remains the same across all systems, characterized by three distinct stages: inspiral, merger, and ringdown. This process is illustrated in Figure 3.2. During the inspiral phase, two compact objects orbit each other and emit gravitational waves, gradually dissipating the system's orbital energy over millions of years. This energy loss causes the objects to move closer together, increasing their orbital velocity and emitting stronger waves. As they spiral inward, the emitted gravitational waves increase in frequency and amplitude, eventually reaching a stage where the objects rapidly coalesce (MAGGIORE, 2008).

The inspiral phase is mathematically described by the post-Newtonian (PN) approximation, an asymptotic expansion of general relativity that incorporates relativistic corrections order by order in v/c. This approximation is valid when the binary separation is large and velocities are small compared to the speed of light (MAGGIORE, 2008). Since gravitational waves are emitted due to the quadrupole moment oscillations of the system, the dominant gravitational wave frequency is related to the orbital frequency as:

$$f_{\mathrm{gw}} = 2 f_{\mathrm{orbital}}. \tag{3.39}$$

As the binary inspiral continues, the post-Newtonian expansion breaks down when the two objects enter a strong gravitational field regime. At this stage, the compact objects plunge toward each other, rapidly merging into a single black hole or neutron star (MAGGIORE, 2008). The merger phase cannot be described analytically because it involves highly non-linear and dynamical gravitational interactions.

Instead, numerical relativity simulations are required to solve Einstein's equations and model the final moments before coalescence. The merger phase typically lasts only a few milliseconds, during which the gravitational wave amplitude peaks (MAGGIORE, 2008).

Figure 3.2 - Stages of a compact binary coalescence.

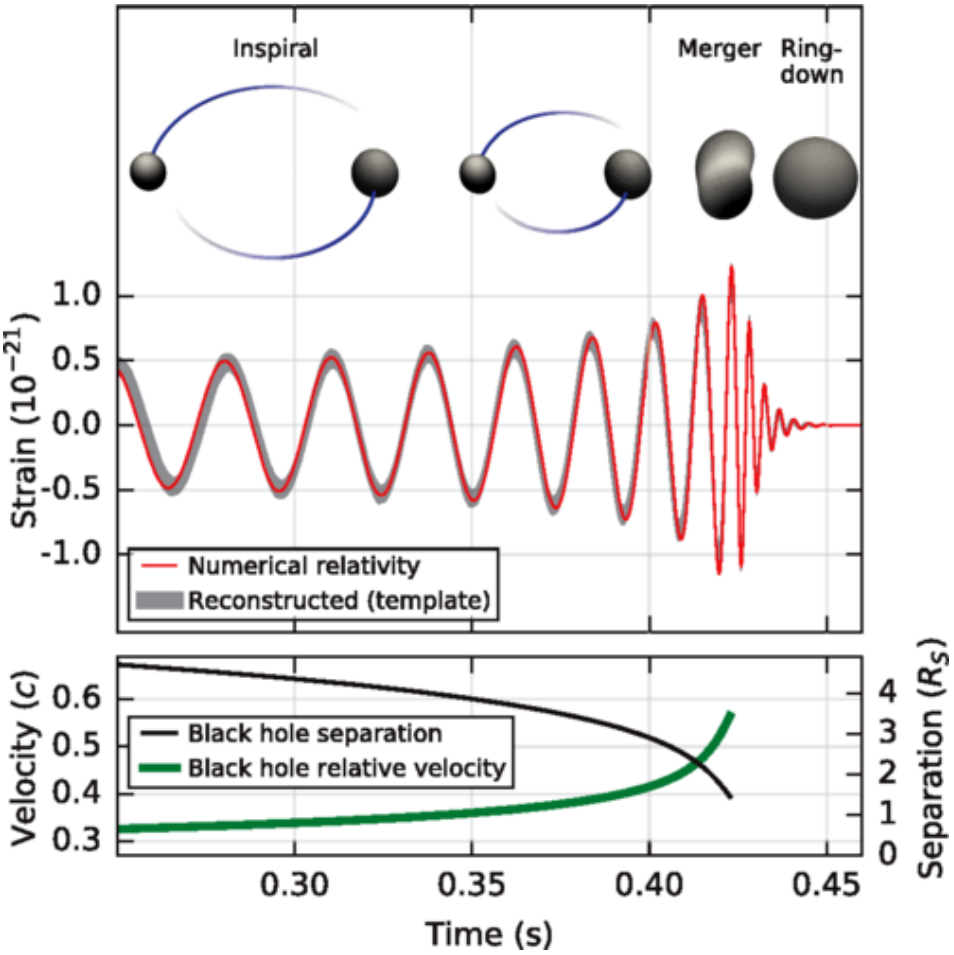

At the top, the estimated gravitational wave amplitude of GW150914 at the Hanford detector is displayed. Above that, the Schwarzschild horizons of both merging black holes are depicted, calculated numerically from the general theory of relativity. Below, the effective distance of the black holes is represented in units of Schwarzschild radii (R_s), along with the relative velocity in units of the speed of light.

SOURCE: Abbott et al. (2016).

The final remnant, if it is a black hole, undergoes quasi-normal mode (QNM) oscillations, emitting gravitational waves in the last stage known as the ringdown. These damped oscillations resemble the vibrations of a bell and carry information about the final mass and spin of the remnant black hole (MAGGIORE, 2008). The ringdown phase is well described by perturbation theory in general relativity, where the gravitational wave signal exhibits an exponentially decaying amplitude.

All gravitational waves detected by LIGO so far have originated from compact binary coalescences. LIGO's detectors are most sensitive to gravitational waves in the frequency range 10 Hz to 10 kHz (ABBOTT et al., 2019). This range corresponds to the inspiral and merger frequencies of stellar-mass black hole and neutron star binaries.

3.6 Gravitational waves in cosmology

3.6.1 Primordial Gravitational Waves

Primordial gravitational waves (PGWs), also known as relic gravitational waves, are tensor perturbations in the metric that originate from the early universe and provide a cosmological background analogous to the Cosmic Microwave Background (CMB) (WANG, 2024). These waves are predicted to be generated during the rapid exponential expansion of the universe known as inflation, which likely occurred between 10^{-36} and 10^{-32} seconds after the Big Bang. During inflation, quantum fluctuations in spacetime were stretched to macroscopic scales, producing a stochastic background of gravitational waves (WEINBERG, 2008).

As the universe expanded, the comoving wavelengths of PGWs were redshifted, placing them in the millihertz to nanohertz range today, depending on their production epoch. Unlike electromagnetic radiation, primordial gravitational waves interact weakly with matter, allowing them to traverse the cosmos largely unaltered since their production. This makes them invaluable for probing the universe's earliest moments and testing theories of inflation and quantum gravity, Figure 3.3. Detecting primordial gravitational waves remains a significant challenge. Their signals are expected to be incredibly faint, requiring advanced detectors and indirect methods, such as analyzing their imprint on the polarization of the CMB. Current and future experiments, including those using space-based observatories and pulsar timing arrays (PTAs), aim to uncover evidence of these waves. While PTAs such as NANOGrav provide constraints on nanohertz gravitational waves (AGAZIE et al., 2023), their primary sensitivity is to backgrounds from supermassive black hole binaries rather than inflationary PGWs (AGGARWAL et al., 2023). A successful detection would provide a unique window into the physics of the Big Bang and offer insights into the fundamental nature of spacetime (WANG, 2024).

Figure 3.3 - Primordial Gravitational Waves.

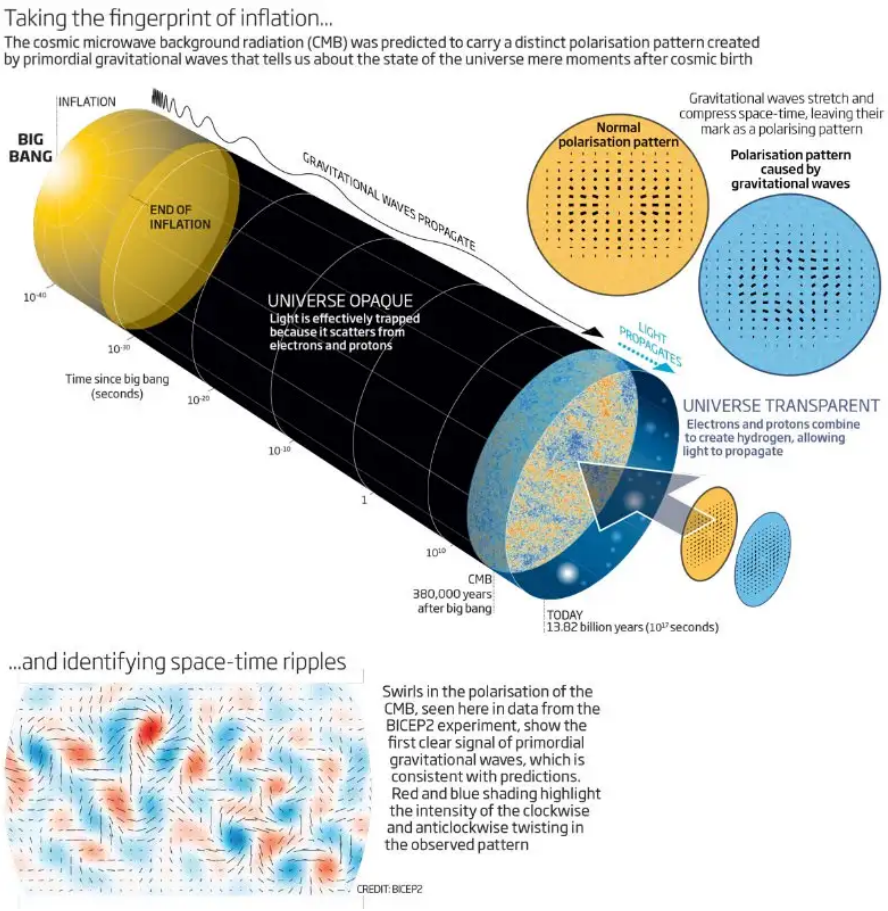

Visualization of the early universe and the imprint of primordial gravitational waves on the cosmic microwave background (CMB).

SOURCE: NEW SCIENTIST (2014).

3.6.2 Cosmological parameter estimation

Gravitational waves have become a powerful tool for investigating cosmological parameters following their first direct detections by the LIGO and Virgo detectors in 2015 (ABBOTT et al., 2016). The use of gravitational waves for estimating cosmological parameters such as the Hubble constant (H_0), matter density (Ω_m), and parameters associated with dark energy (w_0 and w_a) relies on the relationship between the gravitational wave amplitude and the luminosity distance (d_L) of the source.

Gravitational wave sources can be classified as bright sirens and dark sirens. Bright sirens refer to gravitational wave events with identifiable electromagnetic counter-

parts, such as the GW170817 event, which resulted from the coalescence of neutron stars and produced emissions across the electromagnetic spectrum, including gamma rays and visible light (ABBOTT et al., 2017a). These counterparts enable a direct association between the luminosity distance measured from gravitational waves and the redshift of the host galaxy obtained from spectroscopic observations. This combination allows for a direct estimation of the Hubble constant H_0 through the relation:

$$v = H_0 d, \tag{3.40}$$

at low redshifts ($z \ll 1$), where d represents the proper distance. Since the luminosity distance is related to the proper distance by $d_L = (1+z)d$, care must be taken when using this relation in cosmological analyses.

The GW170817 event exemplifies the potential of bright sirens in cosmology. Detected by the Advanced LIGO and Virgo detectors on August 17, 2017, GW170817 marked the first observed binary neutron star merger. Its multi-messenger nature, combining gravitational wave and electromagnetic signals, enabled the identification of the host galaxy, NGC 4993, located at a distance of approximately 40 Mpc. The redshift of the galaxy was measured to be $z = 0.009783$. Using the gravitational wave strain amplitude to determine the luminosity distance, Abbott et al. (2017) derived a value of $H_0 = 70.0^{+18.8}_{-8.8}$ km/s/Mpc, assuming a flat prior for $\cos\iota$, where ι represents the inclination angle. This result demonstrated the feasibility of using bright sirens for direct H_0 estimation, independent of traditional distance ladder methods.

On the other hand, dark sirens are gravitational wave events without observed electromagnetic counterparts. The absence of a clear identification of the host galaxy requires the use of statistical techniques to estimate cosmological parameters. These techniques rely on galaxy catalogs and redshift distributions to infer the probability of the source belonging to a given galaxy. The likelihood for H_0 in this case is expressed as:

$$\mathcal{L}(H_0) \propto \prod_i \int P(d_L^i|z, H_0) P(z) dz, \tag{3.41}$$

where $P(d_L^i|z, H_0)$ is the probability of d_L given z and H_0, and $P(z)$ represents the redshift distribution of galaxies. Analyses of dark sirens, such as GW170814, have derived H_0 values by combining gravitational wave data with galaxy catalogs. (PALMESE et al., 2020) demonstrated that a combination of dark sirens with large galaxy surveys, such as the Dark Energy Survey (DES), can yield competitive constraints on H_0. Although less precise than bright sirens for individual events, dark

sirens can significantly contribute to cosmological studies when aggregated across numerous detections. The next generation of detectors, such as the Einstein Tele-

Figure 3.4 - Comparison of H_0 estimates using GW events.

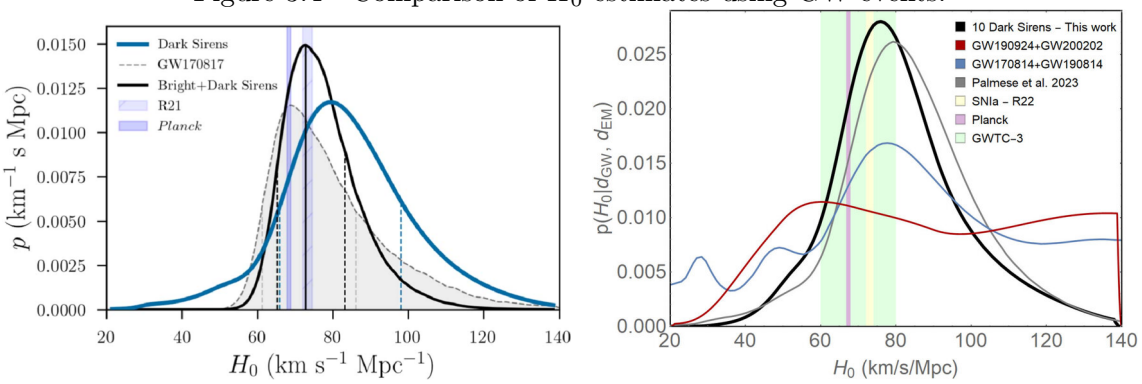

The left panel shows posterior distributions of the Hubble constant (H_0) inferred from different gravitational wave (GW) analyses. The dark blue curve represents the constraint from dark sirens, while the dashed black line corresponds to the measurement from GW170817, the first binary neutron star merger with an electromagnetic counterpart. The black solid curve combines constraints from both bright and dark sirens. The vertical bands indicate external measurements: R21 (gray) and Planck (blue).The right panel displays probability distributions for H_0 conditioned on gravitational wave and electromagnetic data from different sources. The black line represents the current work using 10 dark sirens, while the red and blue curves correspond to constraints from specific GW events (GW190924-GW200202 and GW170814-GW190814, respectively). Other external measurements, such as Palmese et al. (2023), SNIa (R22), Planck, and GWTC-3, are also shown for comparison. Both plots highlight the potential of gravitational wave cosmology in measuring the Hubble constant, with results that can be compared to traditional cosmic probes.

SOURCE: Alfradique et al. (2024) & Palmese et al. (2020).

scope (ET) and the Cosmic Explorer (CE), will expand the range of gravitational wave observations, enabling the detection of events at high redshifts ($z > 2$) and improving the precision in determining cosmological parameters (MAGGIORE et al., 2020). The Einstein Telescope is expected to detect events beyond $z \sim 5$, while Cosmic Explorer will provide complementary constraints at lower redshifts (CHEN et al., 2018). These advances will allow bright sirens to play an even more central role in observational cosmology, particularly in studies related to dark energy and the accelerated expansion of the universe.

The use of gravitational waves in cosmology is just beginning, but it has already

demonstrated its potential. With next-generation detectors, these measurements are expected to further contribute to our understanding of the universe's dynamics.

4 DATA ANALYSIS TECHNIQUES IN GRAVITATIONAL WAVES COSMOLOGY

Gravitational wave astronomy relies on sophisticated data analysis techniques to extract meaningful signals from noisy detector data. In this section, we examine the data analysis techniques employed in gravitational wave cosmology, with a specific emphasis on their relevance for estimating cosmological parameters through the use of bright sirens. We will discuss the functionality of gravitational wave interferometers, focusing on antenna pattern functions and detector response, which are integral to the accurate detection and interpretation of these signals. Additionally, we delve into Bayesian inference for parameter estimation, highlighting its ability to combine observational data with prior knowledge. The chapter concludes with a discussion of approximation methods for likelihood analysis, including the Fisher Matrix, the covariance matrix, and the DALI method, which provide efficient approaches for quantifying uncertainties and understanding parameter correlations in gravitational wave observations.

4.1 Gravitational waves interferometers

Gravitational waves affect matter by compressing objects along one axis while stretching them along the perpendicular axis. This characteristic has led to the development of gravitational wave detectors shaped like an "L". These detectors employ interferometry to measure the relative lengths of their arms precisely. Interferometry relies on analyzing the interference patterns created by combining two light sources, see Figure 4.1.

Figure 4.1 - Simplified scheme of a Michelson Interferometer.

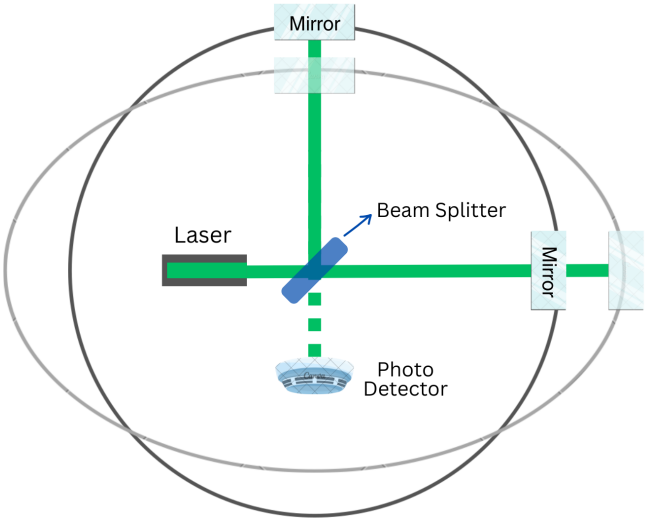

It works by splitting a laser beam evenly using a beam splitter and sending the light into two arms of the interferometer. The light is reflected off the end mirrors and converges back at the beam splitter. A photodetector detects the interference pattern. If a gravitational wave is present, one arm of the interferometer lengthens while the other shortens.

SOURCE: Adapted from Koke (2022).

A GW observatory comprises a large-scale Michelson interferometer calibrated to induce destructive interference (resulting in a dark fringe) of the laser light initially split by a beam splitter onto the suspended mirrors (test masses) and later recombined on a photodetector. The passage of a gravitational wave alters the interference pattern upon interaction with the mirrors, inducing differential accelerations along the interferometer arms. Consequently, the measurement directly involves monitoring the separation between the mirrors. Laser interferometers exhibit sensitivity across a broad frequency spectrum unlike resonant mass detectors. Currently, we have the so-called second generation of ground-based detectors for gravitational wave interference.

The LIGO observatories, short for Laser Interferometer of Gravitational Waves Observatory, are a pair of advanced detectors located in Hanford, Washington, US, and Livingston, Louisiana, US, each featuring two equal arms that are perpendicular to each other and extend up to 4km in an L-shaped configuration. The differential displacement between these arms is a direct measure of the gravitational wave strain amplitude (THORNE, 1995) and can be expressed as a dimensionless quantity of

strain h:

$$h = \frac{\Delta L}{L} \tag{4.1}$$

where $\delta L_x - \delta L_y = \Delta L$ and $L = L_x = L_y$. Alongside other sensors within the LVK (LIGO-Virgo-KAGRA) collaboration, it undergoes cycles of observation and enhancement. These cycles involve alternating between data-gathering phases, known as runs, and periods dedicated to technical enhancements aimed at boosting detector sensitivity. Following each enhancement phase, a commissioning period ensues, aiming to optimize detector performance with the upgraded components. This ensures that subsequent observation periods commence with markedly improved sensitivity compared to previous operations. Up to this point, there have been three complete observational runs with LIGO, currently, it is happening in the second part of the fourth run (O4b). At the end of the second observing run, in August 2017, Virgo joined the LIGO detector. Located in Cascina, Italy, Virgo is another interferometer that shares the same description as LIGO, however, it has 3-kilometer-long arms. In 2020, KAGRA, a fourth interferometer started operating, it is located in the depths below the Kamioka mine, located in Kamioka-cho, Hida-city, Gifu-prefecture, Japan.

The next LIGO upgrade, along with the addition of the planned LIGO India facility, is expected to enhance detection capabilities (UNNIKRISHNAN, 2013). Beyond these advancements, the third-generation ground-based detectors, Cosmic Explorer (CE) and Einstein Telescope (ET), represent the next major leap in gravitational wave observatories. The CE is designed as an L-shaped interferometer, similar to LIGO and Virgo, but on a much larger scale. The length of its arms is still under discussion, with proposed options of 20 km or 40 km each (COSMIC EXPLORER PROJECT, 2024). Its exact site is not decided yet, but it is known that it will be built in American territory. According to COSMIC EXPLORER PROJECT (2024), the expectation is that Cosmic Explorer will be able to determine the nature of the densest matter in the universe; reveal the universe's binary black hole and neutron star populations throughout cosmic time; provide an independent probe of the history of the expanding universe; explore warped spacetime with unprecedented fidelity; and expand our knowledge of how massive stars live, die, and create the matter we see today (HALL et al., 2022).

The Einsteins Telescope is a proposed underground infrastructure in a triangle shape with arms of 10km with 60° between them (EINSTEIN. . . , 2024). Each corner of the triangle has a pair of interferometers, one for low frequencies and the other for high frequencies. Therefore, the detector would be sensitive to gravitational waves coming from any direction in the sky, unlike single and traditional L-shaped interferometers

(EINSTEIN. . . , 2024). Figure 4.2, shows the ET design and a graphic comparing the size of CE, ET, and LIGO.

Figure 4.2 - Third Generation Detector.

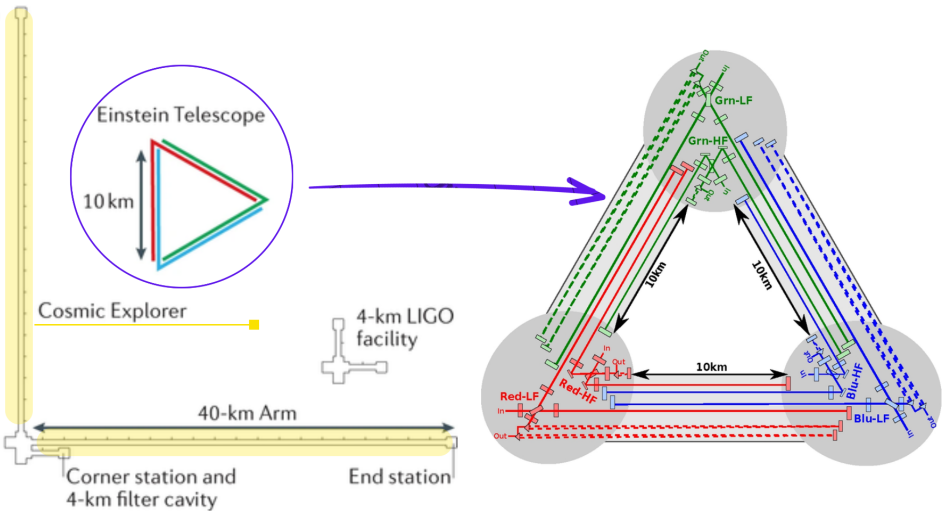

Comparison of next-generation gravitational wave detectors, focusing on the Cosmic Explorer and the Einstein Telescope. The Cosmic Explorer, featuring 40-kilometer-long arms, is designed as a linear interferometer, similar in concept to current LIGO facilities but with significantly extended arms to achieve greater sensitivity. In contrast, the Einstein Telescope is envisioned as an underground triangular interferometer, with each side measuring 10 kilometers. This design provides superior noise isolation and incorporates a unique three-detector configuration. The arms of the Einstein Telescope are color-coded to represent the pairs of interferometers located at each corner. These pairs consist of two interferometers optimized for distinct frequency bands, enabling enhanced detection of gravitational waves across a broad range of frequencies.

SOURCE: Lück et al. (2020).

4.1.1 Antenna pattern functions

The output of a gravitational wave detector is the sum of its instrumental noise $n(t)$ and the detector strain $h(t)$,

$$O(t) = h(t) + n(t), \tag{4.2}$$

The detector strain is defined as the scalar product of the perturbation tensor h and the detector tensor D, which encodes the detector's geometric properties (WHELAN, 2013):

$$h(t) = D : h = D : \left[\sum_{A=+,\times} h_A(t) \mathbf{e}_A \right] \tag{4.3}$$

$$= \sum_{A=+,\times} \left[D^{ij} e_{ij}^{(A)} \right] h_A(t) = \left[D^{ij} e_{ij}^{(+)} \right] h_+ + \left[D^{ij} e_{ij}^{(\times)} \right] h_\times \tag{4.4}$$

$$= F_+ h_+(t) + F_\times h_\times(t) \tag{4.5}$$

Where e_A represents the polarization tensor basis of h (HILBORN, 2018). The coefficients F_+ and $F_\times$ are known as Antenna Pattern Functions; these depend on the detector's geometry, the source's sky position, and the polarization angle. The detector tensor D can be expressed as (WHELAN, 2013):

$$D = \frac{\sin \Omega}{2} \begin{bmatrix} 1 & 0 & 0 \\ 0 & -1 & 0 \\ 0 & 0 & 0 \end{bmatrix}, \tag{4.6}$$

where Ω is the angle between the arms of the interferometer.

In gravitational wave astronomy, the polarization tensors e_+ and $e_\times$ describe the two independent polarization states of a gravitational wave. These tensors are typically expressed in the source frame but must be transformed into the detector frame to calculate the detector's response (HILBORN, 2018). In the source frame, the polarization tensors are defined as:

$$e_+ = (\hat{x}_S \otimes \hat{x}_S - \hat{y}_S \otimes \hat{y}_S) = \begin{bmatrix} 1 & 0 & 0 \\ 0 & -1 & 0 \\ 0 & 0 & 0 \end{bmatrix}, \tag{4.7}$$

$$e_\times = (\hat{x}_S \otimes \hat{y}_S + \hat{y}_S \otimes \hat{x}_S) = \begin{bmatrix} 0 & 1 & 0 \\ 1 & 0 & 0 \\ 0 & 0 & 0 \end{bmatrix}. \tag{4.8}$$

To transform the basis from the *source frame* (S) to the *detector frame* (D), we define the rotation matrix $\mathbf{R}$ as a product of three simpler rotations, each associated with

one of the angles α_d, β_d, or ψ_d:

$$\mathbf{R} = \underbrace{\begin{bmatrix} \cos\psi_d & \sin\psi_d & 0 \\ -\sin\psi_d & \cos\psi_d & 0 \\ 0 & 0 & 1 \end{bmatrix}}_{\text{rotation by } \psi_d} \underbrace{\begin{bmatrix} \cos\beta_d & 0 & -\sin\beta_d \\ 0 & 1 & 0 \\ \sin\beta_d & 0 & \cos\beta_d \end{bmatrix}}_{\text{rotation by } \beta_d} \underbrace{\begin{bmatrix} \cos\alpha_d & \sin\alpha_d & 0 \\ -\sin\alpha_d & \cos\alpha_d & 0 \\ 0 & 0 & 1 \end{bmatrix}}_{\text{rotation by } \alpha_d}. \tag{4.9}$$

Here, the subscript (d) indicates angles measured in the detector frame, α_d, azimuthal angle in the detector plane; β_d, polar angle from the detector's z-axis; ψ_d polarization angle, describing the rotation of the wave's polarization axes.

Given a polarization tensor $\mathbf{e}_{(A,S)}$ in the source frame (A can be $+$ or $\times$), its components in the detector frame are obtained via:

$$\mathbf{e}_{(A,D)} = \mathbf{R}^{\mathsf{T}}\, \mathbf{e}_{(A,S)}\, \mathbf{R}. \tag{4.10}$$

By carrying out the matrix multiplication explicitly, one finds, for the $(+)$ polarization in the detector frame:

$$\mathbf{e}_{(+,D)} = \begin{bmatrix} r_{11}^2 - r_{21}^2 & r_{11}r_{12} - r_{21}r_{22} & r_{11}r_{13} - r_{21}r_{23} \\ r_{12}r_{11} - r_{22}r_{21} & r_{12}^2 - r_{22}^2 & r_{12}r_{13} - r_{22}r_{23} \\ r_{13}r_{11} - r_{23}r_{21} & r_{13}r_{12} - r_{23}r_{22} & r_{13}^2 - r_{23}^2 \end{bmatrix}, \tag{4.11}$$

and for the $(\times)$ polarization:

$$\mathbf{e}_{(\times,D)} = \begin{bmatrix} 2r_{21}r_{11} & r_{21}r_{12} + r_{11}r_{22} & r_{21}r_{13} + r_{11}r_{23} \\ r_{22}r_{11} + r_{12}r_{21} & 2r_{22}r_{12} & r_{22}r_{13} + r_{12}r_{23} \\ r_{23}r_{11} + r_{13}r_{21} & r_{23}r_{12} + r_{13}r_{22} & 2r_{23}r_{13} \end{bmatrix}. \tag{4.12}$$

In these expressions, r_{ij} are the elements of the simplified rotation matrix

$$\mathcal{R} = \begin{bmatrix} r_{11} & r_{12} & r_{13} \\ r_{21} & r_{22} & r_{23} \\ r_{31} & r_{32} & r_{33} \end{bmatrix},$$

which corresponds to $\mathbf{R}$ in the Equation 4.10. From the expressions (4.10), (4.11) and the detector tensor D, we can calculate the Antenna Pattern Functions (WHE-

LAN, 2013):

$$F_+ = D^{ij}e^+_{ij} = \frac{1}{2}\sin^2\Omega\left[(r_{11}^2 - r_{21}^2) - (r_{12}^2 - r_{22}^2)\right], \tag{4.13}$$

$$F_\times = D^{ij}e^\times_{ij} = \sin 2\Omega[r_{21}r_{11} - r_{22}r_{12}]. \tag{4.14}$$

Assuming $\psi = 0$, the simplified rotation matrix is (WHELAN, 2013):

$$R_{\alpha\beta} = \begin{bmatrix} \cos\beta_d\cos\alpha_d & \cos\beta_d\sin\alpha_d & -\sin\beta_d \\ -\sin\alpha_d & \cos\alpha_d & 0 \\ \sin\beta_d\cos\alpha_d & \sin\beta_d\sin\alpha_d & \cos\beta_d \end{bmatrix}. \tag{4.15}$$

Using this, we derive the explicit expressions for the Antenna Pattern Functions, if the polarization angle $\psi = 0$ (WHELAN, 2013):

$$f_+(\alpha,\beta_\alpha) = \frac{1}{2}\sin\Omega(1+\cos^2\beta_d)\cos(2\alpha_d), \tag{4.16}$$

$$f_\times(\alpha,\beta_\alpha) = -\sin\Omega\cos\beta_d\sin(2\alpha_d). \tag{4.17}$$

Considering the polarization angle, the general Antenna Pattern Functions are given by:

$$F_+(\alpha_d,\beta_d,\psi_d) = f_+\cos(2\psi_d) + f_\times\sin(2\psi_d), \tag{4.18}$$

$$F_\times(\alpha_d,\beta_d,\psi_d) = -f_+\sin(2\psi_d) + f_\times\cos(2\psi_d), \tag{4.19}$$

$$f_+(\alpha_d,\beta_d) = \frac{1}{2}\sin\Omega\Big(1+\cos^2\beta_d\Big)\cos(2\alpha_d), \tag{4.20}$$

$$f_\times(\alpha_d,\beta_d) = -\sin\Omega\cos\beta_d\sin(2\alpha_d). \tag{4.21}$$

4.1.2 Detector response

The GW strain can be written as the linear combination of the GW polarizations:

$$h(t) = F_+h_+(t) + F_\times h_\times(t) \tag{4.22}$$

Or

$$h(t) = F\cdot[(\cos\zeta)h_+ + (\sin\zeta)h_\times] \tag{4.23}$$

where,

$$F(\alpha,\beta) = \sqrt{F_+^2 + F_\times^2} = \sqrt{f_+^2 + f_\times^2} \tag{4.24}$$

$$\tan \zeta = \frac{F_\times}{F_+} \tag{4.25}$$

The detector response is represented by the quantity F, which indicates the detector's sensitivity to the sky. All L-shaped detectors have four blind spots, where F = 0. These blind spots occur in the plane of the detector, in directions where the incoming gravitational waves deform both detector arms in the same way. The figures below show the sky plot projected on the Earth's surface of the detector response for the 2G detectors individually and combined, highlighting the necessity of using multiple detectors to eliminate areas of no sensitivity. The combined detectors do not have blind spots in the sky, meaning that this detector network is sensitive to all sky directions.

Figure 4.3 - LIGO Livingston detector response.

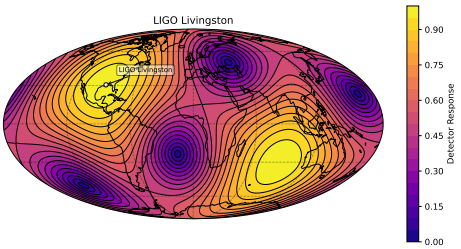

Figure 4.4 - LIGO Hanford detector response.

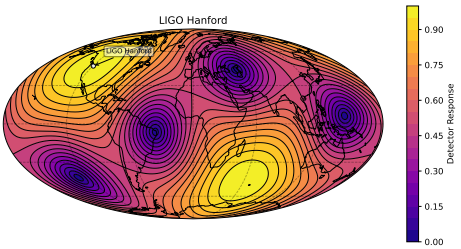

Figure 4.5 - Virgo detector response.

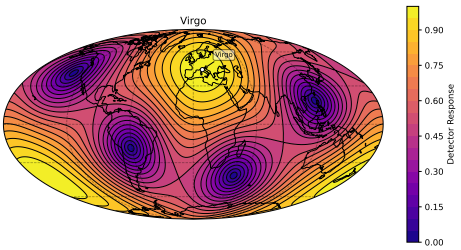

Figure 4.6 - KAGRA detector response.

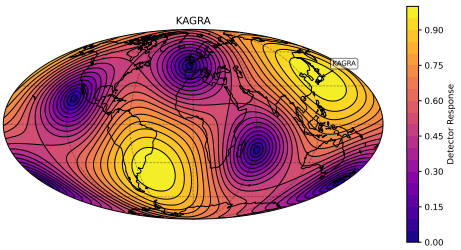

Figure 4.7 - Combined detector response.

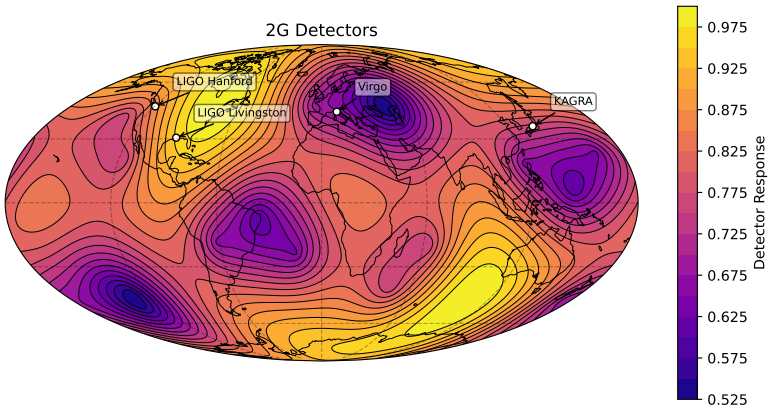

These plots illustrate the antenna response functions of different gravitational wave detectors across the sky. Each plot represents how sensitive a specific detector is to gravitational waves coming from different sky locations, using an all-sky projection with a color gradient and contour lines. The color bar indicates the relative sensitivity, with yellow regions corresponding to higher sensitivity and purple regions to lower sensitivity. The combined detector response (Figure 4.7) demonstrates how the network of gravitational wave observatories complements each other to provide better sky coverage and improved localization of astrophysical sources.

SOURCE: Auhtor.

When considering 3G detectors, CE will have a sensitivity map similar to those of LIGO, Virgo, and KAGRA, resulting in four blind spots. On the other hand, the shape of ET is still under discussion. If it takes on a triangular shape, it will not have any blind spots. This is because it can function as a combination of three separate detectors positioned in the same geographic location but with different orientations (COSMIC EXPLORER PROJECT, 2024; EINSTEIN. . . , 2024). The figures below illustrate the CE and ET detector responses.

Figure 4.8 - Cosmic Explorer detector response.

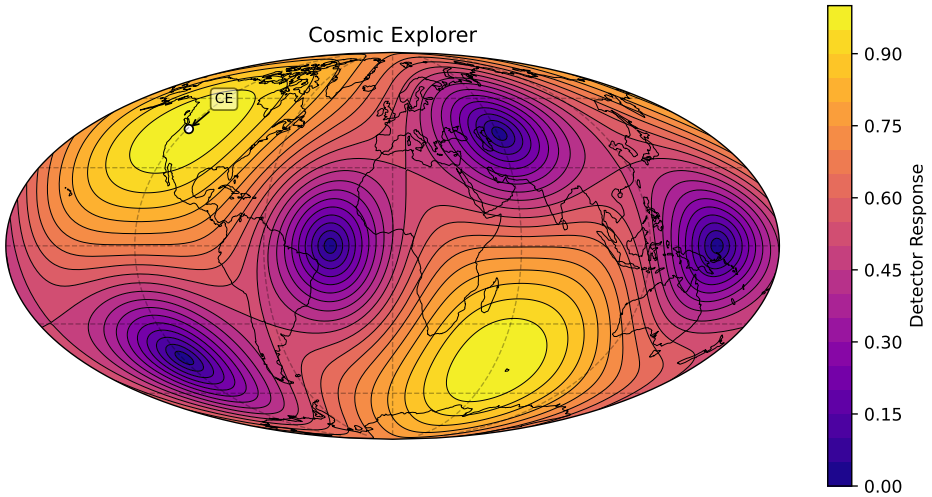

SOURCE: Author.

Figure 4.9 - Einstein Telescope detector response.

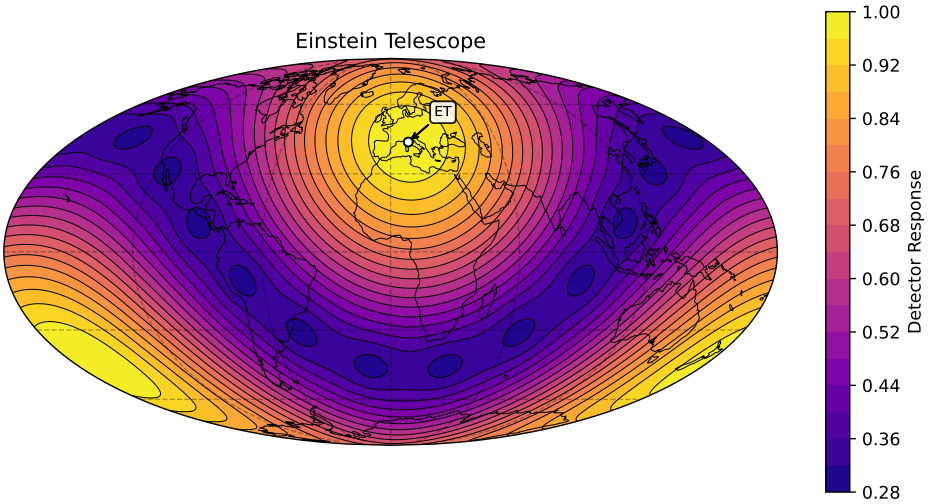

SOURCE: Auhtor.

4.1.3 Source sky position and arrival time delay

Now that we understand how the GW observatories operate, it is important to know how to use them to get some information about the source. When observing the arrival of a wavefront, the time delays among observatories can be used to determine the celestial coordinates of the gravitational wave source. When a gravitational wave passes through Earth, it arrives at geographically separated detectors at different times. These time delays depend on the distance between detectors and the direction from which the wave is coming (HILBORN, 2018).

Let consider the 2G detectors. Thus, we define the position of the Hanford Observatory relative to the Livingston Observatory as $\vec{r}_{LH}$ (see Figure 4.10(a)). Similarly, the position of the Virgo Observatory is denoted as $\vec{r}_{LV}$. These position vectors can be calculated using the following formulas:

$$\vec{r}_{LH} = (\hat{H} - \hat{L})R_E, \tag{4.26}$$

$$\vec{r}_{LV} = (\hat{V} - \hat{L})R_E, \tag{4.27}$$

where R_E is the radius of the Earth (approximately 6.37×10^3 km) (HILBORN, 2018). These vectors represent the spatial separations between the detectors and are expressed in an Earth-fixed coordinate system.

The unit vector $\hat{w}_z(\alpha_d, \beta_d)$ points in the direction of the incoming gravitational wave. It can be defined in terms of spherical coordinates using the angles α (latitude) and β (longitude). In spherical coordinates, the unit vector can be decomposed along the axes $\hat{x}_E$, $\hat{y}_E$, and $\hat{z}_E$ as a combination of these directions, weighted by the angles α and β. In Cartesian coordinates, the vector $\vec{w}_z$ in terms of α_d and β_d is expressed as:

$$\vec{w}_z = \sin(\alpha_d)\cos(\beta_d)\hat{x}_E + \sin(\alpha_d)\sin(\beta_d)\hat{y}_E + \cos(\alpha_d)\hat{z}_E. \tag{4.28}$$

However, for the propagation vector of the gravitational wave, we want the vector to point in the opposite direction. Thus, we obtain the expression for $-\vec{w}_z$:

$$-\vec{w}_z = -\sin(\alpha_d)\cos(\beta_d)\hat{x}_E - \sin(\alpha_d)\sin(\beta_d)\hat{y}_E - \cos(\alpha_d)\hat{z}_E. \tag{4.29}$$

Rearranging the terms and considering the signs, we obtain the GW propagation unit vector:

$$\vec{w}_z(\alpha, \beta) = -\cos(\alpha_d)\cos(\beta_d)\hat{x}_E + \cos(\alpha_d)\sin(\beta_d)\hat{y}_E - \sin(\alpha)\hat{z}_E. \tag{4.30}$$

The time delay between two detectors, such as Livingston and Hanford, can be calculated using the dot product:

$$\Delta t_{LH} = \frac{\hat{w}_z(\alpha_d, \beta_d) \cdot \vec{r}_{LH}}{c}, \tag{4.31}$$

Here c is the speed of light. Similarly, the time delay between Livingston and Virgo is given by:

$$\Delta t_{LV} = \frac{\hat{w}_z(\alpha_d, \beta_d) \cdot \vec{r}_{LV}}{c}. \tag{4.32}$$

The dot product $\hat{w}_z \cdot \vec{r}_{LH}$ calculates the projection of the position vector $\vec{r}_{LH}$ in the direction of the incoming wave, representing how much of this vector aligns with the GW direction. Dividing by c converts this projection from a distance to a time delay (HILBORN, 2018; WHELAN, 2013).

Figure 4.10 - Geometric representation of the time-delay analysis in a two-detector gravitational-wave network.

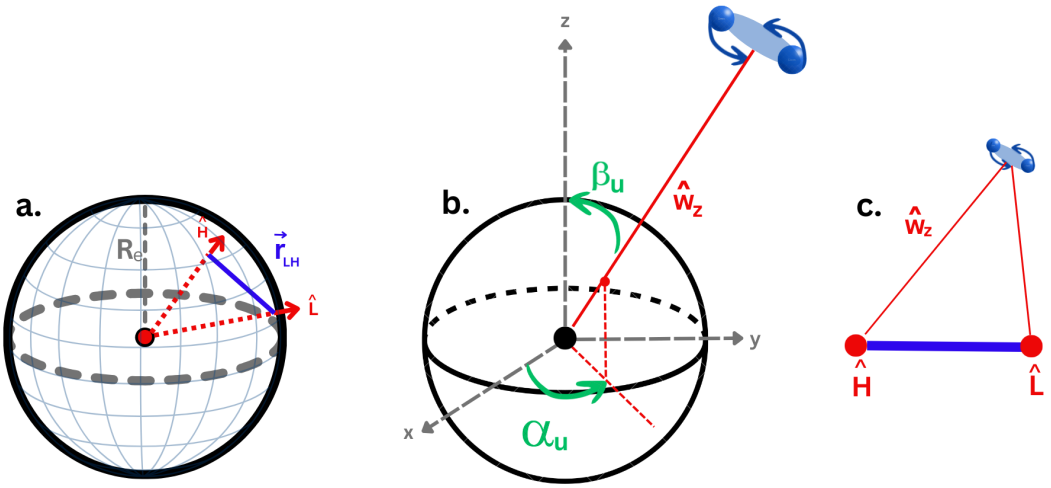

(a) The relative positioning of the detectors on Earth's surface, with $\hat{H}$ and $\hat{L}$ denoting unit vectors pointing to the respective detector locations. $\vec{r}_{LH}$ is the baseline vector between the two detectors, and R_e is Earth's radius. **(b)** Orientation of the gravitational wave propagation direction $\hat{w}_z$ in a spherical coordinate system, defined by the azimuthal angle α_u and the polar angle β_u. **(c)** The triangle formed by the wave propagation vector $\hat{w}_z$, detector positions $\hat{H}$ and $\hat{L}$.

SOURCE: Author.

When dealing with multiple detectors, we must know how to relate the observed sky position of the GW source among different detectors. Because of that, we will choose the geocentric coordinates as the common reference. The GW unity vector aligned with the line of sight between the detector and source is described by the Equation 4.30

$$\vec{w}_z = \sin(\alpha_u)\cos(\beta_u)\hat{x}_E + \sin(\alpha_u)\sin(\beta_u)\hat{y}_E + \cos(\alpha_u)\hat{z}_E.$$

where $u = d$ denotes the detector frame and $u = g$ denotes the geocentric frame. The rotation matrix $\mathbf{R}$ which transforms from detector frame to geocentric frame is given by:

$$\mathbf{R} = \begin{pmatrix} \cos\xi_u & \sin\xi_u & 0 \\ -\sin\xi_u & \cos\xi_u & 0 \\ 0 & 0 & 1 \end{pmatrix} \begin{pmatrix} \cos\theta_u & 0 & -\sin\theta_u \\ 0 & 1 & 0 \\ \sin\theta_u & 0 & \cos\theta_u \end{pmatrix} \begin{pmatrix} \cos\phi_u & \sin\phi_u & 0 \\ -\sin\phi_u & \cos\phi_u & 0 \\ 0 & 0 & 1 \end{pmatrix}, \quad (4.33)$$

In which θ_u and ϕ_u are the detector coordinates, latitude, and longitude, and ξ_u is the angular orientation of the detector to its normal $\hat{z}_d$. Equations 4.30 and 4.33, lead to the sky position transformation (SOUZA, 2023):

$$\alpha_a = \tan^{-1}\left(\frac{\cos\xi_a U - \sin\xi_a V}{\sin\xi_a U + \cos\xi_a V}\right), \quad (4.34)$$

$$\beta_a = \tan^{-1}\left(\frac{\sqrt{1-X^2}}{X}\right), \quad (4.35)$$

where,

$$U \equiv \sin\beta_0 \sin(\alpha_0 - \phi_a), \quad (4.36)$$

$$V \equiv \left[\sin\beta_0 \cos\theta_a \cos(\alpha_0 - \phi_a) - \cos\beta_0 \sin\theta_a\right], \quad (4.37)$$

$$X \equiv \cos\theta_a \cos\beta_0 + \sin\theta_a \sin\beta_0 \cos(\alpha_0 - \phi_a). \quad (4.38)$$

To conclude, the ability to precisely determine the sky position of a gravitational wave source is crucial for multi-messenger astronomy, particularly in the context of Bright Sirens. By combining the reconstructed sky localization from gravitational wave data with electromagnetic counterparts, we can significantly refine distance measurements.

4.2 Matched filtering

To gain deeper insights into the gravitational wave source, it is essential to analyze the signal and extract meaningful information. Matched filtering is a technique used to maximize the signal-to-noise ratio (SNR) in the search for a known waveform within noisy data (JANQUART, 2019-2020). The method involves correlating the incoming data stream with a set of precomputed theoretical waveforms, or templates, that represent the expected gravitational wave signals. These templates are meticulously calculated using General Relativity and are based on detailed models of astrophysical sources, such as binary black hole mergers or neutron star collisions, ensuring optimal sensitivity to the targeted signals (MA et al., 2024; JANQUART,

2019-2020).

Gravitational wave detectors measure tiny perturbations in spacetime caused by passing GWs. As defined before 4.2, these perturbations are characterized by a strain $h(t)$, which is typically much smaller than the noise level in the detectors. The noise, $n(t)$, arises from various sources, including thermal vibrations, seismic activity, and quantum fluctuations. The total data stream, $O(t)$, can be expressed as:

$$O(t) = h(t) + n(t),$$

where $h(t)$ represents the GW signal, and $n(t)$ is the noise. As shown in Figure 4.11, detector characterization ensures data quality before applying advanced filtering techniques.

Figure 4.11 - Schematic overview of the gravitational wave detection pipeline.

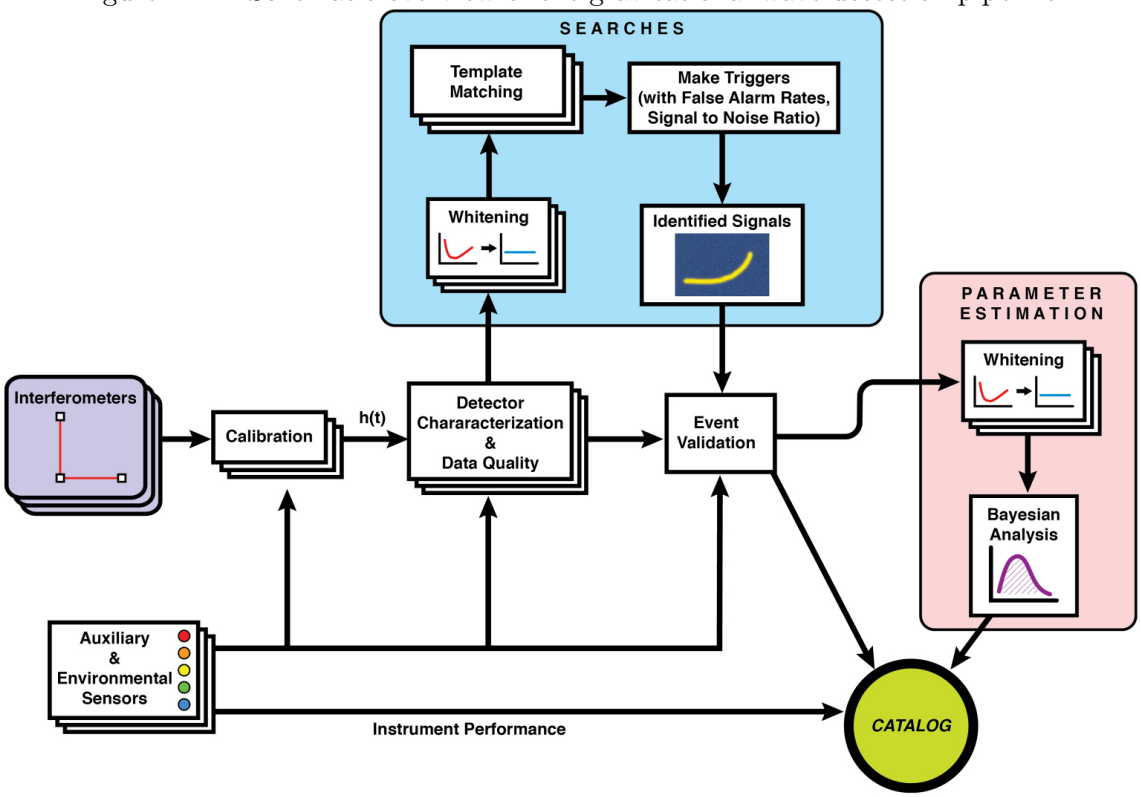

The process begins with calibrated data from interferometers subjected to detector characterization and whitening. Matched filtering is employed to identify candidate signals, which are subsequently validated and analyzed using Bayesian parameter estimation. Auxiliary sensors monitor environmental and instrumental noise to ensure data quality.

SOURCE: Abbott et al. (2020).

Detector Sensitivity. To identify the filter that closely matches the data, It is needed not only the data but also the sensitivity of the detector and a catalog of pre-computed waveforms. The sensitivity of a gravitational wave detector is characterized by its noise power spectral density (PSD), $S_n(f)$, which quantifies the frequency-dependent noise background present in the data (JANQUART, 2019-2020). The PSD is formally defined as the Fourier transform of the noise autocorrelation function $\langle n(t)n(t+\tau)\rangle$ (MA et al., 2024),(JANQUART, 2019-2020):

$$S_n(f) = 2\int_{-\infty}^{\infty} \langle n(t)n(t+\tau)\rangle e^{-i2\pi f\tau} d\tau, \tag{4.39}$$

where $n(t)$ is the noise as a function of time, τ is the time lag, f is the frequency, and $\langle\cdot\rangle$ represents the ensemble average over noise realizations.

For real-world analyses, where data are collected over a finite observation time T, the PSD is estimated using the finite-duration time series $n(t)$. In this case, $S_n(f)$ can be expressed as (MAGGIORE, 2008):

$$S_n(f) = \frac{2}{T}\left\langle |\tilde{n}(f)|^2 \right\rangle, \tag{4.40}$$

where $\tilde{n}(f)$ is the Fourier transform of the noise over the time interval T, defined as:

$$\tilde{n}(f) = \int_{-T/2}^{T/2} n(t)e^{-i2\pi ft} dt, \tag{4.41}$$

and $|\tilde{n}(f)|^2$ is the periodogram, which represents the squared magnitude of the Fourier transform. The factor $2/T$ normalizes the PSD, accounting for the finite duration of the data. In practice, the ensemble average $\langle\cdot\rangle$ is often approximated by averaging over multiple noise realizations or adjacent frequency bins. The noise power spectral density ($S_n(f)$) provides insight into the frequency-dependent sensitivity of gravitational wave detectors. Figure 4.12 illustrates the $S_n(f)$ curves for various detectors, highlighting their sensitivity across different frequency bands. This visualization is critical for understanding the regions where each detector is most effective at identifying gravitational wave signals.

Figure 4.12 - Noise power spectral density.

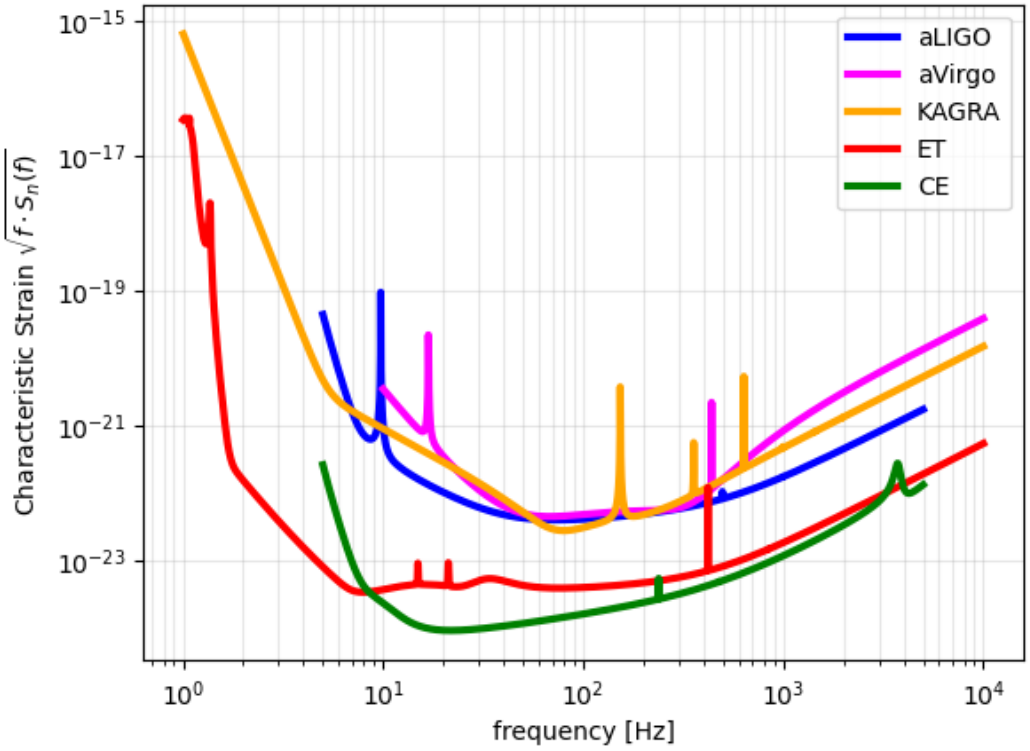

Noise power spectral density $S_n(f)$ for various gravitational wave detectors, showing the frequency-dependent sensitivity of each detector. The characteristic strain $\sqrt{f \cdot S_n(f)}$ highlights the regions of maximum sensitivity.

SOURCE: Author.

Signal to Noise Ratio. The noise power spectral density $S_n(f)$ not only characterizes the detector's sensitivity but also plays a critical role in quantifying the detectability of a signal, as it directly enters the calculation of the signal-to-noise ratio (SNR), which determines the strength of a gravitational wave signal relative to the noise background (SAULSON, 1990; MARTYNOV et al., 2016). The quantity of signal S is determined by the expected value of the output and the desired filter K(t):

$$S = \int_{-\infty}^{+\infty} \langle O(t)K(t) \rangle dt = \int_{-\infty}^{+\infty} [h(t) + n(t)]\, K(t) dt = \int_{-\infty}^{+\infty} h(t)K(t)dt, \qquad (4.42)$$

If the equation above and the quantity of noise N are modeled in terms of frequency,

the ratio between the signal S and the noise N is given by:

$$\rho \equiv \frac{S}{N} = 2\frac{\mathrm{Re}\left\{\int_0^\infty \tilde{h}(f)\tilde{K}^*(f)df\right\}}{\sqrt{\int_0^\infty S_n(f)|\tilde{K}(f)|^2 df}}, \tag{4.43}$$

So, to find the filter that maximizes ρ there is a new quantity $\vee$ related to the filter as $\tilde{\vee}(f) \equiv \tilde{K}(f)S_n(f)$. The new equation is

$$\rho = 2\frac{\mathrm{Re}\left\{\int_0^\infty \frac{\tilde{h}(f)\tilde{v}^*(f)}{S_n(f)}df\right\}}{\sqrt{\int_0^\infty \frac{|\tilde{v}(f)|^2}{S_n(f)}df}}. \tag{4.44}$$

The optimal filter that maximizes the signal-to-noise ratio is $\tilde{\vee}(f) = \tilde{h}(f)$, where $\tilde{h}(f)$ represents the Fourier transform of the gravitational wave signal (MAGGIORE, 2008)

$$\rho_{\mathrm{opt}} = \sqrt{4\int_0^\infty \frac{|\tilde{h}(f)|^2}{S_n(f)}df}. \tag{4.45}$$

In practice, we only have one instance of noise instead of several. Because of this, we cannot average the output $O(t)$ over multiple noise instances. Instead, we calculate the signal-to-noise ratio from Equation (4.44). We replace $\tilde{h}(f)$ with $\tilde{\mathcal{O}}(f)$ and $\tilde{v}(f)$ with $\tilde{h}_f e^{2\pi i f t_c}$.

$$\rho(t_c) = 2\frac{\mathrm{Re}\left\{\int_0^\infty \frac{\tilde{\mathcal{O}}(f)\tilde{h}_f^*(f)e^{-2\pi i f t_c}}{S_n(f)}df\right\}}{\sqrt{\int_0^\infty \frac{|\tilde{h}_f(f)|^2}{S_n(f)}df}}. \tag{4.46}$$

In gravitational wave detection, an SNR threshold of 8 is commonly used as a criterion to ensure the reliability of detected signals. This threshold corresponds to a false alarm probability on the order of 10^{-4} to 10^{-5}, which significantly reduces the chances of identifying noise as a gravitational wave event.

The choice of SNR > 8 is informed by the weak nature of gravitational wave signals and the various types of noise present in interferometers (LIGO/VIRGO/KAGRA COLLABORATION, 2024). Thermal noise, arising from vibrational excitation in materials, seismic noise due to ground vibrations, and quantum noise associated with the light's quantum properties all contribute to the background noise (MARTYNOV et al., 2016). These noise sources create a challenging environment for signal detection, making it crucial to set a robust threshold for identifying real events.

4.3 Bayesian inference

After matched filtering confirms the presence of the gravitational wave (GW) signal in the detector output, the next step is to estimate the astrophysical parameters of the GW source using Bayesian statistics (MAGGIORE, 2008). Bayesian inference is a statistical approach based on Bayes' theorem, providing a mathematical framework to update the probability of a hypothesis in light of new evidence. This methodology has been applied in various fields, such as physics, biology, social sciences, and engineering, due to its ability to integrate prior knowledge with observational data coherently and flexibly. Bayes' theorem can be mathematically expressed as:

$$P(\theta_i \mid d) = \frac{P(d \mid \theta_i)P(\theta_i)}{P(d)}, \tag{4.47}$$

Where:

- $P(\theta_i \mid d)$: the posterior distribution, the probability of the hypothesis given the data ;
- $P(d \mid \theta_i)$: the likelihood, represents the probability of observing the data given a specific set of parameters.
- $P(\theta_i)$: the prior distribution, reflecting prior knowledge about the parameters of a statistical model, encapsulates our initial beliefs or assumptions before observing any data;
- $P(d)$: the evidence or normalization factor, ensuring that the sum of posterior probabilities equals 1. It is calculated as:

$$P(d) = \int P(d \mid \theta_i)P(\theta_i)\mathrm{d}\theta. \tag{4.48}$$

Prior distributions represent the initial state of knowledge about the parameter θ_i before observing the data. They can be informative, incorporating relevant prior knowledge, or non-informative, aiming to minimize subjective influences (GELMAN et al., 2013). The likelihood is derived from a probabilistic model describing how the data are generated. Choosing an appropriate model is crucial to ensure valid inferences. The posterior distribution combines the prior with the observed data through the likelihood, representing the updated state of knowledge.

The inference process involves several steps. First, the problem must be defined by identifying the parameter to be inferred and collecting the data. Then, a prior

distribution is chosen to represent prior knowledge about. Afterward, a likelihood function is constructed to model the probability of the data given the parameter. Applying Bayes' theorem updates the distribution, resulting in the posterior. Finally, analyses such as point estimation, interval estimation, or hypothesis testing are performed.

4.4 Approximation methods for likelihood analysis

Bayesian inference provides a rigorous framework for parameter estimation, combining observational data and prior information using Bayes' theorem. However, the direct application of this formalism can be computationally challenging, especially for models with high-dimensional parametric spaces. To deal with these difficulties, approximate likelihood analysis methods play a crucial role.

4.4.1 The Fisher matrix method

The Fisher matrix method is used to quantify the amount of information a dataset provides about a set of parameters (WITTMAN, 2016). It can also be described as a statistical tool that leverages observational information to evaluate uncertainties in parameter estimation. Crucially, it is useful not only when data are already in hand but also for forecasting precision limits in future experiments (TEGMARK, 1997; WITTMAN, 2016).

In many practical scenarios, the observed data d_i are assumed to be drawn from independent Gaussian distributions whose means are given by a theoretical model $M(\theta_i)$ and whose variances are σ_i^2. In this case, the likelihood function for N data points can be written as:

$$\mathcal{L}(\theta) = \prod_{i=1}^{N} \frac{1}{\sqrt{2\pi}\,\sigma_i} \exp\left[-\frac{1}{2}\frac{(d_i - M_(\theta)_i))^2}{\sigma_i^2}\right]. \tag{4.49}$$

Taking the natural logarithm of $\mathcal{L}(\theta)$ yields:

$$\ln \mathcal{L}(\theta) = -\frac{1}{2}\sum_{i=1}^{N}\left[\frac{(d_i - M_(\theta_i))^2}{\sigma_i^2} + \ln\left(2\pi\,\sigma_i^2\right)\right]. \tag{4.50}$$

Thus, we apply an expansion of the logarithm of the likelihood up to the second order in the parameter displacement ($\Delta\theta_i = \theta_i - \hat{\theta}_i$).

$$\log \mathcal{L}(\theta_i) = \log \mathcal{L}|_{\hat{\theta}_i} + \sum_i \frac{\partial \log \mathcal{L}}{\partial \theta_i}\Big|_{\hat{\theta}_i} \Delta\theta_i + \frac{1}{2}\frac{\partial^2 \log \mathcal{L}}{\partial\theta_i \partial\theta_j}\Big|_{\hat{\theta}_i} \Delta\theta_i \Delta\theta_j + \mathcal{O}(3) \tag{4.51}$$

where $\mathcal{L}(\theta)$ is the likelihood function associated with the dataset, θ is the vector of model parameters. As stated in (COE, 2009), the initial term (green) remains constant and is incorporated into the normalization. The subsequent term (red) assesses the first derivative of the likelihood at its peak value (which is 0 by definition). The final term (blue) represents the quadratic term, where its coefficients characterize the Fisher Matrix F_{ij}. It can be written as:

$$F_{ij} = -\left\langle \frac{\partial^2 \ln \mathcal{L}(\theta)}{\partial\theta_i \partial\theta_j} \right\rangle, \tag{4.52}$$

where

- F_{ij} is an element of the Fisher matrix,
- $\langle\cdot\rangle$ denotes the expected value (averaging over possible data realizations).

A key outcome of the Fisher matrix is its relationship to the Cramér-Rao bound ($\mathrm{Var}(\theta_i) \geq \left(\mathbf{F}^{-1}\right)_{ii}$), it defines that the diagonal elements of F_{-1} gives a lower bound of the variance of the estimated parameters (TEGMARK, 1997).

4.4.2 Covariance matrix

The covariance matrix describes the uncertainty associated with estimating the model parameters (COE, 2009). It can be defined through the inverse of the Fisher matrix:

$$\mathbf{C} = \mathbf{F}^{-1}, \tag{4.53}$$

where $\mathbf{C}$ is the covariance matrix and $\mathbf{F}$ is the Fisher matrix. Each element C_{ij} of the covariance matrix represents the variance or covariance between the parameters θ_i and θ_j.

4.4.3 DALI method

The Derivative Approximation for Likelihood (DALI) method was developed to overcome the limitations of the Fisher information matrix in analyzing non-Gaussian probability distributions. The Fisher matrix assumes that the likelihood function is approximately Gaussian around its maximum, an assumption that does not always hold in cosmological and gravitational wave applications (SELLENTIN et al., 2014). DALI extends this approach by incorporating higher-order derivatives, allowing it to capture the non-Gaussianities inherent in the parameter space, thus improving

parameter estimation. For that, we use the Taylor expansion of the likelihood logarithm.

$$\log \mathcal{L}(\theta_i) = \log \mathcal{L}|_{\hat{\theta}_i} + \sum_i \frac{\partial \log \mathcal{L}}{\partial \theta_i}\Big|_{\hat{\theta}_i} \Delta\theta_i + \frac{1}{2!}\frac{\partial^2 \log \mathcal{L}}{\partial \theta_i \partial \theta_j}\Big|_{\hat{\theta}_i} \Delta\theta_i \Delta\theta_j + \frac{1}{3!}\frac{\partial^3 \log \mathcal{L}}{\partial \theta_i \partial \theta_j \partial \theta_k}\Big|_{\hat{\theta}_i} \Delta\theta_i \Delta\theta_j \Delta\theta_k + \frac{1}{4!}\frac{\partial^4 \log \mathcal{L}}{\partial \theta_i \partial \theta_j \partial \theta_k \partial \theta_l}\Big|_{\hat{\theta}_i} \Delta\theta_i \Delta\theta_j \Delta\theta_k \Delta\theta_l \tag{4.54}$$

The blue term corresponds to the Fisher term, as is well known. The red term is referred to as the Flexion tensor, while the green term is known as the Quarxion tensor (SELLENTIN et al., 2014). A common issue that arises when using Taylor expansions for distributions is that higher-order terms can lead to non-normalizable contributions. To address this problem, (SELLENTIN et al., 2014) proposed an expansion based on the derivatives of the model function.

For the cosmological model, the DALI likelihood function is given by:

$$\begin{aligned} \log \mathcal{L}_\alpha = &-\frac{1}{2}(\partial_i \hat{\mu})\mathbf{M}(\partial_j \hat{\mu})\Delta\theta^{ij} \\ &- \left[\frac{1}{2}(\partial_{ij}\hat{\mu})\mathbf{M}(\partial_k \hat{\mu})\Delta\theta^{ijk} + \frac{1}{8}(\partial_{ji}\hat{\mu})\mathbf{M}(\partial_{jk}\hat{\mu})\Delta\theta^{ijkl}\right] \\ &- \left[\frac{1}{6}(\partial_i \hat{\mu})\mathbf{M}(\partial_{ijk}\hat{\mu})\Delta\theta^{ijkl} - \frac{1}{12}(\partial_{ij}\hat{\mu})\mathbf{M}(\partial_{km}\hat{\mu})\Delta\theta^{ijklm}\right] \\ &- \frac{1}{72}(\partial_{ijk}\hat{\mu})\mathbf{M}(\partial_{lmn}\hat{\mu})\Delta\theta^{ijklmn} \end{aligned} \tag{4.55}$$

where $\partial_i \hat{\mu} = \frac{\partial \hat{\mu}}{\partial \theta_i}$ represents the first-order derivatives of the theoretical model, $\partial_{ij}\hat{\mu} = \frac{\partial^2 \hat{\mu}}{\partial \theta_i \partial \theta_j}$ are second-order derivatives. Higher-order derivatives such as $\partial_{ijk}\hat{\mu}$ and $\partial_{ijkl}\hat{\mu}$ account for nonlinear effects in parameter space. The matrix $\mathbf{M}$ represents the inverse of the covariance of measurements.

To illustrate how DALI works, Figure 4.13 illustrates the confidence contours for the cosmological parameters ω_0 and Ω_m using different derivative approximation methods: Fisher, Doublet, and Exact Likelihood (gray area). These contours highlight the impact of considering higher-order derivatives in capturing the non-Gaussianities of the likelihood function.

Figure 4.13 - Derivative Approximation for Likelihood.

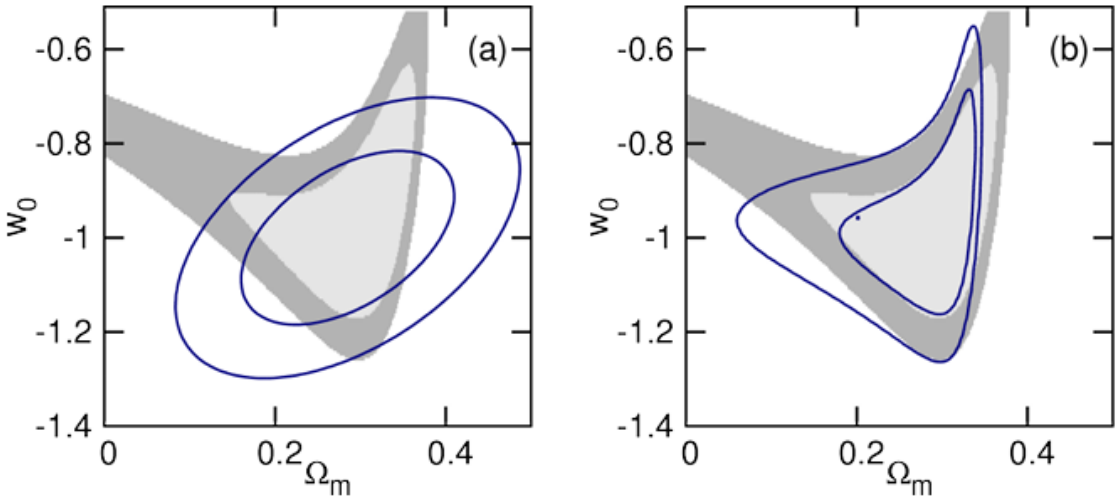

Distributions of ω_0 and Ω_M using different derivative approximation methods. The confidence contours are Fisher and Doublet, and the gray area is the exact likelihood.

SOURCE: Sellentin et al. (2014).

In the context of gravitational waves, the DALI likelihood is (SOUZA, 2023):

$$\begin{aligned}\log L \approx \log \mathcal{L}_0 &- \left[\frac{1}{2}\sum_{i,j}(\partial_i h(\theta)|\partial_j h(\theta))_0 \Delta\theta_i \Delta\theta_j\right] \\ &- \left[\frac{1}{2}\sum_{i,j,k}(\partial_i h(\theta)|\partial_j\partial_k h(\theta))_0 \Delta\theta^{ijk} + \frac{1}{8}\sum_{i,j,k,l}(\partial_i\partial_j h(\theta)|\partial_k\partial_l h(\theta))_0 \Delta\theta^{ijkl}\right] \\ &- \left[\frac{1}{6}\sum_{i,\ldots,l}(\partial_i h|\partial_j\partial_k\partial_l h)\Delta\theta^{ijkl} + \frac{1}{12}\sum_{i,\ldots,m}(\partial_i\partial_j h|\partial_k\partial_l\partial_m h)\Delta\theta^{ijklm}\right] \\ &+ \frac{1}{72}\sum_{i,\ldots,n}(\partial_i\partial_j\partial_k h|\partial_l\partial_m\partial_n h)\Delta\theta^{ijklmn} \\ &+ O(\mathcal{O}^4)\end{aligned} \tag{4.56}$$

where the terms have analogous interpretations as in the cosmological context, with derivatives now acting on the waveform model $h(\theta)$.

5 SURFING THE COSMIC WAVES: CONFRONTING THE HUBBLE TENSION WITH COSMO(GW)DALI

In this section, we present the results of our extensive research, which aims to address our results in cosmology through the analysis of gravitational wave data.

5.1 GWDALI

The detection and analysis of gravitational waves have revolutionized astrophysics, providing unprecedented precision in measuring fundamental parameters such as the masses, luminosity distances, and orbital inclinations of merging compact objects. As discussed by (SELLENTIN et al., 2014), traditional methods for parameter estimation often rely on Gaussian approximations of the likelihood function, a simplification that can prove inadequate in scenarios involving highly non-linear parameter spaces or degenerate likelihood surfaces. To address these limitations, GWDALI, a Python-based software, has been developed. Leveraging the Derivative Approximation for Likelihoods (DALI) method and the Fisher Matrix formalism, GWDALI enhances the accuracy and robustness of gravitational wave parameter estimation. By offering both Gaussian and non-Gaussian likelihood approximations, this software extends the applicability of parameter inference for signals observed by ground-based detector networks, enabling more reliable analyses in complex astrophysical scenarios (SOUZA, 2023; SOUZA; STURANI, 2023).

One of the software's key features is its ability to handle cases where the determinant of the Fisher matrix approaches zero. Unlike traditional methods that fail under these conditions, the program makes use of the DALI framework to estimate uncertainties using a combination of Monte Carlo [1] sampling and higher-order likelihood approximations (SOUZA, 2023).

[1] Monte Carlo sampling is a statistical technique widely employed to approximate probability distributions and evaluate integrals in high-dimensional parameter spaces. The method relies on generating random samples from a given distribution and using statistical analysis to estimate properties such as expectations, variances, or posterior distributions Metropolis1949. One of its most significant applications is in Bayesian inference, where Monte Carlo methods, particularly Markov Chain Monte Carlo (MCMC), are used to explore complex likelihood functions and posterior distributions Gelman2013. In gravitational wave astronomy, Monte Carlo sampling plays a crucial role in parameter estimation by efficiently probing the likelihood function associated with observed signals, allowing for accurate determination of source properties such as luminosity distance and sky location Veitch2010. Similarly, in cosmology, these methods are used to infer parameters of models such as the w_0w_aCDM framework, where likelihood evaluations involve integrating over multidimensional data spaces Lewis2002. The robustness of Monte Carlo techniques makes them indispensable for problems involving complex statistical distributions, particularly when analytical solutions are computationally intractable.

Unlike the Fisher matrix, which can struggle with degeneracies in inclination and distance, GWDALI incorporates higher-order corrections to improve luminosity distance precision. Besides, the tool is also equipped to forecast the precision of parameter estimation for arbitrary networks of gravitational wave detectors. It allows researchers to simulate the performance of current observatories, such as LIGO and Virgo, as well as future facilities, like the Einstein Telescope and Cosmic Explorer (like in this work). This functionality is critical for optimizing detector designs and ensuring maximal scientific output from gravitational wave observations (WANG et al., 2022). In addition to its theoretical advances, the software seamlessly integrates with existing data analysis tools. It supports the optional use of the LSC Algorithm Library (LAL) and Bilby, which enable exact or approximate likelihood sampling. These integrations make the program a versatile tool for both parameter estimation and methodological validation through extensive simulations (SOUZA; STURANI, 2023).

Furthermore, the software allows the selection of a method depending on the desired level of accuracy and computational feasibility: Fisher, Fisher Sampling, Doublet, and Triplet. Each method progressively incorporates higher-order corrections to improve the parameter estimation accuracy, and they are described in Table 5.1.

Table 5.1 - Summary of methods used to approximate the likelihood function in parameter estimation.

Method	Description	Usage
Fisher	Uses only the Fisher matrix to approximate the likelihood. Calculates the covariance matrix by inverting the Fisher matrix. It can fail when the Fisher matrix is not invertible due to degeneracies in parameter space.	Fast parameter uncertainty estimation with reasonable accuracy.
Fisher Sampling	Similar to the Fisher method but incorporates stochastic sampling of the likelihood to estimate uncertainties. Uses a Monte Carlo algorithm to obtain posterior distributions, providing a more reliable estimate when the Fisher matrix approximation fails.	Comparing Fisher-based results with Monte Carlo sampling to assess approximation validity.
Doublet	Expands the likelihood beyond the Fisher matrix by incorporating terms involving up to second-order derivatives. Includes the Flexion Tensor (third derivative) and the two-derivative part of the Quarxion Tensor (fourth derivative). Improves uncertainty estimates in cases where the Fisher matrix fails.	Useful when correlations or degeneracies affect the Fisher approximation.
Triplet	Further refines the likelihood approximation by including terms involving up to third-order derivatives. Incorporates additional contributions from the Quarxion Tensor, P-Tensor (fifth derivative), and H-Tensor (sixth derivative), providing a more accurate representation of the likelihood.	Capturing highly non-Gaussian uncertainties and improving precision in complex parameter spaces.

SOURCE: Souza and Sturani (2023).

The open-source nature of the tool ensures accessibility to the broader scientific community, fostering collaboration and driving further advancements in gravitational wave science. Recently, the software was used in the study by Ferri et al. (2024). He proposed and tested the Peak Sirens method, which uses the correlation between binary black holes (BBHs) detected by gravitational waves (dark sirens) and galaxies mapped by redshifts to measure the expansion of the universe in a way that is independent of cosmological models. To do this, the authors carried out thousands of full-sky simulations, incorporating gravitational lensing effects, errors in the location of BBHs, and the Milky Way mask. For that, the GWDALI code was used to estimate the uncertainties in the three-dimensional positions of gravitational wave events, taking into account errors in the luminous distance and angular location and the impact of the rotation of the Earth on the accuracy of the detectors. The results indicate that the method can determine H_0 with 7% accuracy using only LVK O5 and with less than 1% when employing future networks such as ET + 2CE, which makes it a promising tool to clarify Hubble tension (FERRI et al., 2024).

5.2 Mock data

In this study, due to the large amount of data, we used computing resources from a LIGO cluster based at the California Institute of Technology. The cluster's certification is managed by the LIGO Data Grid (LDG), and communication is established via Secure Shell Protocol (SSH). The LDG integrates the computational and data storage resources of the LIGO Scientific Collaboration (LSC) into a grid computing framework.

We generated 1000 simulated catalogs of bright sirens, each containing 300 gravitational wave detections with electromagnetic counterparts and a signal-to-noise ratio (SNR) greater than 8. These simulations assumed detection by third-generation (3G) detectors: Cosmic Explorer and Einstein Telescope [2].This extensive simulation is motivated by the fact that, to date, only one multi-messenger event (GW170817) has been observed, highlighting the need to explore a broader parameter space for future detections. To construct these catalogs, we employed the function `get_strain_snr` [3] from the `gw dali` package using the `'TaylorF2_py'` [4] approximant with frequency

[2]Since both detectors are still in the design phase and their sites are not yet fully defined, we consider the following geolocations: Detector 0 (CE): Longitude −119°, Latitude 46°, Rotation 45°, Shape 90°. Detector 1 (ET): Longitude 10°, Latitude 43°, Rotation 0°, Shape 60°. Detector 2 (ET): Longitude 10°, Latitude 43°, Rotation 120°, Shape 60°. Detector 3 (ET): Longitude 10°, Latitude 43°, Rotation −120°, Shape 60°.

[3]We developed our own code to generate the the GW signals, but thinking about time efficiency we decided to use the GWDALI function.

[4]he `TaylorF2` waveform is derived by expanding the orbital dynamics in powers of the orbital

parameters $f_{\min} = 1\,\mathrm{Hz}$, $f_{\max} = 10^4\,\mathrm{Hz}$, and $f_{\mathrm{size}} = 3 \times 10^3$.

The simulated source parameters included component masses (m_1 and m_2), right ascension (RA), declination (Dec), luminosity distance (d_L), inclination angle (ι), polarization angle (ψ), coalescence time (t_{coal}), and coalescence phase (ϕ_{coal}). The angular parameters such as RA and Dec were isotopically sampled uniformly to ensure a realistic sky distribution, m_1 and m_2 were modeled as $1.5 \times (1 + z[i])$ to account for redshift effects, while d_L was directly determined from the luminosity distance corresponding to each redshift $z[i]$ assuming the FlatLambdaCDM model $H_0 = 70km/Mpc/s$, $\Omega_m = 0.3$.

The redshift range $[0.05, 1]$. Although 3G detectors could detect sources up to 2 (being very optimistic) (SOUZA; STURANI, 2021), we focus on a smaller range, as EM counterpart detections can be too difficult to observe. The range is chosen because it balances detectability and signal strength, ensuring sufficient signal-to-noise ratios for detection by current and future observatories while remaining compatible with galaxy surveys like DES, LSST, and Euclid for host galaxy identification ((LEGACY COLLABORATION, 2021), (EUCLID CONSORTIUM, 2020)). It spans the transition from the matter-dominated to the dark energy-dominated regime (RYDEN, 2003), making it suitable for inferring the Hubble constant and cosmological parameters. Additionally, it aligns with astrophysical predictions that the majority of detectable compact binary mergers occur. This selection enhances statistical significance while avoiding challenges associated with very low ($z < 0.05$) or high ($z > 1$) redshifts, such as limited volume, weak signals, and difficulty in obtaining redshifts from electromagnetic counterparts considering future instruments.

Figure 5.1 presents the correlation matrix (See Appendice A) from one arbitrary source for the parameters simulated in our gravitational wave catalogs, including chirp mass ($\mathcal{M}_c$), symmetric mass ratio (η), luminosity distance (d_L), inclination angle (ι), polarization angle (ψ), and coalescence phase (ϕ). Notably, $\mathcal{M}_c$ and η show correlation, while ψ and ϕ exhibit negative correlation. Furthermore, d_L and

velocity, where the lowest-order terms describe the motion in the non-relativistic limit and higher-order terms include corrections due to the system's gravitational radiation. The model includes terms up to the 3.5 PN order, which captures a significant portion of the dynamics during the inspiral phase (BLANCHET, 2006; ARUN et al., 2009). These higher-order terms are essential for accurate modeling of the gravitational wave signal, particularly when considering the complex dynamics of compact binary systems. The `TaylorF2` approximation is based on a post-Newtonian (PN) expansion, which provides a series of corrections to the Newtonian description of the orbital dynamics, incorporating relativistic effects as the objects spiral toward each other. The `TaylorF2` model is commonly used in Bayesian inference methods for parameter estimation of binary systems, where it serves as a template for matching observed signals (VEITCH et al., 2015).

Figure 5.1 - Parameters correlation.

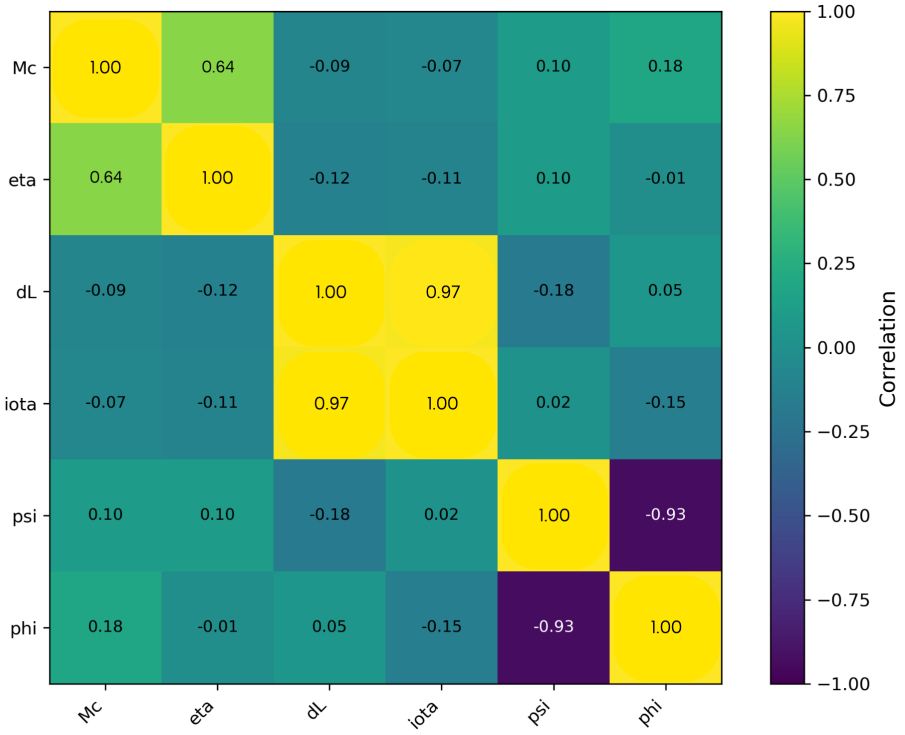

Correlation matrix of the main parameters simulated in the gravitational wave catalogs, including chirp mass ($\mathcal{M}_c$), symmetric mass ratio (η), luminosity distance (d_L), inclination angle (ι), polarization angle (ψ), and coalescence phase (ϕ).

SOURCE: Author.

ι display a high positive correlation. The strong correlations observed suggest that these parameters are not entirely independent, which can complicate their mutual estimation in gravitational wave analyses. Specifically, gravitational waves with inclinations closer to $\iota = 0°$ or $\iota = 180°$ produce stronger signals than those closer to $\iota = 90°$. As a result, a system may appear to be farther away than it actually is when it is oriented face-on, leading to a degeneracy between the luminosity distance d_L and the inclination ι (VITALE; EVANS, 2017). By contrast, parameter pairs with near-zero correlations (e.g., $\mathcal{M}_c$ and ψ) suggest more independent variations, potentially leading to more robust individual parameter estimates.

5.2.1 Bright Siren redshift distribution

The redshift distribution function used in this study takes into account a realistic scenario that assesses how far the proposed THESEUS[5] mission can detect the electromagnetic counterparts of coalescing neutron binaries. This distribution is modeled using the following expression (BELGACEM et al., 2019):

$$P(z) = \frac{1}{\mathcal{N}} \frac{z^3}{1 + \exp(10.6 z^{0.6})}, \tag{5.1}$$

where $\mathcal{N}$ is a normalization factor ensuring the distribution is properly normalized. This function represents the analytical fit of the bright siren distribution to be observed by combining THESEUS and ET (SOUZA; STURANI, 2021).

Recent studies, (BELGACEM et al., 2019), have explored potential coordination between the Einstein Telescope and THESEUS, examining the expected distribution profile of bright siren detections. It is anticipated that there will be around 500 detections over 10 years in optimistic scenarios, while pessimistic scenarios predict approximately 125 detections during the same timeframe (BELGACEM et al., 2019). In this context, we will utilize the analytical fit of these distributions as presented in (BELGACEM et al., 2019; SOUZA; STURANI, 2021). The comparison between the simulated redshift values (blue) and the analytic redshift distribution function $P(z)$ (red) is shown in Figure 5.2, illustrating the expected distribution of bright sirens detected by THESEUS.

5.3 Parameter estimation

5.3.1 Gravitational waves

After generating the sources, we proceeded to the parameter estimation phase using GWDALI. We chose six parameters for our analysis: the chirp mass ($\mathcal{M}_c$), the symmetric mass ratio (η), the luminosity distance (d_L), the inclination angle (ι), the polarization angle (ψ), and the coalescence phase (ϕ). Although our study focuses on bright sirens, we do not include the source's sky position (right ascension and declination) as free parameters. This is because we assume these coordinates are well-constrained, given that we start from a known redshift for each source. The estimations were done for Fisher and Doublet; for both methods, we used the sampler

[5]Transient High-Energy Sky and Early Universe Surveyor (THESEUS) is a proposed space-based observatory designed to detect and study transient astrophysical phenomena, particularly gamma-ray bursts. It aims to enhance multi-messenger astronomy by providing rapid electromagnetic counterparts to gravitational wave events.

Figure 5.2 - Brigth siren distribution.

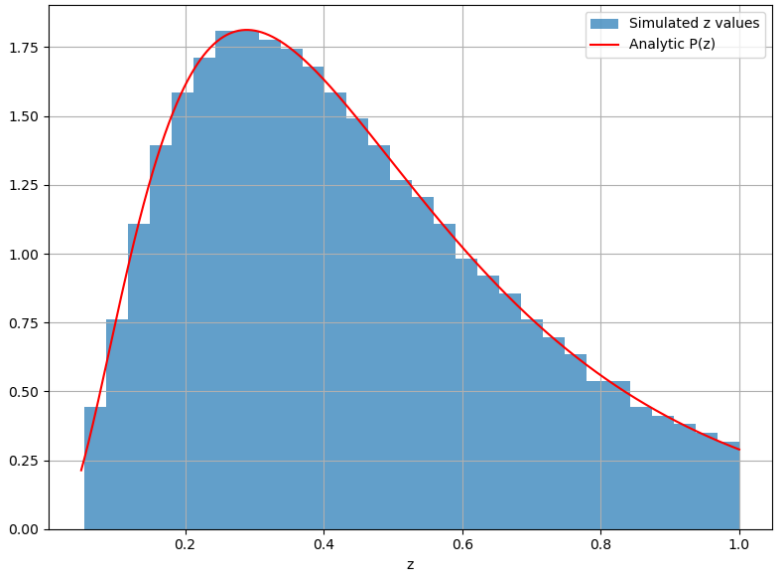

Histogram of simulated redshift values compared with the analytic redshift distribution function $P(z)$.

SOURCE: Author.

Nestle (nested sampling) with 300 live points.

Initially, we applied the Fisher method to obtain the uncertainties associated with the system's parameters. Prior definitions were unnecessary while running Fisher because in the GWDALI, Fisher considers the priors to be flat or uniform. The results of the Fisher method for the luminosity distance d_L for an arbitrary source are shown in Figure 5.3.

For Doublet analysis, it was necessary to define priors for each parameter. The prior distributions for the angular parameters (Euler Angles) used are listed in Table 5.2.

Table 5.2 - Prior distributions used in parameter estimation.

Parameter	**Prior Distribution**	**Range / Details**
ι	Sine	$[0, \pi]$
ψ	Uniform	$[0, \pi]$
ϕ_{coal}	Uniform	$[0, 2\pi]$

Figure 5.3 - GWDALI Fisher.

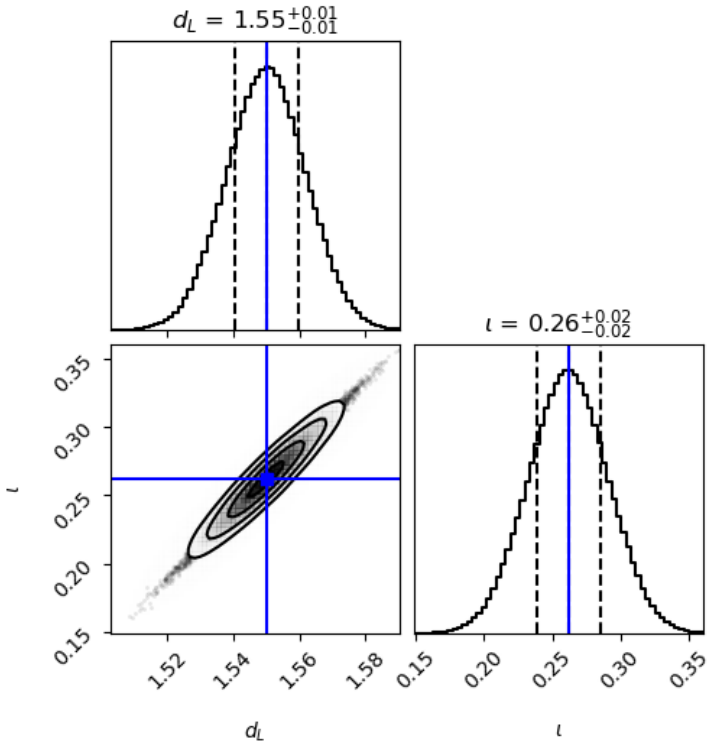

Parameter estimation using the Fisher method for the luminosity distance d_L.
SOURCE: Author.

For the parameters ι (inclination) and ψ (polarization), we used sine and uniform distributions, respectively. The uniform distribution for ψ and ϕ_{coal} (coalescence phase) assumes that all orientations are equally probable. The range for ι is typically chosen to be $[0, \pi]$, corresponding to a complete sweep of possible orientations of the binary system's orbital plane relative to the observer.

This range is selected due to some reasons (MAGGIORE, 2008); the value of $\iota = 0 = \pi$ corresponds to a face-on system, where the orbital plane is perpendicular to the line of sight of the observer. In contrast, $\iota = \pi/2$ represents an edge-on system, where the orbital motion is observed from the side, resulting in the most significant modulation of the gravitational wave signal. Due to the symmetry of gravitational waveforms, the face-on and edge-on configurations are indistinguishable from their inverted counterparts, making the range of ι span from 0 to π radians; Binary systems are generally expected to be more likely to have orbital planes oriented at intermediate angles, and the sine distribution ensures that these orientations are favored in the parameter estimation process (HOLZ; HUGHES, 2005; FARR

et al., 2010). Table 5.3 summarizes the custom prior distributions for the chirp mass ($\mathcal{M}_c$) and symmetric mass ratio (η), defined within a restricted range: In the

Table 5.3 - Custom prior distributions for $\mathcal{M}_c$ and η, represented as discretized uniform distributions.

Parameter	**Prior Distribution**	**Range**
Chirp Mass ($\mathcal{M}_c$)	Uniform (discretized)	$[\mathcal{M}_c(1-10^{-3}), \mathcal{M}_c(1+10^{-3})]$
Symmetric Mass Ratio (η)	Uniform (discretized)	$[\eta(1-10^{-3}), \eta(1+10^{-3})]$

context of GWDALI, when using the DOUBLET method, it is necessary to define the luminosity distance d_L in terms of its inverse and set its prior through the Jacobian transformation $\pi(d_L) \rightarrow \pi(d_L)^{-1}$. This is done to correct the bimodality between d_L and ι. Table 5.4 summarizes the priors. The impact of this transformation on the posterior distribution of d_L is shown in Figure 5.4. Comparing both, we can see that, when using *inv_dL* the peak of spurious bimodality is eliminated. This effect was also observed by (WANG et al., 2022).

Figure 5.4 - Comparison between DOUBLET with prior *inv_dL* and d_L.

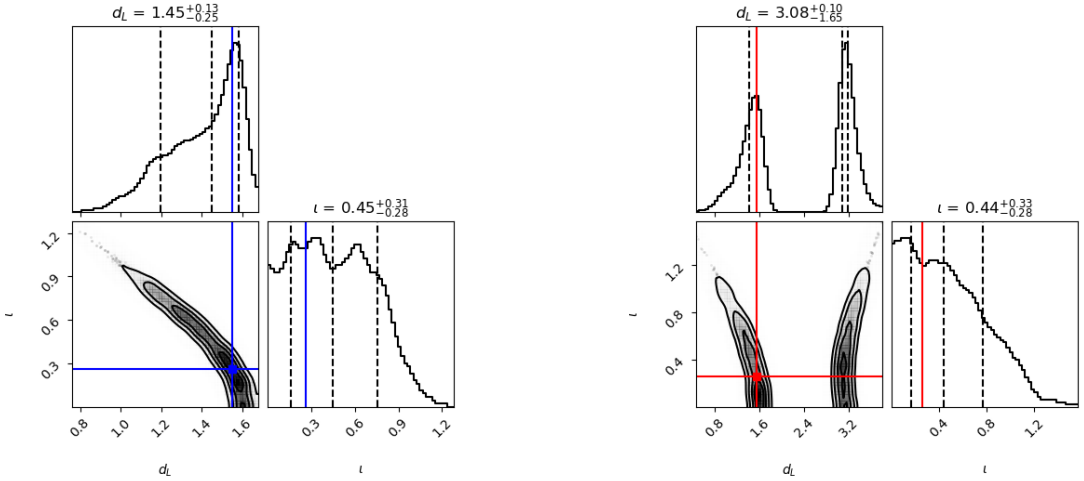

Doublet (*inv_dL*) Doublet d_L

(A)Posterior distribution of $1/d_L$ using the `DOUBLET` method, applying the Jacobian transformation. (B) Posterior distribution of d_L using the `DOUBLET` method.

SOURCE: Author.

Table 5.4 - Properties of the prior distribution for d_L. The prior in inv_dL is obtained via jacobian transformation of the prior in d_L, i.e. $\pi(d_L) = \pi(d_L) * d_L^2$.

Parameter	**Prior Distribution**	**Range**
d_L	Uniform	[0.02 Gpc, 8 Gpc]

For both methods, to quantify the uncertainty in parameter estimations, we used quantiles, which are statistics that divide an ordered distribution into equal probability parts. In the case of uncertainty with a 0.68 confidence level (CL), we considered the interquartile range (from the 16th to the 84th percentile), corresponding to approximately 1σ coverage in normal distributions. Thus, the errors in parameter estimation were obtained by:

$$\Delta\theta = \frac{\theta_{84} - \theta_{16}}{2}. \tag{5.2}$$

This method provides a robust estimation of uncertainties, avoiding the need to assume specific error distributions. To illustrate these results, we present Figure 5.5, which provides a direct visual comparison of the Fisher and Doublet estimations for d_L.

The top-left panel shows the luminosity distance as a function of redshift, with both the Fisher and Doublet methods yielding similar trends. As expected d_L increases with redshift (HOGG, 2000). Both methods provide consistent estimates, at higher redshifts, the uncertainty regions (shaded areas) become larger. This increase in uncertainty reflects the degradation of the signal-to-noise ratio (SNR) for distant sources. The Fisher method shows a slightly larger uncertainty region compared to Doublet at high redshift, suggesting that the latter might incorporate additional constraints that reduce variance.

The top-right panel illustrates the estimated inclination angle (ι) as a function of redshift. The bottom-left panel presents the relative error in luminosity distance. The Fisher method consistently maintains lower errors compared to Doublet, which exhibits larger fluctuations, especially at low redshifts. This suggests that Doublet may be more sensitive to specific configurations of the sources, leading to occasional large deviations. In fact, Doublet is sensitive to inclination angles around 90°. At higher redshifts, Doublet retains slightly higher variability but lower error. Since the accuracy of d_L directly impacts cosmological parameter estimation, methods with lower relative errors are preferable for standard siren measurements of the Hubble

Figure 5.5 - Analysis of luminosity distance and inclination angle estimation using different methods.

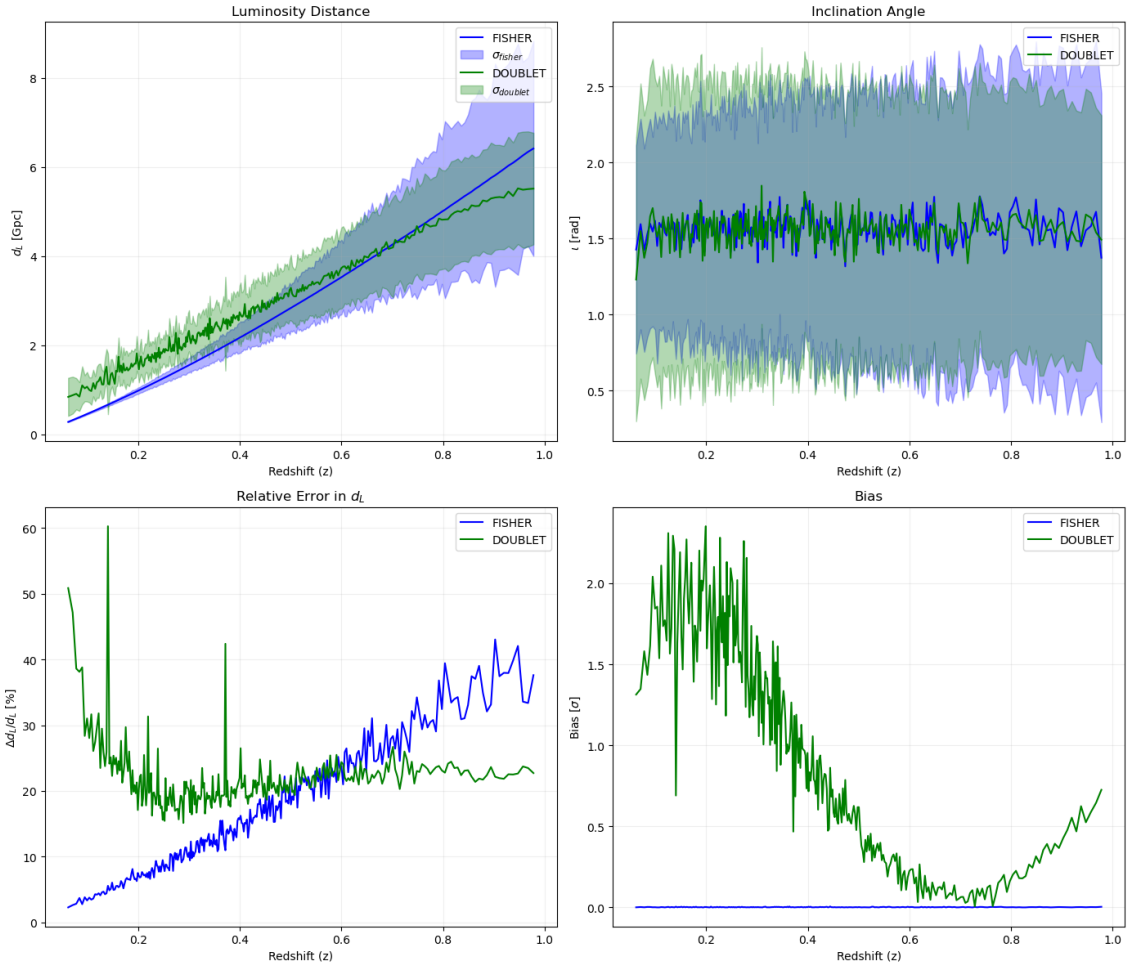

(5.3)

The top-left panel shows the luminosity distance d_L as a function of redshift, comparing the Fisher and Doublet methods, including dispersion regions. The top-right panel presents the estimated inclination angle ι versus redshift. The bottom-left panel displays the relative error in d_L, while the bottom-right panel illustrates the bias in d_L, with dispersion regions included.

SOURCE: Author.

constant (CHEN et al., 2018).

The bottom-right panel quantifies the bias in luminosity distance estimation. Fisher remains nearly unbiased across all redshifts, while Doublet exhibits a systematic bias. The spread in the uncertainty bands for both methods highlights the challenge of accurately recovering d_L. The growing uncertainty bands at high z further indicate challenges in maintaining precision at large distances, in agreement with previous studies on gravitational-wave parameter estimation (VITALE; EVANS, 2017).

5.3.2 Cosmological parameters

In this section, we employ the DALI method to estimate four cosmological parameters: the Hubble constant H_0, the matter density parameter Ω_M, and the parameters w_0 and w_a of the equation of state (EoS) of dark energy. These parameters are fundamental for understanding the expansion history of the Universe and its current dynamics. The fiducial values used for them are listed in Table 5.5, they are the same used for our Mock Data d_L, and the Fisher/DALI tensors were computed around them. To estimate the cosmological parameters, we applied Equation 4.56 and the method described in Section 4.4.3.

For gravitational wave parameter estimates, uncertainties are obtained by inverting the Fisher matrix. However, for cosmological parameter estimates, we sample from the approximate posterior associated with the Fisher term. This sampling was performed using the Bilby library with the nestle method, employing 1000 live points. The same procedure was applied to the Doublet, Triplet, and Exact Likelihood approaches. The priors used for each case are also listed in Table 5.5.

Table 5.5 - Cosmological reference parameters and priors.

Parameters	**Symbol**	**Fiducial Value**	**Priors**
Hubble Constant	H_0	70 km/s/Mpc	$60 \leq H_0 \leq 80$
Matter Density	Ω_m	0.3	$0.1 \leq \Omega_m \leq 0.9$
Equation of state	w_0	-1	$-2 \leq w_0 \leq -0.1$
Equation of state	w_a	0	$-5 \leq w_a \leq 5$

All priors were defined as uniform. A uniform prior assumes that all values within a given range are equally probable, thereby minimizing the influence of prior knowledge on the results (JOHNSON, 2005). For instance, setting $H_0 \sim U(60, 80)$ km s^{-1}

Mpc^{-1} encompasses the current range of estimates from cosmic microwave background (CMB) measurements and local distance ladder methods without imposing an artificial preference for one over the other (RIESS et al., 2022).

To further investigate the relationships between the estimated cosmological parameters, we present the correlation matrix from one arbitrary catalog in Figure 5.3.2. An anticorrelation is observed between H_0 and Ω_m, consistent with theoretical predictions, meaning a higher matter density leads to a slower expansion rate at early times, reducing the inferred value of H_0. This relationship is well-established in cosmological analyses, particularly from the Cosmic Microwave Background (CMB) and large-scale structure constraints (AGHANIM et al., 2020; PEEBLES, 1993).

The mild correlation between H_0 and ω_0 is expected since a more negative ω_0 enhances the late-time acceleration, which can lead to a lower inferred H_0, as well. However, given the degeneracy with ω_a this correlation is not as strong as the one with matter density.

Additionally, Ω_m exhibits a moderate positive correlation with w_0 and a strong positive correlation with its uncertainty, suggesting that a higher matter density leads to greater uncertainty in its estimation. The uncertainties in w_0 and w_a also display a high correlation, this is consistent with the well-known degeneracy between these parameters in dark energy models, where a higher expansion rate can be compensated by a less accelerating equation of state, as discussed in (HLOZEK et al., 2008; GONG; GAO, 2014). Their sigma are also highly correlated, as both parameters describe the same physical component (dark energy). The degeneracy between these two parameters leads to highly correlated uncertainties, making it difficult to constrain one parameter without precise knowledge of the other. To assess the influence of redshift (and consequently, the number of sources) on the parameter estimation, we divided the analysis into five progressively increasing and uniformly spaced intervals. The number of sources in each interval in each catalog is presented in Table 5.6.

Table 5.6 - Redshift Intervals and Number of Sources.

Redshift Interval	**Number of Sources**
0.05 - 0.24	69
0.05 - 0.43	168
0.05 - 0.62	237
0.05 - 0.81	278
0.05 - 0.99	300

Figure 5.6 - Correlation matrix of cosmological parameters and their uncertainties.

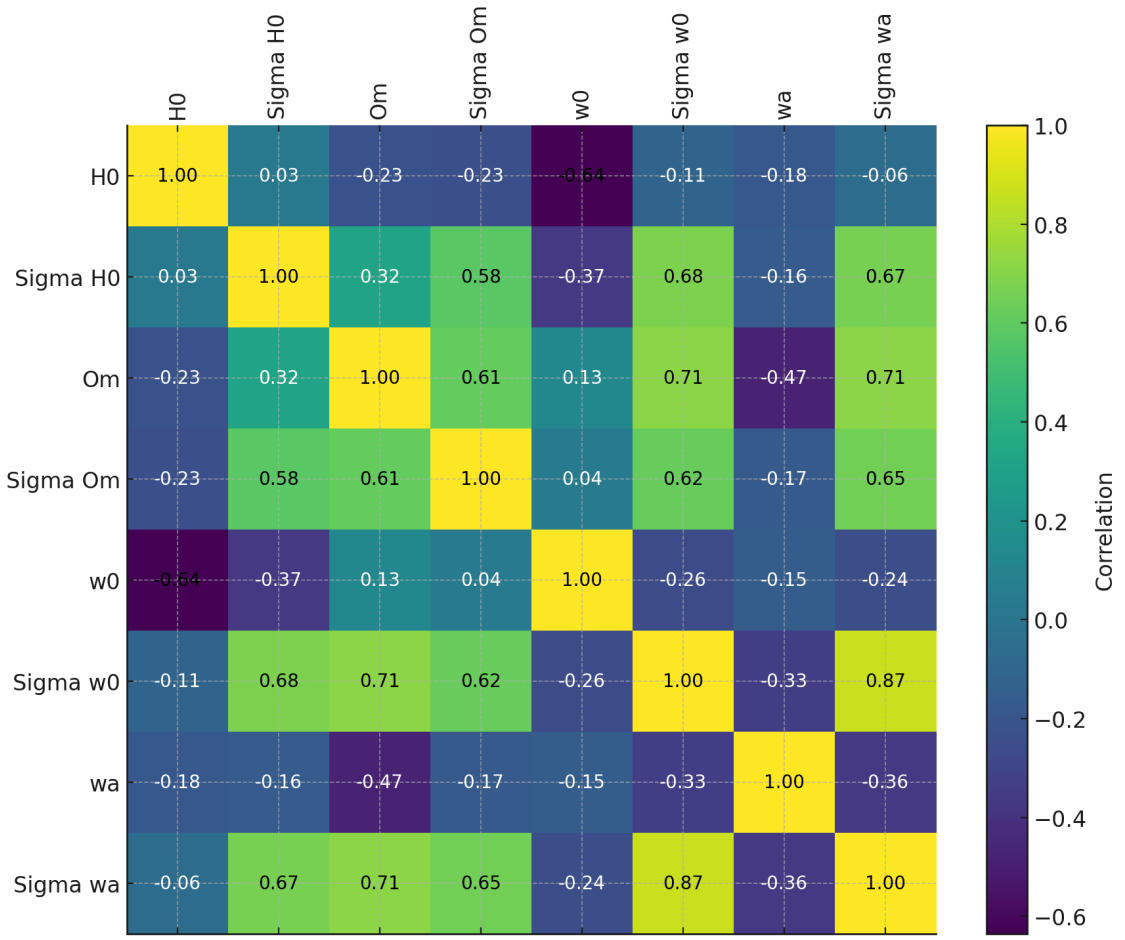

Correlation matrix of cosmological parameters and their uncertainties obtained using the DALI method. The color scale represents the degree of correlation, where yellow indicates a strong positive correlation, dark blue represents a negative correlation, and green suggests a weak or no correlation.

SOURCE: Author.

5.3.3 Cosmo GW(DALI)

The analysis of the GW(Fisher) cosmological results (see Figure 5.7) reveals that for the values of Ω_m the Fisher method exhibits the largest deviations from the fiducial value, particularly at lower redshifts, where the approximation of a Gaussian likelihood is less accurate. The Doublet method improves upon the Fisher estimate. The Triplet method, further refines the estimation, bringing it closer to the fiducial values. This improvement is expected, as higher-order approximations in the likelihood expansion allow for a more accurate representation of the underlying probability distribution.

When compared with the fiducial values of the dark energy equation of state parameter, ω_0, the Fisher approach presents deviations, particularly at lower redshifts. The Doublet method reduces these discrepancies at lower redshifts but still exhibits some offsets at higher, while the Triplet method significantly enhances the accuracy, if compared with the fiducial values. For time evolution of dark energy is parameterized by ω_a, the Fisher approach introduces a deviation from the fiducial value, particularly at lower redshifts. The Doublet and Triplet methods provide an improvement, with values oscillating around the fiducial values. For these three parameters, it is observed that the Fisher curve follows the Exact Likelihood plots, while Doublet and Triplet curves are more similar to each other.

Regarding H_0, the Fisher method provides a reasonable estimate but shows slight systematic offsets at high redshifts. The Doublet method refines this estimate, approaching the fiducial values, while the Triplet presented the smallest deviation across the redshift. It presents a behavior similar to the Doublet.

The analysis of the GW(Doublet) cosmological results (Figure 5.8 reveals for Ω_m that the Fisher approach deviates more from the fiducial values and the Exact Likelihood, when compared with the Doublet and Triplet. The same behavior is observed for the parameter ω_0. For ω_a we observe an unexpected behavior for the Exact Likelihood, it recovered really high values. Gong and Gao (2014) discuss the degeneracy between the cosmological parameters w_a and w_0 is a significant issue in observational cosmology, especially when characterizing dark energy. According to them, these two parameters are often adjusted simultaneously in analyses of cosmological data, such as supernova data, CMB (Cosmic Microwave Background), and other cosmological tests. However, the parameters can become highly degenerate, which means that in some cases, observational data cannot clearly distinguish between different combinations of these parameters. This degeneracy can affect the constraints in a positive way when w_0 and w_a are adjusted simultaneously, the degeneracy between them can result in a reduction of the estimated error in w_0. This occurs because, for certain values of w_a, the effects of dark energy can be masked, leading to better precision in the measurements of w_0, although the uncertainty in w_a may increase.

For H_0, the approximation methods yielded results similar to the fiducial values. Although the Exact Likelihood showed some deviation, it still recovered values in the expected range. In general, we did not anticipate such a high dispersion for the Exact Likelihood. The reasons for this variation in the parameters estimated from the GwDoublet data require further investigation.

Figure 5.7 - Plots of the cosmological parameters obtained from the GW(Fisher) catalog.

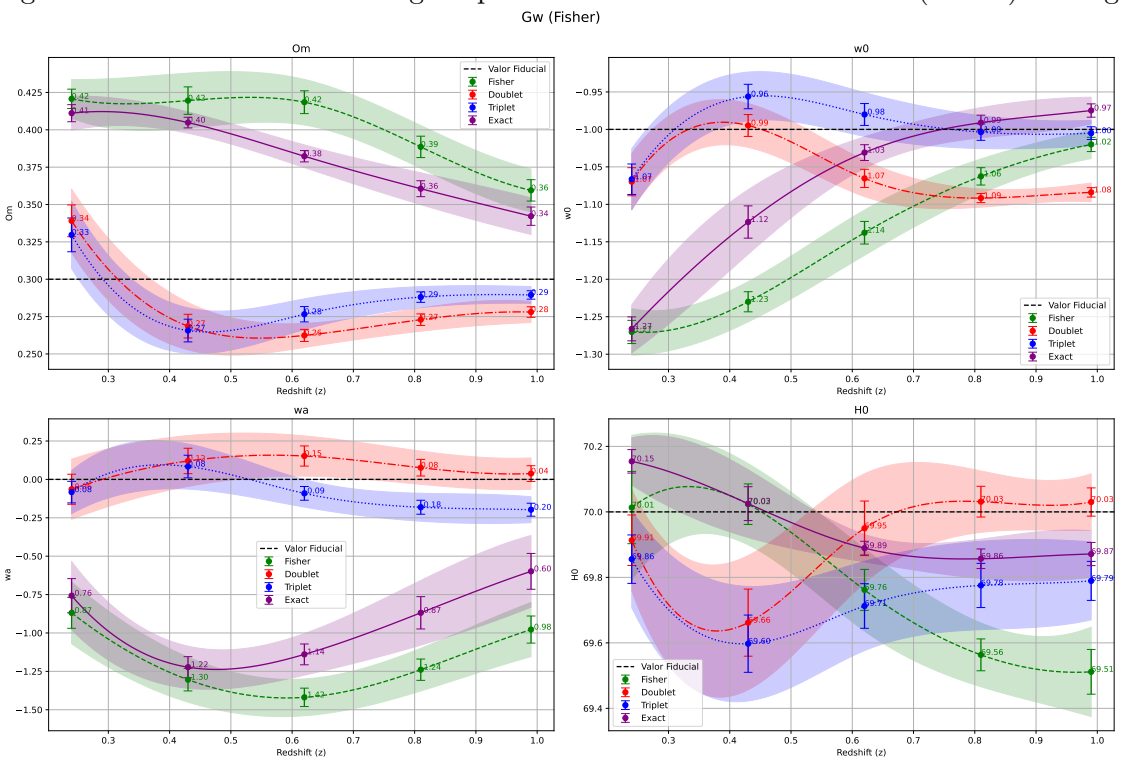

Cosmological parameters as a function of redshift. The green curves represent results from Fisher, red curves from Doublet, blue from Triplet, and purple from Exact Likelihood, the shadowed region is the dispersion over 1000 catalogs.

SOURCE: Author.

Figure 5.8 - Plots of the cosmological parameters obtained from the GW(Doublet) catalog.

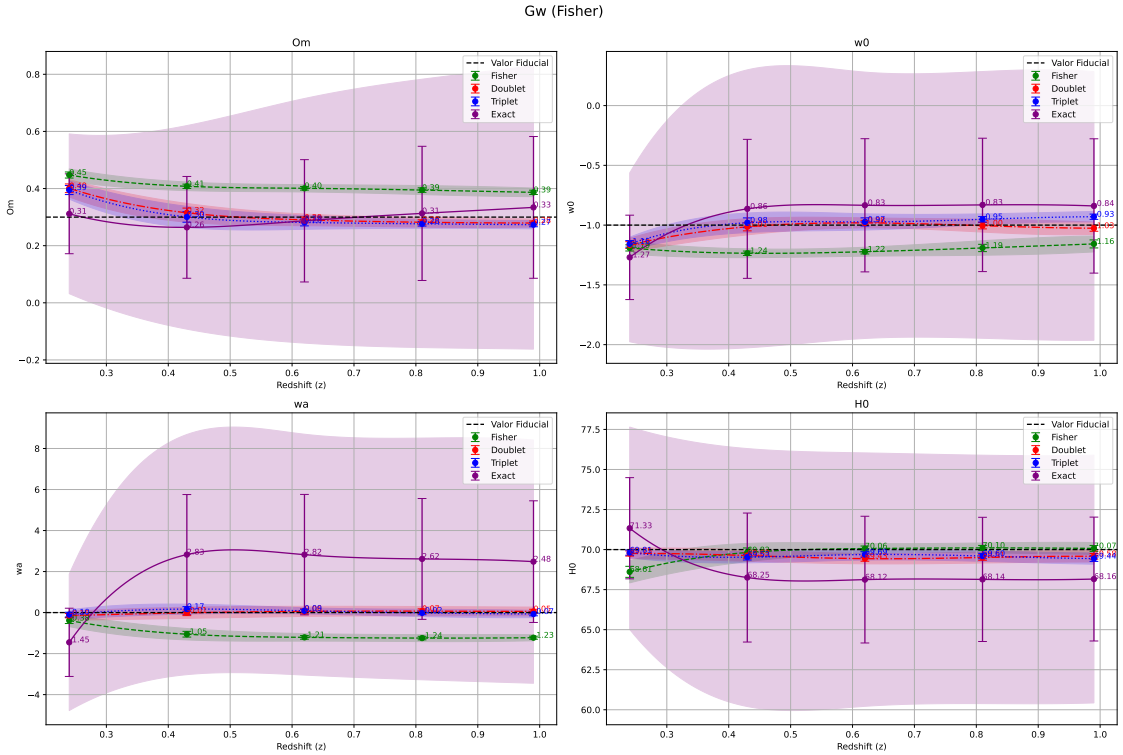

Cosmological parameters as a function of redshift. The green curves represent results from Fisher, red curves from Doublet, blue from Triplet, and purple from Exact Likelihood, the shadowed region is the dispersion over 1000 catalogs.

SOURCE: Author.

There are several methods for calculating DALI tensors: the frequentist approach, which involves averaging over several parameters values (WANG et al., 2022); the Bayesian approach, the tensors are calculated around the best fit (using a Maximum Likelihood Estimator MLE); and the direct approach, where tensors are calculated around fiducial values without averaging over the parameter space, as in the GW-DALI (SOUZA; STURANI, 2023). In this analysis, we employed the direct method, but this approach can fail if the peak of the exact posterior is not aligned with the fiducial values. This misalignment may explain some of the unexpected behaviors observed, though further investigation is required. We expect that computing the tensors around the best-fit values will minimize these irregularities and lead to more robust parameter constraints.

Table 5.7 - Average values of Ω_m, ω_a and ω_0 for different redshifts and methods.

	Ω_m mean		ω_a mean		ω_0 mean	
	GwFisher	GwDoublet	.	.	.	.
Fisher						
z = 0.24	0.42 ± 0.23	0.44 ± 0.24	-0.86 ± 3.12	0.38 ± 3.12	-1.27 ± 0.52	-1.19 ± 0.52
z = 0.43	0.41 ± 0.23	0.40 ± 0.24	-1.30 ± 2.94	-1.05 ± 2.94	-1.12 ± 0.48	-1.23 ± 0.56
z = 0.62	0.41 ± 0.22	0.40 ± 0.23	-1.41 ± 2.44	-1.20 ± 2.81	-1.13 ± 0.35	-1.22 ± 0.57
z = 0.81	0.38 ± 0.20	0.39 ± 0.21	-1.23 ± 2.44	-1.24 ± 2.74	-1.06 ± 0.24	-1.19 ± 0.55
z = 0.99	0.35 ± 0.18	-0.97 ± 0.24	-1.22 ± 1.56	-1.22 ± 2.71	-1.02 ± 0.18	-1.15 ± 0.54
Doublet						
z = 0.24	0.33 ± 0.24	0.39 ± 0.25	-0.06 ± 3.16	-0.14 ± 3.28	-1.06 ± 0.52	-1.15 ± 0.57
z = 0.43	0.26 ± 0.18	0.31 ± 0.21	-0.12 ± 2.70	-0.01 ± 3.01	-0.99 ± 0.48	-1.01 ± 0.57
z = 0.62	0.26 ± 0.16	0.29 ± 0.19	-0.15 ± 2.36	0.0 ± 2.83	-1.06 ± 0.29	-0.98 ± 0.54
z = 0.81	0.27 ± 0.15	0.28 ± 0.18	-0.07 ± 2.05	-0.0 ± 2.97	-1.09 ± 0.22	-0.99 ± 0.54
z = 0.99	0.27 ± 0.13	0.27 ± 0.14	-0.03± 1.80	-0.0 ± 1.29	-1.08 ± 0.19	-0.93 ± 0.44
Triplet						
z = 0.24	0.32 ± 0.22	0.38 ± 0.24	-0.08 ± 2.07	-0.10 ± 2.96	-1.06 ± 0.41	-1.14 ± 0.52
z = 0.43	0.26 ± 0.17	0.29 ± 0.21	-0.08 ± 1.76	-0.14 ± 2.57	-0.95 ± 0.48	-0.97 ± 0.52
z = 0.62	0.27 ± 0.13	0.28 ± 0.17	-0.09 ± 0.92	0.08 ± 2.83	-0.98 ± 0.33	-0.97 ± 0.49
z = 0.81	0.28 ± 0.09	0.27 ± 0.15	-0.18 ± 0.77	-0.0 ± 1.37	-1.00 ± 0.25	-0.95 ± 0.46
z = 0.99	0.28 ± 0.07	0.27 ± 0.14	-0.19± 0.74	-0.06 ± 1.29	-1.00 ± 0.20	-0.93 ± 0.44
Exact						
z = 0.24	0.41 ± 0.14	0.31 ± 0.14	-0.75 ± 3.08	-1.45 ± 2.77	-1.25 ± 0.44	-1.26 ± 0.41
z = 0.43	0.40 ± 0.11	0.26 ± 0.13	-1.22 ± 2.20	-2.82 ± 1.80	-1.12 ± 0.27	-0.86 ± 0.24
z = 0.62	0.38 ± 0.10	0.28 ± 0.12	-1.13 ± 1.90	-2.82 ± 1.57	-1.03 ± 0.16	-0.83 ± 0.24
z = 0.81	0.36 ± 0.09	0.31 ± 0.11	-0.86 ± 1.71	-2.61 ± 1.51	-0.99 ± 0.12	-0.83 ± 0.24
z = 0.99	0.34 ± 0.09	0.33 ± 0.11	-0.59 ± 1.56	-2.48 ± 1.48	-0.97 ± 0.10	-0.83 ± 0.25

5.3.3.1 Measurements relative error and bias

In experimental and observational studies, it is crucial to assess the accuracy and precision of measurements. Two fundamental metrics for evaluating measurement errors are the relative error and bias. These indicators help quantify how much a measured value deviates from the expected or true value. The relative error is often defined as the ratio between the absolute error and the true or expected value. It is defined mathematically as (WALPOLE et al., 2007):

$$\varepsilon_r = \frac{\sigma}{X_{\text{measured}}} \tag{5.4}$$

where X_{measured} is the estimated value.

The relative error provides a standardized way to compare errors across different measurements. The bias of a measurement represents the systematic error, which indicates whether a measurement consistently overestimates or underestimates the true value. It is given by (WALPOLE et al., 2007):

$$B = \frac{X_{\text{measured}} - X_{\text{true}}}{\sigma} \tag{5.5}$$

where $|B| > 1$ implies a significant deviation of the measurement (far from the real/fiducial value) and $|B| < -1$ implies it is a reliable measurement, i.e. the real/fiducial value is within 1-sigma of your measurement. Therefore, we analyzed the bias and error for each parameter.

5.3.3.2 Cosmo GW(Fisher) bias and error

Ideally, a cosmological model should display low and stable biases across all redshifts. In Figure 5.9, are compared the approximation methods: Fisher, Doublet, Triplet, and Exact Likelihood. The trends observed in the bias estimation indicate a systematic underestimation in the lower-order method, which assumes a Gaussian likelihood. The biases associated with H_0 remain relatively low across all methods, whereas those for Ω_m, ω_0, and ω_a exhibit significant deviations. The Fisher method consistently underestimates the bias, while the inclusion of higher-order corrections through the Doublet and Triplet methods progressively reduces systematic deviations. The Exact Likelihood approach, provides the most accurate parameter estimates.

The errors on ω_0 and ω_a are high. These results align with historical findings on parameter estimation trends. Croft and Dailey (2015) documented the evolution of cosmological parameter uncertainties over two decades and highlighted systematic underestimations of errors, particularly in dark energy constraints. The trends observed in the present study mirror those findings, with the bias in ω_0 and ω_a following a similar pattern of reduction as methodologies improve. The historical study emphasized that error bars on H_0 and Ω_m stabilized around the early 2000s, whereas dark energy parameters continued to exhibit significant variations as new constraints emerged.

These results should be interpreted in the context of ongoing efforts to refine cosmological constraints through gravitational wave observations. The analysis by Croft and Dailey (2015) emphasized the role of systematic uncertainties in shaping past parameter estimates, a concern that remains relevant given the observed biases in the

present study. The findings suggest that while higher-order corrections improve parameter constraints, further methodological advancements are necessary to achieve the precision required for robust dark energy measurements. Meanwhile, the relative errors of Ω_m remain well constrained across different methodologies, in agreement with previous findings in the literature.

The precision of H_0 estimations from gravitational wave standard sirens has been studied, with forecasts suggesting that third-generation detectors such as the Einstein Telescope (ET) and Cosmic Explorer (CE) could achieve sub-percent uncertainties in H_0 in the ΛCDM framework (VITALE; EVANS, 2017), while more flexible models like $\omega_0\omega_a$ CDM may retain errors at the few percent level (FERRI et al., 2024). The relative errors obtained here, for GW(Fisher) data, further support these expectations, with Fisher estimates yielding an uncertainty of approximately 2-3%, the Doublet method exhibiting a slightly broader range of 2-4%, the Triplet method maintaining errors between 2-3%, and the Exact Likelihood approach achieving a precision of 1%.

Figure 5.9 - Bias and error results for Cosmo(Methods) with GW(Fisher).

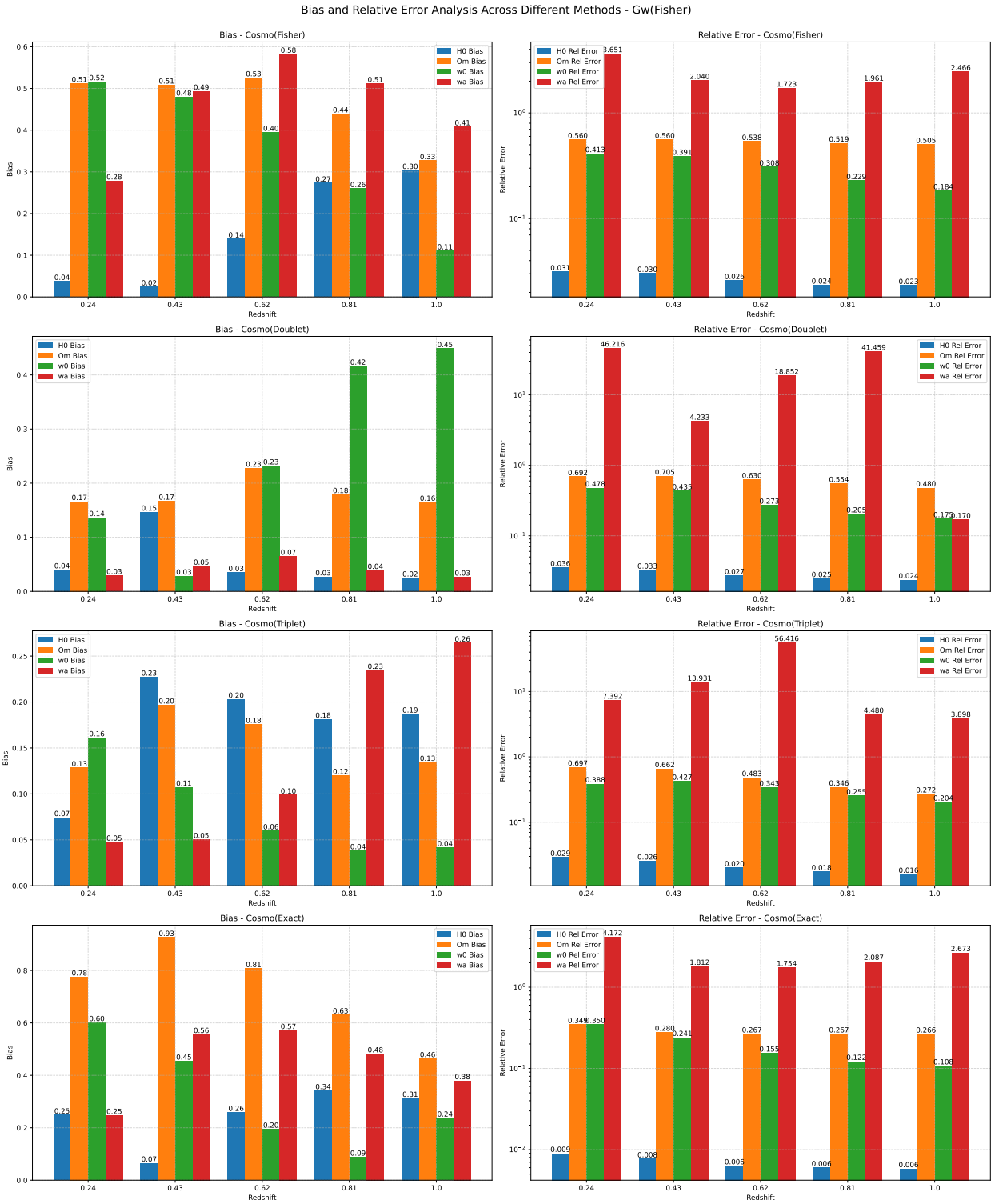

SOURCE: Author.

5.3.3.3 Cosmo GW(Doublet) bias and error

We evaluated the performance of different methods using gravitational-wave data analyzed with the Doublet approach. The bias in H_0 s relatively low across all methods, consistent with the expectation that the Hubble constant is among the best-constrained parameters in cosmological analyses. The Fisher, Doublet, and Triplet methods yield biases below 0.1, indicating their robustness. However, the Exact Likelihood method presents an anomaly, with extreme high bias across all parameters. This discrepancy suggests that the d_L measurements with GWDALI/Doublet were not reliable. Incorrect d_L measurements lead to biased cosmological parameter estimates, increasing systematic errors. In the Fisher/Doublet case for GW parameters, the tensors have already been calculated around the fiducial values, leading to 'better' measurements of the cosmological parameters. In other words, we overestimated the DALI in this case because we did not take into account the possible biases in the exact likelihood.

The matter density parameter exhibits moderate bias in the Fisher, Doublet, and Triplet approaches, with progressive improvement as higher-order corrections are introduced. The Fisher method underestimates bias, while the Doublet and Triplet methods significantly reduce it. Dark energy equation of state parameters exhibit the highest biases, consistent with previous findings that constraints on ω_a and ω_0 remain among the most challenging in cosmology. The Fisher and Doublet methods show progressively decreasing bias.

The relative error analysis provides of H_0 insight into the precision of parameter estimation across methods. The Fisher method provides an uncertainty of approximately 5–7%, while the Doublet and Triplet methods offer slight improvements. As expected, dark energy parameters exhibit the largest relative errors. The Fisher and Doublet methods yield uncertainties as high as 10–50%, while the Triplet method stabilizes relative errors at around 8–20%. Additionally, previous works using gravitational-wave standard sirens, such as Abbott et al. (2017) (ABBOTT et al., 2017c), reported uncertainties around $10\% - 30\%$, demonstrating that while bright sirens provide valuable redshift information, their impact on reducing the uncertainty in H_0 remains constrained by errors.

Figure 5.10 - Bias and error results for Cosmo(Methods) with GW(Doublet).

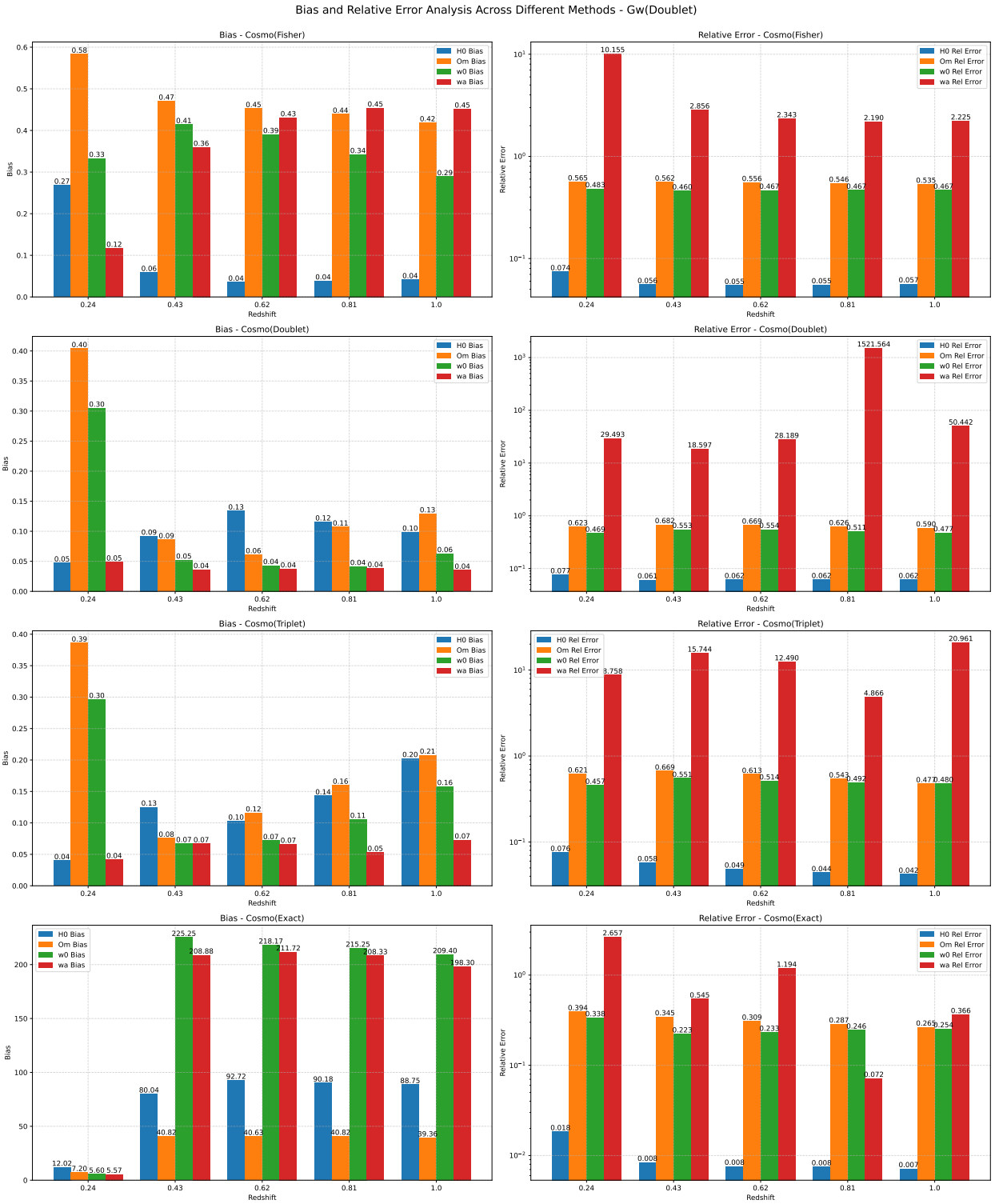

SOURCE: Author.

These findings highlight that higher-order corrections improve parameter constraints. However, while the Exact Likelihood approach theoretically provides the most precise constraints, its high bias questions the trade-off between accuracy and precision in this case. The unexpected systematic deviations call for a deeper investigation into the role of priors, numerical instabilities, and potential overfitting in likelihood computations.

5.3.4 Hubble tension

Figure 5.11 presents the estimated distributions of the Hubble constant (H_0) for five redshift bins computed using four distinct methods: Fisher (top-left), Doublet (top-right), Triplet (bottom-left), and the Exact likelihood (bottom-right). In each panel, every curve corresponds to a specific redshift range, while the vertical dashed lines indicate the central tendency (e.g., median) of H_0 for each distribution.

This figure demonstrates that the higher-order DALI expansions more accurately reproduce the shape of the Exact likelihood compared to the standard Fisher approach (the Fisher distributions are more spread). Specifically, the Fisher distributions deviate from the exact likelihood in terms of peak location, width, and tails. This discrepancy arises because the Fisher method, being a first-order approximation around the likelihood maximum, can underestimate or misrepresent the tails when the true likelihood exhibits non-Gaussian features. In contrast, the Doublet and Triplet approaches incorporate second-order and third-order derivatives, respectively, thereby capturing skewness, kurtosis, and other higher-order effects absent in the Fisher approximation (SELLENTIN et al., 2014).

Upon closer inspection, the exact likelihood (Bottom-Right) serves as the benchmark, representing the full functional form without relying on series expansion. In the Fisher panel (Top-Left), the distributions are noticeably narrower or shifted relative to the exact likelihood—a consequence of assuming Gaussian errors around the best-fit point, which may lead to an underestimation of uncertainties in non-Gaussian scenarios. Interestingly, while one might expect that redshift bins with a larger range (and thus more sources) would yield broader distributions, the Fisher method shows similar widths across different curves.

In the Doublet panel (Top-Right), the distributions align more closely with the exact likelihood, indicating enhanced accuracy due to the inclusion of second-order corrections in the DALI expansion. The Triplet panel (Bottom-Left) further improves on this, with distributions that track the exact likelihood very closely, particularly at

higher redshifts where non-linearities in the distance–redshift relation amplify non-Gaussian effects. This observation underscores the benefit of incorporating third-order terms in reducing systematic deviations. Regarding redshift dependence, both higher-order methods reveal that larger redshift ranges result in a more pronounced (thicker) H_0 distribution, reflecting increased precision relative to the broader distributions observed at lower redshifts.

Figure 5.12 presents different results obtained using the GW(Doublet) dataset. The plot on the Exact Likelihood (botton-left) produces wider distributions due to the high bias. The plots shows that the approximation methods present wider curves if compared with the results from cosmological GW(Fisher). This behavior follows the wider distribution of the Exact Likelihood, if compared with the Exact Likelihood from GW(Fisher) cosmological parameters.

Figure 5.11 - Comparison of mean H_0 and σ_{H_0} for the Gw(Fisher) method.

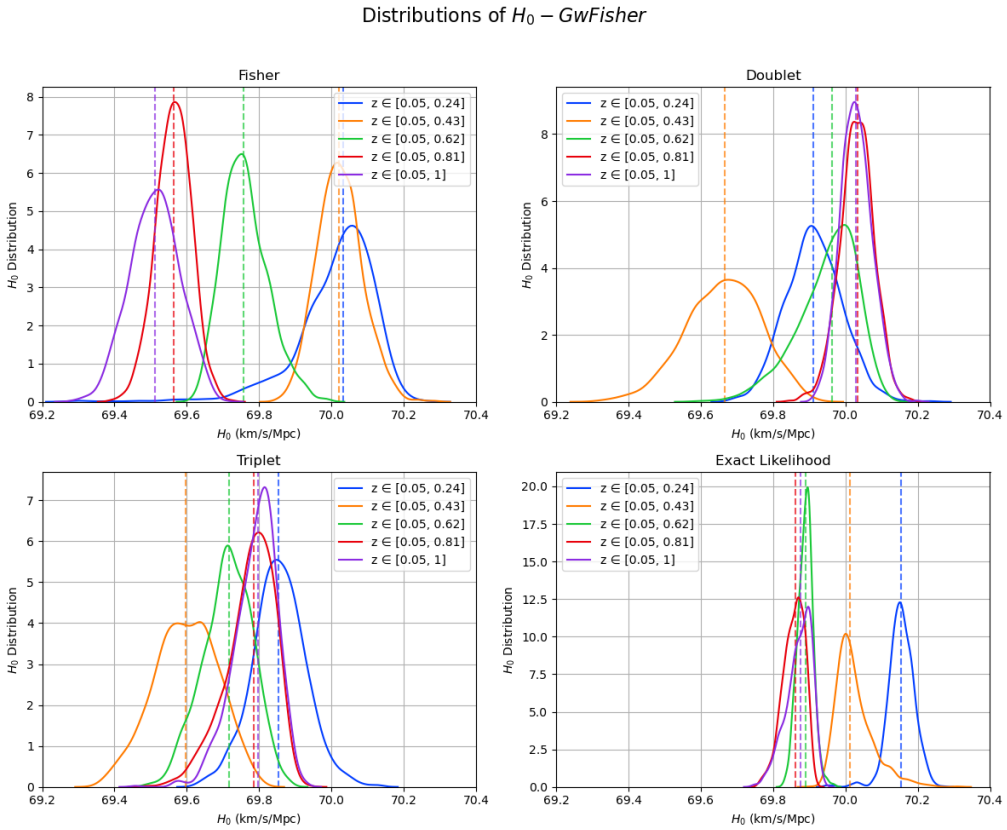

SOURCE: Author.

Table 5.8 presents H_0 as a function of redshift and method. The general trend indi-

Figure 5.12 - Comparison of mean H_0 and for the GW(Doublet) method.

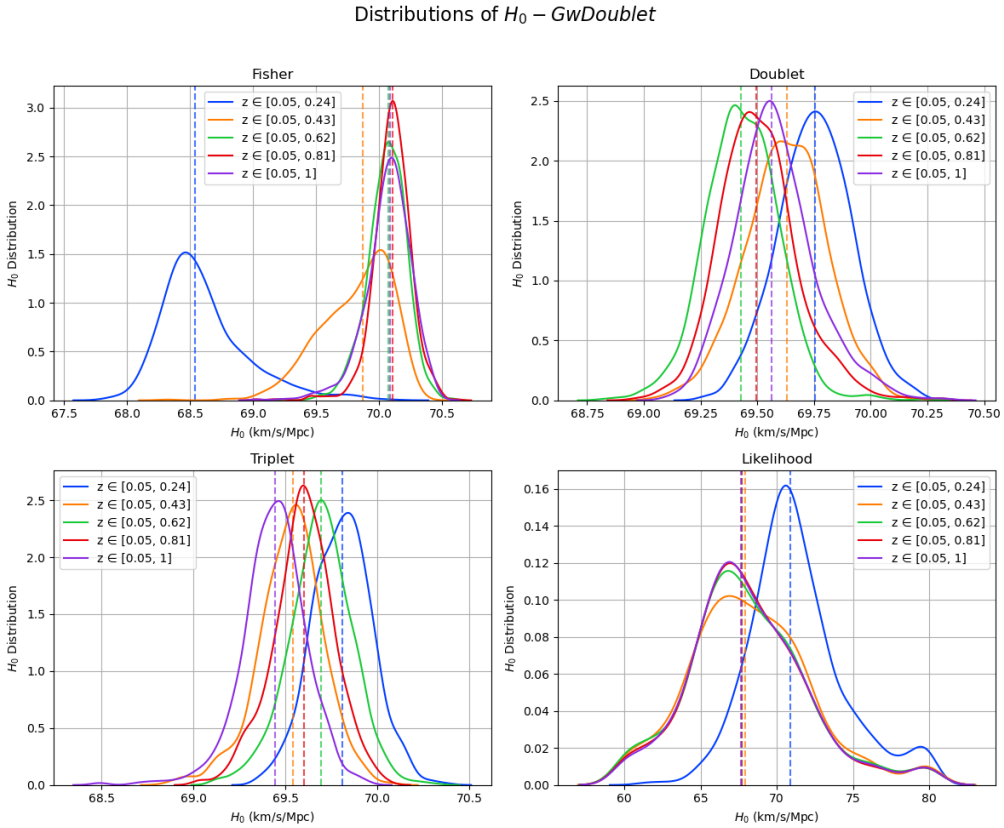

SOURCE: Author.

cates that the meaning of H_0 variates between 69.5 and 70.8 km/s/Mpc, depending on the method and redshift analyzed. These values are in the range of those obtained from the *Planck* CMB data ($H_0 = 67.4 \pm 0.5$ km/s/Mpc) and the tip of the red giant branch (TRGB) method ($H_0 = 69.8 \pm 1.9$ km/s/Mpc), but lower than the values reported by SH0ES ($H_0 = 73.04 \pm 1.04$ km/s/Mpc). This intermediate positioning suggests that the methodology employed acts as a compromise between the constraints from the early universe, as inferred from the cosmic microwave background (CMB), and those obtained from the local distance ladder. However, differences emerge when considering the method employed.

Comparing the approximation methods, for the GwFisher cosmological parameters (yellow background) estimates remain consistent across different values of redshift parameter and methods. The GwDoublet cosmological parameters (blue background) are similar to those from GwFisher, with minor variations, but the uncertainties are marginally larger.

Table 5.8 - Table of results organized for Cosmo(Exact), Doublet and Triplet with different colours for each z.

	H_0 mean		σ Planck		σ SH0ES	
	GwFisher	GwDoublet	.	.	.	.
Fisher						
z = 0.24	70.01 ± 2.22	68.61 ± 5.13	1.17	0.23	1.36	0.85
z = 0.43	70.02 ± 2.14	68.87 ± 3.70	1.22	0.67	1.41	0.86
z = 0.62	69.76 ± 1.84	70.06 ± 3.87	1.28	0.73	1.78	0.83
z = 0.81	69.56 ± 1.30	70.10 ± 3.67	1.30	0.73	2.10	0.80
z = 0.99	69.51 ± 1.64	70.07 ± 4.10	1.29	0.66	2.15	0.72
Doublet						
z = 0.24	69.91 ± 2.51	69,75 ± 5.37	1.00	0.44	1.15	0.60
z = 0.43	69.66 ± 2.30	69.63 ± 4.31	0.98	0.51	1.47	0.77
z = 0.62	69.95 ± 1.94	69.43 ± 4.33	1.31	0.47	1.59	0.81
z = 0.81	70.03 ± 1.76	69.51 ± 4.36	1.49	0.48	1.71	0.8
z = 0.99	70.03 ± 1.69	69.58 ± 4.36	1.56	0.50	1.78	0.77
Triplet						
z = 0.24	69.86 ± 2.08	69.81 ± 5.32	1.15	0.45	1.37	0.60
z = 0.43	69.60 ± 1.81	69.53 ± 4.08	1.17	0.52	1.65	0.86
z = 0.62	69.71 ± 1.43	69.69 ± 3.62	1.53	0.73	1.89	0.86
z = 0.81	69.78 ± 1.25	69.60 ± 3.66	1.77	0.73	2.01	0.81
z = 0.99	69.79 ± 1.14	69.44 ± 2.99	1.93	0.72	2.11	0.80
Exact						
z = 0.24	70.15 ± 0.64	71.33 ± 1.45	3.38	2.70	2.36	1.17
z = 0.43	70.03 ± 0.56	68.25 ± 0.70	3.51	1.23	2.56	6.89
z = 0.62	69.89 ± 0.45	68.12 ± 0.63	3.69	1.15	2.78	7.82
z = 0.81	69.86 ± 0.43	68.14 ± 0.67	3.73	1.10	2.83	7.31
z = 0.99	69.87 ± 0.42	68.16 ± 0.59	3.80	1.28	2.83	8.23

Additionally, comparing these results with those in the literature emphasizes that the Hubble tension remains unresolved. The values obtained in this study are higher than the Planck 2018 results, but they remain systematically lower than the SH0ES results. This trend aligns with recent discussions in the literature, such as those presented in Di Valentino et al. (2021) and Palmese et al. (2023). Besides that, while the methodologies explored in this study provide intermediate values of H_0, they

do not significantly alleviate the Hubble tension. Instead, they reinforce the idea that the discrepancy persists and is not merely a consequence of statistical approximations but rather an indication of potential underlying physics that remains to be fully understood. This aligns with recent analyses that emphasize the robustness of the tension across multiple independent measurements (VALENTINO et al., 2021; HU; WANG, 2023). The results also highlight the importance of considering non-Gaussian effects in cosmological parameter estimation, as evidenced by the differences in uncertainty levels among the different methods. This has been discussed in previous works, which suggest that a more detailed exploration of higher-order likelihood expansions may be necessary to fully capture the constraints on the Hubble Tension (PALMESE et al., 2020).

Future research should focus on higher-order likelihood approximations to further refine the estimation of H_0. Additionally, it is important to investigate some unexpected results related to the GwDoublet cosmological parameters. Our best approach may be to apply the best fit when calculating the tensors, rather than calculating them around the fiducial value. We anticipate that this will yield results that are closer to the exact likelihood.

Furthermore, exploring new physics scenarios, such as early dark energy and modified gravity models, has been suggested (HU; WANG, 2023) as a potential solution to the current discrepancy. A comprehensive strategy that integrates various observational techniques and enhances statistical methodologies will be crucial for resolving the Hubble tension in the coming years.

6 CONCLUSIONS AND PERSPECTIVE

In this study, we analyzed the estimation of the Hubble constant and others cosmological parameters using bright sirens. Specifically, we simulated 1000 catalogs of bright sirens, each containing 300 gravitational wave events detected by next-generation detectors—Cosmic Explorer and Einstein Telescope—considering a signal-to-noise ratio (SNR) threshold of 8. Given the current scarcity of multi-messenger detections, this extensive simulation aimed to explore the statistical robustness of cosmological inference using bright sirens and assess the accuracy of different parameter estimation methods. To extract cosmological information, we employed the DALI method (Fisher, Doublet, and Triplet) alongside with the Exact Likelihood

- **Methodological Comparisons:** Among the statistical methods, the Fisher, Doublet, and Triplet approaches are stable and robust estimates. The examination of bias and relative error across our models revealed that Cosmo(Fisher), Cosmo(Doublet), and Cosmo(Triplet) maintain low and predictable biases. These insights stress the importance of cross-validating methods to avoid systematic pitfalls in parameter estimation. The DALI method has been used in other research (WANG et al., 2022; FERRI et al., 2024; SOUZA; STURANI, 2023), and can be very useful when estimating parameters. We need to further investigate the unexpected results encountered during this research. Some actions we can take include using the best-fit method to calculate the tensors instead of calculating them around the fiducial values. Additionally, we can explore other approximants besides TaylorF2, such as "IMRPhenomD" (HUSA et al., 2016; KHAN et al., 2016) or "IMRPhenomHM" (LONDON et al., 2018).

This study highlights the significant potential of bright sirens for precision cosmology in the era of third-generation gravitational wave detectors. By applying advanced likelihood approximations, we demonstrated that higher-order expansions (Doublet and Triplet) improve parameter estimation as compared to the Fisher method. Although challenges remain—particularly in addressing systematic uncertainties—the results reinforce the importance of gravitational waves as an independent cosmological probe.

Future gravitational wave observatories, along with large galaxy surveys, will help us better measure the Hubble constant and test our cosmological model. Improved

methods will make standard sirens a useful tool for addressing cosmological tensions. Looking ahead, there are several areas we should explore further:

- **Refinement of Statistical Frameworks:** Future analyses should explore DALI tensor calculations around best-fit values rather than fiducial values to mitigate the observed systematic deviations. A detailed investigation into the numerical instabilities observed in the Exact Likelihood method is needed. Enhancements such as improved parameterizations or Monte Carlo simulations could help mitigate these issues and improve reliability.
- **Expanded Redshift Coverage:** As we push toward higher redshift observations, the challenge of maintaining precision and minimizing bias will grow. Systematic studies focusing on how cosmic evolution impacts parameter estimation are vital for unlocking a more complete picture of cosmic history.
- **Analyses with Second-Generation Detectors:** An immediate extension of this work would involve carrying out the same analyses using data from second-generation (2G) gravitational wave detectors. By comparing the resulting H_0 estimates with those obtained from third-generation (3G) detectors, we can assess the consistency of our methodologies across different detector sensitivities and noise characteristics. Such a comparative study may help isolate potential systematic differences and refine our error models.
- **Expansion to Dark Sirens:** With the concept of the Hubble tension in mind, the current research could be expanded to include dark sirens. Incorporating dark siren data would require a comprehensive analysis of extensive galaxy catalogues from major collaborations and surveys (e.g., SDSS, DES, LSST, Pan-STARRS). By cross-correlating gravitational wave data with these galaxy surveys, it may be possible to statistically infer host galaxy properties and improve cosmological parameter estimates, thereby complementing the standard siren approach.

Each of these future directions not only promises to enhance the robustness of cosmological inference using gravitational waves but also paves the way for new collaborations between the gravitational wave and astronomical survey communities. By integrating a variety of datasets and utilizing advancements in detector technology, we can move closer to addressing persistent issues such as the Hubble tension.

In summary, our current findings support the idea that gravitational wave standard sirens can serve as independent tools for studying cosmology. However, they also highlight the complexities involved in achieving high-precision measurements in this field. By tackling these challenges directly and utilizing advanced observational technologies, we have the opportunity to enhance our understanding of the Universe.

REFERENCES

ABBOTT, B.; ABBOTT, R.; ABBOTT, T.; ABRAHAM, S.; ACERNESE, F.; ACKLEY, K.; ADAMS, C.; ADYA, V.; AFFELDT, C.; AGATHOS, M.; AGATSUMA, K.; AGGARWAL, N.; AGUIAR, O.; AIELLO, L.; AIN, A.; AJITH, P.; ALFORD, T.; ALLEN, G.; ALLOCCA, A.; ZWEIZIG, J. A guide to ligo–virgo detector noise and extraction of transient gravitational-wave signals. **Classical and Quantum Gravity**, v. 37, p. 055002, 03 2020. 51

ABBOTT, B. P. et al. Observation of gravitational waves from a binary black hole merger. **Physical Review Letters**, v. 116, p. 061102, 2016. 1, 9, 31, 33

_____. A gravitational-wave standard siren measurement of the hubble constant. **Nature**, v. 551, n. 7678, p. 85–88, oct 2017. ISSN 1476-4687. Available from: <<http://dx.doi.org/10.1038/nature24471>>. 34

_____. Gw170817: observation of gravitational waves from a binary neutron star inspiral. **Physical Review Letters**, v. 119, p. 161101, Oct 2017. Available from: <<https://link.aps.org/doi/10.1103/PhysRevLett.119.161101>>. 1

_____. _____. **Physical Review Letters**, v. 119, p. 161101, 2017. 83

_____. Multi-messenger observations of a binary neutron star merger. **The Astrophysical Journal Letters**, v. 848, n. 2, p. L12, oct 2017. 1

_____. Properties of the binary neutron star merger gw170817. **Physical Review X**, v. 9, n. 1, p. 011001, 2019. 30, 32

AGAZIE, G. et al. The nanograv 15-year data set: evidence for a gravitational-wave background. **The Astrophysical Journal Letters**, v. 951, p. L8, 2023. 32

AGGARWAL, K. et al. Constraining stochastic gravitational-wave backgrounds with pulsar timing arrays. **Physical Review D**, v. 108, p. 042003, 2023. 32

AGHANIM, N. et al. Planck 2018 results - vi. cosmological parameters. , v. 641, p. A6, sep. 2020. 20, 74

ALFRADIQUE, V.; BOM, C.; PALMESE, A.; TEIXEIRA, G.; SANTANA-SILVA, L.; DRLICA-WAGNER, A.; RILEY, A.; MARTíNEZ-VáZQUEZ, C.; SAND, D.; STRINGFELLOW, G.; MEDINA, G.; CARBALLO-BELLO, J.; CHOI, Y.; ESTEVES, J.; LIMBERG, G.; MUTLU-PAKDIL, B.; NOEL, N.; PACE, A.; SAKOWSKA, J.; WU, J. A dark siren measurement of the hubble constant using gravitational wave events from the first three ligo/virgo observing runs and delve. **Monthly Notices of the Royal Astronomical Society**, v. 528, 01 2024. 35

ARUN, K. G. et al. Impact of higher-order post-newtonian effects on the gravitational-wave signals from coalescing binaries. **Physical Review D**, v. 79, n. 12, p. 124037, 2009. 65

ASHBY, N. Relativity in the global positioning system. **Living Reviews in Relativity**, v. 6, p. 1, 2003. 9

BARTELMANN, M.; SCHNEIDER, P. Weak gravitational lensing. **Physics Reports**, v. 340, p. 291–472, 2001. 19

BARTUSIAK, M. **Archives of the universe: the cosmic microwave background and the new cosmology**. [S.l.]: Pantheon Books, 2006. 10, 13

BELAHCENE, I. **Searching for gravitational waves produced by cosmic strings in LIGO-Virgo data**. PhD Thesis (PhD) — Université Paris Saclay (COmUE), Oct 2019. Available from: <<https://theses.hal.science/tel-02878783>>. 29

BELGACEM, E.; DIRIAN, Y.; FOFFA, S.; HOWELL, E. J.; MAGGIORE, M.; REGIMBAU, T. Cosmology and dark energy from joint gravitational wave-grb observations. **Journal of Cosmology and Astroparticle Physics**, v. 2019, n. 08, p. 015–015, aug. 2019. ISSN 1475-7516. Available from: <<http://dx.doi.org/10.1088/1475-7516/2019/08/015>>. 67

BERTONE, G.; HOOPER, D.; SILK, J. Particle dark matter: Evidence, candidates and constraints. **Physics Reports**, v. 405, p. 279–390, 2005. 19

BLANCHET, L. Gravitational radiation from post-newtonian sources and inspiralling compact binaries. **Living Reviews in Relativity**, v. 9, n. 4, 2006. 65

BRANDENBERGER, R. **Why the DESI Results Should Not Be A Surprise**. 2025. Available from: <<https://arxiv.org/abs/2503.17659>>. 17

CAMARENA, D.; MARRA, V. A new method to build the (inverse) distance ladder. **Monthly Notices of the Royal Astronomical Society**, Oxford University Press (OUP), v. 495, n. 3, p. 2630–2644, apr 2020. ISSN 1365-2966. Available from: <<http://dx.doi.org/10.1093/mnras/staa770>>. 16

CARROLL, S. **Spacetime and geometry: an introduction to General Relativity**. [S.l.]: Cambridge University Press, 2019. 7, 8

CHANDRASEKHAR, S. **The mathematical theory of black holes**. [S.l.]: Oxford University Press, 1983. 9

CHEN, H.-Y.; FISHBACH, M.; HOLZ, D. E. A two per cent hubble constant measurement from standard sirens within five years. **Nature**, v. 562, n. 7728, p. 545–547, oct 2018. ISSN 1476-4687. Available from: <<http://dx.doi.org/10.1038/s41586-018-0606-0>>. 35, 73

CHEVALLIER, M.; POLARSKI, D.; LINDER, E. V. Accelerating universes with scaling dark matter. **International Journal of Modern Physics D**, v. 10, n. 3, p. 213–222, 2001. 21

COE, D. Fisher matrices and confidence ellipses: a quick-start guide and software. **Instrumentation and Methods for Astrophysics**, 2009. Available from: <<https://api.semanticscholar.org/CorpusID:118040490>>. 57

COSMIC EXPLORER PROJECT. **Cosmic explorer**. 2024. Available from: <<https://cosmicexplorer.org>>. 39, 46

D'INVERNO, R. **Introducing Einstein's relativity**. Oxford: Oxford University Press, 1992. 7, 8, 9

EINSTEIN, A. Die feldgleichungen der gravitation. **Sitzungsberichte der Königlich Preußischen Akademie der Wissenschaften (Berlin), 1915, part 2**, p. 844–847, 1915. 7, 9

_____. Cosmological considerations in the general theory of relativity. **Sitzungsberichte der Königlich Preußischen Akademie der Wissenschaften**, 1917. 20

EINSTEIN Telescope Collaboration. 2024. Available from: <<https://www.et-gw.eu>>. 39, 40, 46

EUCLID CONSORTIUM. **Euclid mission: cosmology and physics from the Euclid Survey**. 2020. Available from: <https://www.euclid-ec.org/>. 21, 65

FARR, W. M.; FISHBACH, M.; YE, J.; HOLZ, D. E. Gravitational-wave astrophysics: the role of the ligo-virgo detector network. **Living Reviews in Relativity**, v. 13, n. 1, p. 1–48, 2010. 69, 70

FEENEY, S. M.; PEIRIS, H. V.; RIESS, A. G.; SCOLNIC, D. Prospects for resolving the hubble constant tension with standard sirens. **Physical Review Letters**, v. 122, n. 6, p. 061105, 2019. ISSN 1079-7114. Available from: <<http://dx.doi.org/>>. 2

FERRI, J. V.; TASHIRO, I. L.; ABRAMO, L. R.; MATOS, I.; QUARTIN, M.; STURANI, R. A robust cosmic standard ruler from the cross-correlations of galaxies and dark sirens. **arXiv preprint**, 2024. 64, 81, 91

FISHBACH, M. et al. A standard siren measurement of the hubble constant from gw170817 without the electromagnetic counterpart. **The Astrophysical Journal Letters**, v. 871, n. 1, p. L13, jan 2019. ISSN 2041-8213. Available from: <<http://dx.doi.org/10.3847/2041-8213/aaf96e>>. 2

FREEDMAN, W. L. Measurements of the hubble constant: tensions in perspective*. **The Astrophysical Journal**, v. 919, n. 1, p. 16, sep. 2021. ISSN 1538-4357. Available from: <<http://dx.doi.org/10.3847/1538-4357/ac0e95>>. 2

FREEDMAN, W. L.; MADORE, B. F. The Hubble constant. **Annual Review in Astronomy and Astrophysics.**, v. 48, p. 673–710, 2010. 2

GELMAN, A.; CARLIN, J. B.; STERN, H. S.; DUNSON, D. B.; VEHTARI, A.; RUBIN, D. B. **Bayesian data analysis**. 3. ed. [S.l.]: CRC Press, 2013. 55

GONG, Y.; GAO, Q. On the effect of the degeneracy among dark energy parameters. **The European Physical Journal C**, v. 74, n. 1, jan. 2014. ISSN 1434-6052. Available from: <<http://dx.doi.org/10.1140/epjc/s10052-014-2729-2>>. 74

HALL, E. D. et al. Gravitational-wave science with cosmic explorer: the role of early detector upgrades. **Physical Review D**, v. 106, p. 062003, 2022. 39

HILBORN, R. C. Gw170814: gravitational wave polarization analysis. **arXiv preprint**, 2018. Available from: <<https://arxiv.org/pdf/1802.01193>>. 41, 47, 48, 49

HLOZEK, R.; CORTêS, M.; CLARKSON, C.; BASSETT, B. Dark energy degeneracies in the background dynamics. **General Relativity and Gravitation**, v. 40, n. 2–3, p. 285–300, jan. 2008. ISSN 1572-9532. Available from: <<http://dx.doi.org/10.1007/s10714-007-0548-6>>. 74

HOGG, D. W. Distance measures in cosmology. **arXiv preprint astro-ph/9905116**, 2000. 17, 18, 71

HOLZ, D. E.; HUGHES, S. A. Using gravitational-wave standard sirens. **The Astrophysical Journal**, v. 629, p. 15–22, 2005. Available from: <<https://doi.org/10.1086/431341>>. 2, 69, 70

HU, J.-P.; WANG, F.-Y. Hubble tension: the evidence of new physics. **Universe**, v. 9, n. 2, 2023. ISSN 2218-1997. Available from: <<https://www.mdpi.com/2218-1997/9/2/94>>. 89

HUSA, S.; KHAN, S.; HANNAM, M.; PÜRRER, M.; OHME, F.; FORTEZA, X. J.; BOHÉ, A. Frequency-domain gravitational waves from nonprecessing black-hole binaries. i. new numerical waveforms and anatomy of the signal. **Physics Review**, v. 93, p. 044006, Feb 2016. Available from: <<https://link.aps.org/doi/10.1103/PhysRevD.93.044006>>. 91

HUTERER, D.; WU, H.-Y. Not empty enough: a local void cannot solve the hubble tension. In: _____. **The Hubble constant tension**. Singapore: Springer Nature Singapore, 2024. p. 391–401. ISBN 978-981-99-0177-7. Available from: <<https://doi.org/10.1007/978-981-99-0177-7_21>>. 17

JANQUART, J. **Gravitational waves signal analysis: matched filtering, typical analyses and beyond**. Master Thesis (Master's) — Université de Liège, 2019–2020. Available from: <<http://hdl.handle.net/2268.2/9211>>. 50, 51, 52

JOHNSON, D. H. Statistical inference for proportions. **American Journal of Roentgenology**, v. 184, n. 4, p. 1057–1064, 2005. 73

KHAN, S.; HUSA, S.; HANNAM, M.; OHME, F.; PÜRRER, M.; FORTEZA, X. J.; BOHÉ, A. Frequency-domain gravitational waves from nonprecessing black-hole binaries. ii. a phenomenological model for the advanced detector era. **Physics Review**, v. 93, p. 044007, Feb 2016. Available from: <<https://link.aps.org/doi/10.1103/PhysRevD.93.044007>>. 91

KOKE, D. **Setup and commissioning of a Michelson interferometer for the demonstration of gravitational wave detection principles in outreach activities**. Master Thesis (Mestrado) — University of Münster, 2022. Available from: <<https://www.uni-muenster.de/imperia/md/content/physik_kp/agkappes/abschlussarbeiten/masterarbeiten/koke_master_thesis.pdf>>. 38

LEGACY COLLABORATION. **LSST Science: Legacy Survey of Space and Time**. 2021. Available from: <https://www.lsst.org/>. 21, 65

LIGO/VIRGO/KAGRA COLLABORATION. **User guide for public alerts**. 2024. Available from: <<https://emfollow.docs.ligo.org/userguide/capabilities.html>>. 54

LINDER, E. V. Exploring the expansion history of the universe. **Physical Review Letters**, v. 90, n. 9, p. 091301, 2003. 21

LISA CONSORTIUM. **Laser Interferometer Space Antenna**. <https://lisa.nasa.gov/>. Acessed on: 12 fev. 2025. 3

LONDON, L.; KHAN, S.; FAUCHON-JONES, E.; GARCÍA, C.; HANNAM, M.; HUSA, S.; JIMÉNEZ-FORTEZA, X.; KALAGHATGI, C.; OHME, F.; PANNARALE, F. First higher-multipole model of gravitational waves from spinning and coalescing black-hole binaries. **Physics Review Letter**, v. 120, p. 161102, Apr 2018. Available from: <<https://link.aps.org/doi/10.1103/PhysRevLett.120.161102>>. 91

LÜCK, H.; SMITH, J.; PUNTURO, M. Third-generation gravitational-wave observatories. In: _____. **Handbook of Gravitational Wave Astronomy**. Singapore: Springer Singapore, 2020. p. 1–18. ISBN 978-981-15-4702-7. Available from: <<https://doi.org/10.1007/978-981-15-4702-7_7-1>>. 40

MA, C.; WANG, S.; WANG, W.; CAO, Z. Using deep learning to predict matched signal-to-noise ratio of gravitational waves. **Physics Review**, v. 109, p. 043009, Feb 2024. Available from: <<https://link.aps.org/doi/10.1103/PhysRevD.109.043009>>. 50, 51, 52

MAGGIORE, M. **Gravitational waves: volume 1: theory and experiments**. [S.l.: s.n.], 2008. ISBN 0198570740, 9780198570745. 1, 23, 26, 27, 30, 31, 52, 54, 55, 69

MAGGIORE, M. et al. Science case for the einstein telescope. **Journal of Cosmology and Astroparticle Physics**, v. 2020, n. 03, p. 050, 2020. 35

MARSH, D. J. E. Axion cosmology. **Physics Reports**, v. 643, p. 1–79, 2016. 19

MARTYNOV, D. et al. Characterization of seismic noise at ligo sites. **Classical and Quantum Gravity**, v. 33, n. 16, p. 165003, 2016. 53, 54

MILLER, M. C.; YUNES, N. **Gravitational waves in physics and astrophysics**. [S.l.]: IOP Publishing, 2021. ISBN 978-0-7503-3051-0. 23

MISNER K. S. THORNE, J. A. W. C. W. **Gravitation**. [S.l.]: W. H. Freeman, 1973. 8

NASA / LAMBDA ARCHIVE TEAM. **Hubble constant**. 2024. Available from: <<https://lambda.gsfc.nasa.gov/education/graphic_history/hubb_const.html>>. 5

NEW SCIENTIST. **First glimpse of big bang ripples from universe's birth**. 2014. Accessed on: 12 Feb. 2025. Available from: <<https://www.newscientist.com/article/dn25235-first-glimpse-of-big-bang-ripples-from-universes-birth/>>. 33

PALMESE, A. et al. A statistical standard siren measurement of the hubble constant from the ligo/virgo gravitational wave compact object merger gw190814 and dark energy survey galaxies. **The Astrophysical Journal Letters**, v. 900, n. 2, p. L33, sep 2020. ISSN 2041-8213. Available from: <<http://dx.doi.org/10.3847/2041-8213/abaeff>>. 34, 35, 89

PEEBLES, P. J. E. **Principles of physical cosmology**. [S.l.]: Princeton University Press, 1993. 9, 74

PENZIAS, A.; WILSON, R. A measurement of excess antenna temperature at 4080 mc/s. **Astrophysical Journal**, v. 142, p. 419, 1965. 20

PERLMUTTER, S. et al. Measurement of ω and λ from 42 high-redshift supernovae. **Astrophysical Journal**, v. 517, p. 565, 1999. 20

RIESS, A. et al. Observational evidence from supernovae for an accelerating universe and a cosmological constant. **Astronomical Journal**, v. 116, p. 1009, 1998. 16, 20

RIESS, A. G. et al. Large magellanic cloud cepheid standards provide a 1% foundation for the determination of h0 and its uncertainties. **The Astrophysical Journal**, v. 876, n. 1, p. 85, 2019. 21

RIESS, A. G.; YUAN, W.; MACRI, L. M.; SCOLNIC, D.; BROUT, D.; CASERTANO, S.; JONES, D. O.; MURAKAMI, Y.; ANAND, G. S.; BREUVAL, L.; BRINK, T. G.; FILIPPENKO, A. V.; HOFFMANN, S.; JHA, S. W.; KENWORTHY, W. D.; MACKENTY, J.; STAHL, B. E.; ZHENG, W. A comprehensive measurement of the local value of the hubble constant with 1 km s1 mpc1 uncertainty from the hubble space telescope and the sh0es team. **The Astrophysical Journal Letters**, v. 934, n. 1, p. L7, jul 2022. ISSN 2041-8213. Available from: <<http://dx.doi.org/10.3847/2041-8213/ac5c5b>>. 2, 16, 74

ROOS, M. **Introduction to cosmology**. [S.l.]: John Wiley & Sons, 2003. 9, 16

RUBIN, V. C.; FORD, W. K. J. Rotation of the andromeda nebula from a spectroscopic survey of emission regions. **The Astrophysical Journal**, v. 159, p. 379, 1970. 19

RYDEN, B. **Introduction to cosmology**. [S.l.]: Addison-Wesley, 2003. 1, 10, 11, 13, 14, 15, 17, 19, 65

SAULSON, P. R. Fundamentals of interferometric gravitational wave detectors. **Physics Reports**, v. 216, n. 5, p. 175–196, 1990. 53

Schutz, B. F. Determining the hubble constant from gravitational wave observations. **Nature**, v. 323, n. 6086, p. 310–311, sep 1986. 2

SELLENTIN, E.; QUARTIN, M.; AMENDOLA, L. Breaking the spell of gaussianity: forecasting with higher order fisher matrices. **Monthly Notices of the Royal Astronomical Society**, v. 441, n. 2, p. 1831–1840, may 2014. ISSN 0035-8711. Available from: <<http://dx.doi.org/10.1093/mnras/stu689>>. 57, 58, 59, 61, 85

SOUZA, J. M. S. D.; STURANI, R. Cosmological model selection from standard siren detections by third-generation gravitational wave observatories. **Physics of the Dark Universe**, v. 32, p. 100830, 2021. ISSN 2212-6864. Available from: <<https://www.sciencedirect.com/science/article/pii/S2212686421000613>>. 65, 67

_____. Gwdali: a fisher-matrix based software for gravitational wave parameter-estimation beyond gaussian approximation. **Astronomy and Computing**, v. 45, p. 100759, 2023. ISSN 2213-1337. Available from: <<https://www.sciencedirect.com/science/article/pii/S2213133723000744>>. 61, 62, 63, 78, 91

SOUZA, J. M. S. de. **Late-Time cosmology with third generation gravitational waves observatories**. PhD Thesis (PhD) — Universidade Federal do Rio Grande do Norte, 2023. Available from: <<https://repositorio.ufrn.br/handle/123456789/12345>>. 24, 50, 59, 61

STRATTA, G.; PANNARALE, F. Neutron star binary mergers: the legacy of gw170817 and future prospects. **Universe**, v. 8, n. 9, 2022. Available from: <<https://www.mdpi.com/2218-1997/8/9/459>>. 1, 4

SUZUKI, N.; RUBIN, D.; LIDMAN, C.; ALDERING, G.; AMANULLAH, R.; BARBARY, K.; BARRIENTOS, L. F.; BOTYANSZKI, J.; BRODWIN, M.; CONNOLLY, N.; AL. et. The hubble space telescope cluster supernova survey: V. improving the dark-energy constraints above $z > 1$ and building an early-type-hosted supernova sample. **The Astrophysical Journal**, v. 746, n. 1, p. 85, 2012. Available from: <<https://supernova.lbl.gov/union/>>. 15

TEGMARK, M. The fisher matrix: method of estimating the precision of model parameters. **Astrophysical Journal**, v. 474, p. 1–23, 1997. 56, 57

TEGMARK, M. et al. The 3d power spectrum of galaxies from the sdss. **Astrophysical Journal**, v. 606, p. 702–740, 2004. 20

THORNE, K. S. Gravitational waves. **Proceedings of the National Academy of Sciences**, v. 92, n. 11, p. 11415–11420, 1995. 38

UNNIKRISHNAN, C. S. Indigo and ligo-india: scope and plans for gravitational wave research and precision metrology in india. **International Journal of Modern Physics D**, v. 22, n. 1, p. 1341010, 2013. 39

VALENTINO, E. D.; MENA, O.; PAN, S.; VISINELLI, L.; YANG, W.; MELCHIORRI, A.; MOTA, D. F.; RIESS, A. G.; SILK, J. In the realm of the hubble tension—a review of solutions *. **Classical and Quantum Gravity**, v. 38, n. 15, p. 153001, jul. 2021. ISSN 1361-6382. Available from: <<http://dx.doi.org/10.1088/1361-6382/ac086d>>. 89

VEITCH, J. et al. Parameter estimation for compact binaries with ligo and virgo: I. the fisher matrix. **Physical Review D**, v. 91, n. 4, p. 042003, 2015. 65

VITALE, S.; EVANS, M. Parameter estimation for binary black holes with networks of third-generation gravitational-wave detectors. **Physical Review D**, v. 95, n. 6, p. 064052, 2017. 66, 73, 81

WALPOLE, R. E.; MYERS, R. H.; MYERS, S. L. **Introdução à estatística e à probabilidade**. São Paulo: Pearson Prentice Hall, 2007. 79, 80

WANG, D. **Primordial gravitational waves 2024**. 2024. Available from: <<https://arxiv.org/abs/2407.02714>>. 32

WANG, Z.; LIU, C.; ZHAO, J.; SHAO, L. Extending the fisher information matrix in gravitational-wave data analysis. **The Astrophysical Journal**, v. 932, n. 2, p. 102, jun. 2022. ISSN 1538-4357. Available from: <<http://dx.doi.org/10.3847/1538-4357/ac6b99>>. 62, 70, 78, 91

WEINBERG, S. **Gravitation and cosmology: principles and applications of the general theory of relativity**. [S.l.]: John Wiley & Sons, 1972. 12

_____. **Cosmology**. [S.l.]: Oxford University Press, 2008. 32

WHELAN, J. T. **The geometry of gravitational wave detection**. LIGO Document Control Center, 2013. Available from: <<https://dcc.ligo.org/public/0106/T1300666/003/Whelan_geometry.pdf>>. 41, 43, 49

WITTMAN, D. **Fisher matrix for beginners**. 2016. Available from: <<https://wittman.physics.ucdavis.edu/Fisher-matrix-guide.pdf>>. 56

WONG, K. C. et al. H0licow - xiii. a 2.4% measurement of h0 from lensed quasars: Systematics and verification. **Monthly Notices of the Royal Astronomical Society**, v. 498, n. 4, p. 5112–5130, 2020. 21

ZWICKY, F. Die rotverschiebung von extragalaktischen nebeln. **Helvetica Physica Acta**, v. 6, p. 110–127, 1933. 19

APÊNDICE A - CORRELATION MATRIX

The correlation matrix is a mathematical construct used to quantify the linear dependence between pairs of random variables. Each element of this matrix, denoted as Corr_{ij}, represents the Pearson correlation coefficient between variables i and j, and is defined by the expression

$$\mathrm{Corr}_{ij} = \frac{\mathrm{Cov}_{ij}}{\sqrt{\mathrm{Cov}_{ii} \cdot \mathrm{Cov}_{jj}}}, \tag{A.1}$$

where Cov_{ij} denotes the covariance between variables i and j, while Cov_{ii} and Cov_{jj} correspond to the variances of variables i and j, respectively. This normalization ensures that the correlation coefficients are dimensionless quantities constrained to the interval $[-1, 1]$, enabling a direct interpretation of the strength and direction of the linear relationship between variables.

Quantitatively, a correlation coefficient of $+1$ indicates a perfect positive linear relationship, while a coefficient of -1 signifies a perfect negative linear relationship. A value of zero implies the absence of a linear correlation. Intermediate values can be interpreted according to their magnitude, with values close to ± 1 representing strong correlations, and values near zero indicating weak or negligible correlations. The sign of the correlation coefficient reveals the direction of the relationship: positive values correspond to variables that tend to increase together, whereas negative values indicate that one variable tends to decrease when the other increases.

Qualitatively, the correlation matrix provides a compact representation of the mutual dependencies among a set of variables, facilitating the identification of redundancies or strong associations that may influence statistical inference or model fitting. The matrix is symmetric, as $\mathrm{Corr}_{ij} = \mathrm{Corr}_{ji}$, and its diagonal elements are always equal to unity, reflecting the fact that each variable is perfectly correlated with itself. This structure makes the correlation matrix a central tool in multivariate analysis, particularly in fields such as statistics, cosmology, and data science.

PUBLICAÇÕES TÉCNICO-CIENTÍFICAS EDITADAS PELO INPE

Teses e Dissertações (TDI)

Teses e Dissertações apresentadas nos Cursos de Pós-Graduação do INPE.

Notas Técnico-Científicas (NTC)

Incluem resultados preliminares de pesquisa, descrição de equipamentos, descrição e ou documentação de programas de computador, descrição de sistemas e experimentos, apresentação de testes, dados, atlas, e documentação de projetos de engenharia.

Propostas e Relatórios de Projetos (PRP)

São propostas de projetos técnico-científicos e relatórios de acompanhamento de projetos, atividades e convênios.

Publicações Seriadas

São os seriados técnico-científicos: boletins, periódicos, anuários e anais de eventos (simpósios e congressos). Constam destas publicações o Internacional Standard Serial Number (ISSN), que é um código único e definitivo para identificação de títulos de seriados.

Pré-publicações (PRE)

Todos os artigos publicados em periódicos, anais e como capítulos de livros.

Manuais Técnicos (MAN)

São publicações de caráter técnico que incluem normas, procedimentos, instruções e orientações.

Relatórios de Pesquisa (RPQ)

Reportam resultados ou progressos de pesquisas tanto de natureza técnica quanto científica, cujo nível seja compatível com o de uma publicação em periódico nacional ou internacional.

Publicações Didáticas (PUD)

Incluem apostilas, notas de aula e manuais didáticos.

Programas de Computador (PDC)

São a seqüência de instruções ou códigos, expressos em uma linguagem de programação compilada ou interpretada, a ser executada por um computador para alcançar um determinado objetivo. Aceitam-se tanto programas fonte quanto os executáveis.